Manipulation of Conducting Oxides and Their Rational Design for Use in Photonics

by

Khue Nguyen

A thesis

presented to the University of Waterloo

in fulfilment of the

thesis requirement for the degree of

Master of Science

in

Chemistry

Waterloo, Ontario, Canada, 2022

Author's Declaration

I hereby declare that I am the sole author of this thesis. This is a true copy of the thesis, including any required final revisions, as accepted by my examiners. I understand that my thesis may be made electronically available to the public.

Abstract

Transparent conducting oxides (TCOs) have been largely studied for their applications in light emitting diodes (LEDs), photodetectors, solar cells, and other photonic uses. TCOs are useful as they can be doped or alloyed to tune specific properties such as photoluminescence (PL), allowing them to emit light spanning the entire visible region or near UV. Considering literature and research from the Radovanovic group, the TCO gallium (III) oxide (Ga_2O_3) and cerium oxide (CeO_2) were selected to be modified via doping, alloying and surface treatments to design functional nanoparticles (NPs). Cerium oxide nanoparticles (CNPs) were synthesized with varying surface modifiers to enhance their UV emission. Low temperature PL data of tri-octylphosphine oxide (TOPO) surface treated CNPs reveal a novel UV emission theorized to originate from the charge transfer (CT) between Ce^{3+} and TOPO ligands, and Ce^{3+} intracentre transitions (5d-4f). Lanthanides were then introduced into the CNPs as dopants to further functionalize CNPs. Erbium cerium oxide NPs demonstrated a novel white light emission, that could be useful in future white LED applications. Functionalization of CNPs by lanthanide incorporation is also explored through sensitization of Tb^{3+} ions. The synthesis of γ-gallium oxide (γ-Ga_2O_3) is also studied herein, and several synthesis parameters were tuned. Aluminum will be used as an alloying species because aluminum oxide (Al_2O_3) can form a defective spinel lattice structure like γ-Ga_2O_3 allowing it to easily form an alloy structure. Al_2O_3's larger band gap energy allows band gap manipulation in alloyed aluminum gallium oxides (AGOs) NPs. The results indicate an increase in band gap energy and an emission shift to the UV region as aluminum concentration is increased. Overall, the results found herein the thesis demonstrate the use of rational design and nano-engineering to achieve novel and useful metal oxide NPs for potential applications in photonics and beyond.

Acknowledgements

I would like to acknowledge all the members including several past members of the Radovanovic group that have helped me and guided me through out my time here. I would like to acknowledge my supervisor Pavle Radovanovic and my committee members German Sciaini and Vivek Maheshwari. Lastly, I would like to thank my family and friends who were always there for me.

Table of Contents

List of Figures
Chapter 1

Chapter 2

Chapter 3

Chapter 4

List of Tables

List of Abbreviations

ACAC	Acetylacetonate
AGO	Aluminum-doped Gallium Oxide
AMMD	Acrylamide and methylene diacrylamide
CB	Conduction Band
CNP	Cerium Oxide Nanoparticle
CT	Charge transfer
DAP	Donor-Acceptor Pair
FCC	Face centred cubic
FWHM	Full width of half maximum
IR	Infrared
LEDs	Light emitting diodes
LMCT	Ligand Metal Charge Transfer
MLCT	Metal Ligand Charge Transfer
NPs	Nanoparticles
OAM	Oleylamine
OA	Oleic acid
PL	Photoluminescence
PLQY	Photoluminescence Quantum Yield
QBS	Quinine Bisulfate
QD	Quantum dots
RBF	Round Bottom Flask
TBP	Tri-butylphosphine
TCOs	Transparent conducting Oxides
TEM	Transmission Electron Microscopy
TOPO	Tri-n-octylphosphine Oxide
TOP	Tri-n-octylphosphine
UV-Vis-NIR	Ultraviolet-visible-Near Infrared
VB	Valence band
XRD	X-ray diffraction

Chapter 1.0 Introduction

1.1 Semiconductors and Transparent Conducting Oxides (TCO)

Conductors are materials capable of transmitting electrons through them, while insulators are materials that cannot transmit electrons.[1,2] Electrons can occupy energy levels or bands in materials. Outer shell electrons occupy the valence band (VB) while free electrons occupy the conduction band (CB), energy difference between these bands is called the band gap energy.[2,3] Electrons must pass the band gap energy to be transmitted through materials. Electrons can move freely through conducting materials due to the VB and CB overlapping, and giving zero band gap energy.[1,2] On the other hand, insulators have large band gaps where the VB and CB are far apart in energy usually > 5 eV.[1,2] Semiconductors are materials between a conductor and insulator which show partial conductive properties, with a band gap usually between 0 eV and 5 eV.[1,2]

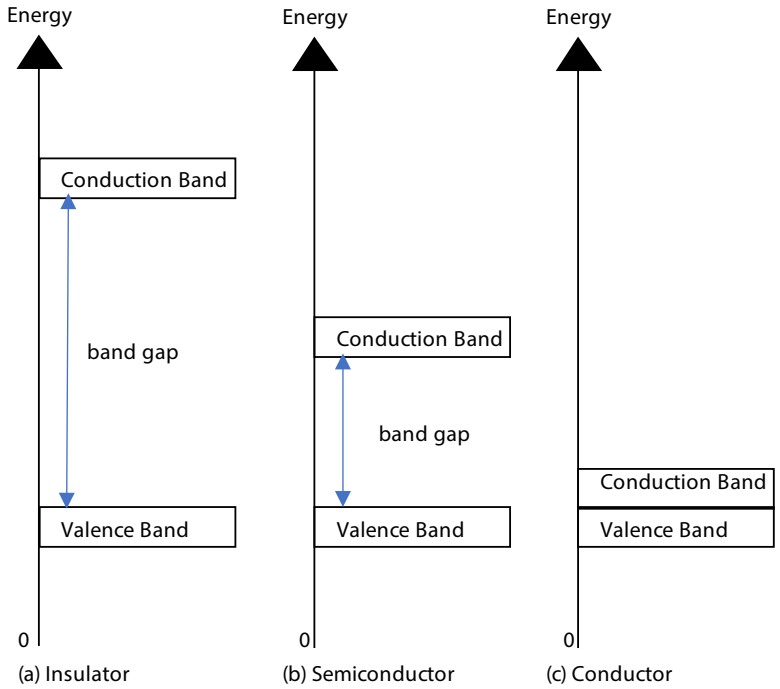

Figure 1. 1: Schematic diagram of energy levels and VB and CB for (a) insulators (b) semiconductors (c) conductors.

In the subcategories of semiconductors there are intrinsic and extrinsic semiconductors. Intrinsic semiconductors have a pure composition with no impurity, while extrinsic semiconductors are intentionally doped with impurities.[1,2,4] In intrinsic semiconductors the number of charge carriers is determined by the native material structure and native defects, while in extrinsic semiconductors the number of charge carriers depends on impurities.[3] This is due to the impurities supplying holes or electrons depending on the type of impurity, while an intrinsic semiconductor has holes and electrons supplied only by the pure structure.[5] Extrinsic semiconductors can exhibit p- or n-type characteristics (**Figure 1.2**).[6] A semiconductor doped with a cation with more valence electrons than the host will show n-type behaviour.[7] Electrons from the impurity will be close in energy to the CB, and so the CB would be partially filled by donated electrons.[6] However, a semiconductor with impurities with different number of valence electrons could not be n-type due to charge compensation.[7] A semiconductor doped with an element with fewer valence electrons then the host will show p-type behaviour.[6] The energy levels of the impurity's are close to the VB, and so the VB would be partially empty due to electron acceptors.[6] Charge carriers in n-type semiconductors are mostly electrons while majority of charge carriers in

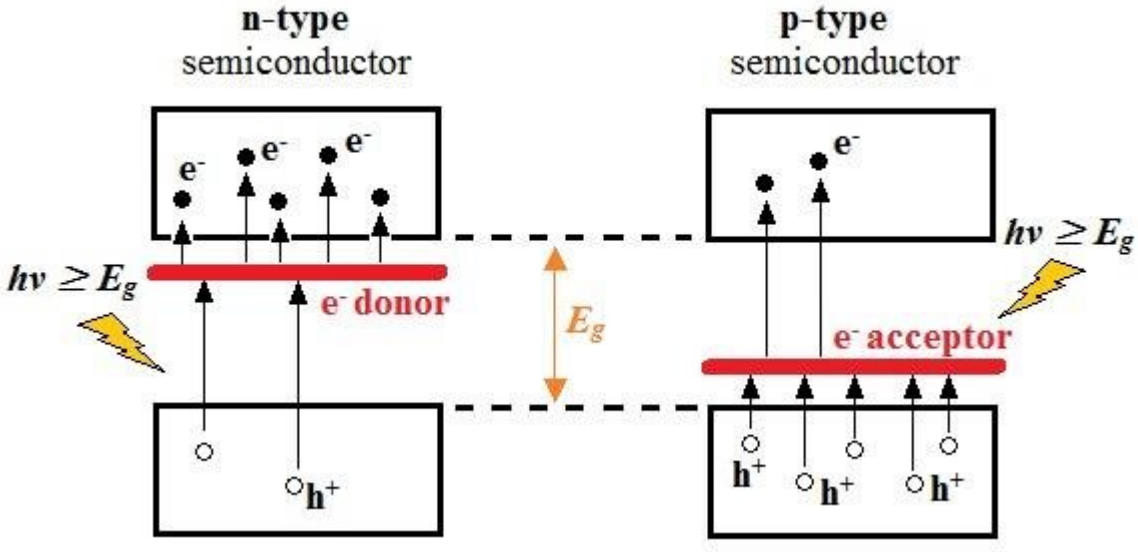

Figure 1. 2: Schematic energy diagram of n-type and p-type semiconductors, where E_g is the band gap energy. [23]

p-type semiconductors are electron holes or electron acceptors. In an intrinsic semiconductor the number of holes and electrons stays the same.[6,7]

Transparent conducting oxides (TCO) are another type of semiconductor with a wide band gap of > 3 eV which enables it to be transparent in the visible region.[8] Naturally occurring TCO's are usually n-type semiconductors, because of native defects acting as electron donor states.[6,9] By manipulating the dopants and dopant concentration in these materials, the conductivity and band gap can be tuned.[10,11]These materials also show high stability and absorption in the infrared and ultraviolet (UV) region, making them very valuable.[6] Today TCO's such as indium tin oxide are used in light emitting diodes (LEDs), solar cells, touch panels, among other applications.[6]

A high degree of control over the properties of nanomaterials is desired to enhance their functional properties. Native crystallographic defects have been investigated in TCOs, giving rise to modulation of electronic structure and enhancement of intrinsic properties.[9,12] Doped systems have also been investigated; they play a key role in exploring new avenues by extrinsically improving properties of nanostructures. Surface control of TCOs can also improve stability, efficiency and modulate properties of TCOs.[13] The effect of doping, defect control and surface control on optical, electronic, and magnetic properties is a potential motivation for expanding the application of the TCO nanoparticles.

Cerium oxide and gallium oxide are interesting TCO systems that have been specifically studied as part of this work. Their structural and optical properties are discussed herein.

1.2 Photoluminescence and Quantum Dots

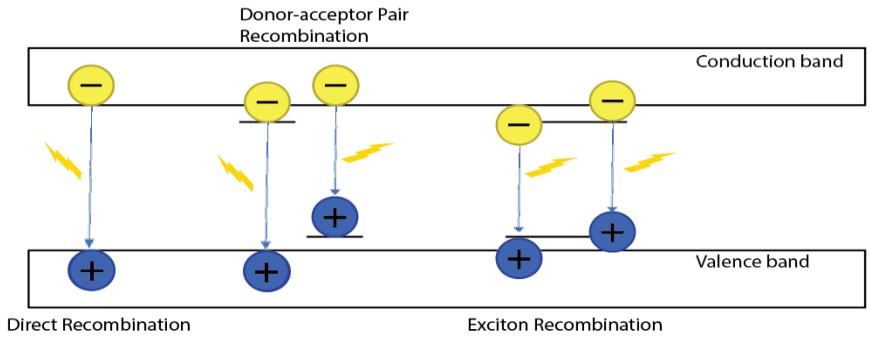

Figure 1. 3: Schematic diagram of recombination mechanism, electrons (yellow) and holes (blue).

Photoluminescence (PL) occurs when a material absorbs a light of certain wavelength (excitation) and then emits a light (emission) that has equal or less energy.[14,15] PL occurs in semiconductors when sufficient energy carried by a photon excites electrons from the VB into the CB, passing the band gap.[14,15] After excitation, electrons and holes form pairs called excitons.[16] These excitons then recombine during a relaxation period, where photons are emitted when electrons relax back into the VB.[14,15]

1.21 Donor Acceptor Pair Recombination

There is also donor-acceptor pair (DAP) recombination. In DAP recombination the semiconductor is doped so that it shows both n- and p-type properties.[9,18,19] The optical properties of oxides investigated in this thesis are explained by DAP mechanism, so it is worth discussing the underlying mechanism in terms of energy and its impact on the PL of TCOs. The PL properties arise from the electron-hole recombination upon transfer of the electron from the donor to the acceptor site named a tunnel transfer.[19,20] This DAP mechanism is a hallmark of Ga_2O_3, and the resulting PL can be manipulated by defect interactions induced by alloying or doping.[9,21,22] The ionized nature of donors and acceptors results in Coulomb interaction between them, which influence the energy of DAP emission, as illustrated by the following equation:

$$E_{em} = E_g - (E_D + E_A) + \frac{e^2}{4\pi\varepsilon r} \pm nE_{phonon} \quad \textbf{(Eq. 1)}$$

where E_g is band gap energy, E_D and E_A are donor and acceptor binding (ionization) energies, respectively, r is the average donor-acceptor separation, ε is the absolute permittivity of material (dielectric constant), E_{phonon} is the energy of phonons involved in the radiative transition and the third term on the right, $E_c = e^2 / 4\pi\varepsilon r$, is the Coulomb term.[23] Smaller distances between DAPs (smaller r) leads to an increase in Coulomb interaction between them and as a result, a blue shift in emission.[24] Defect density, as a result, is a parameter which can be utilized to tune the PL emission in the visible range to enhance the applicability of TCO nanomaterials.[25]

There are several methods to modulate the emission of nanoparticles (NPs) whose PL is governed by DAP mechanisms. The Radovanovic research group has recently demonstrated that γ-Ga_2O_3 can be stabilized in the nanocrystalline form through the colloidal synthesis, and its optical properties were controlled by tuning the size and composition.[10] The relationship between excited carrier lifetime and concentration of defects is another valuable conclusion drawn from the DAP model.[12] High energy emission is expected to decay faster, compared to the low energy side of the DAP emission.[12] The shorter separation between defects, causes the phosphor to emit at higher energy, which in turn leads to a higher probability of charge recombination.[24] Smaller donor-acceptor pair separation is achieved by synthesizing small NPs either at lower temperature or at shorter reaction times.[10] A reducing environment, intensifies the PL emission, while an oxidizing environment leads to a pronounced decrease in the PL intensity, both of which indicate the influence of the control over internal and surface structural defects to chemically tune the optical properties of NPs.[26] Subsequently, they illustrated that luminescent dopants or conjugated molecules adsorbed to the surface can interact with native defects via energy transfer and could be

utilized to exploit the PL properties of these NPs for applicative use in photonics.[13] Further literature review will be discussed later for more details.

1.22 Quantum Confinement

Quantum confinement is a phenomenon that changes the physical properties of a material that is at the nanoscale.[27] As the size of a semiconductor approaches the Bohr radius of the given semiconductor the bandgap increases relative to that of analogous bulk material, which causes the energy levels to become discrete.[15] Quantum dots (QDs) are nano sized semiconductors that exhibit quantum confinement.[15,28]

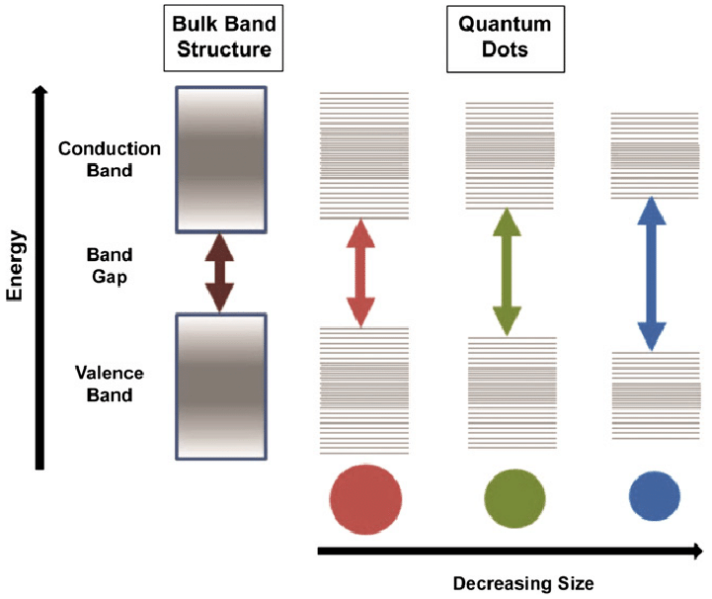

Figure 1. 4: Schematic diagram of quantum confinement on band gap.[15]

1.3 Gallium Oxide (Ga_2O_3) Structure and PL

The unique properties of Ga_2O_3 make it suitable for a variety of applications including, but not limited to, high powered microelectronics, phosphors, photodetectors and spintronics. Gallium Oxide (Ga_2O_3) forms defective lattice structures that displays TCO behaviour, particularly it is a natural n-type semiconductor.[29,30] These defect lattice structures are known as polymorphs and gallium oxide has 5 known polymorphs (α, β, γ, δ, and ε).[30] The material also has a wide bang gap of ~4.9eV. This means it can absorb UV light, which in turn allows Ga_2O_3 NPs to emit near UV rays, in some cases.[29,30] The β-phase was determined to be the most stable phase at room temperature.[20] All phases undergo phase transformation into the β-phase once annealed to 900^{o}C.[29,32] The main polymorph of interest in this thesis is the cubic γ-phase Ga_2O_3, due to its defect spinel structure and its near UV-emissions of ~410 nm.[31,32] The polymorph contains both oxygen and gallium vacancies, with gallium (III) occupying two tetrahedral and two octahedral sites, the structure can be described by **Figure 1.6**.[25] From previous studies in the Radovanovic group the PL mechanism in γ-Ga_2O_3 was determined to be DAP recombination, due to oxygen vacancies and gallium-oxygen vacancy pairs forming shallow donor and deep acceptor states.[33] The mechanism can be visualized in **Figure 1.5**.

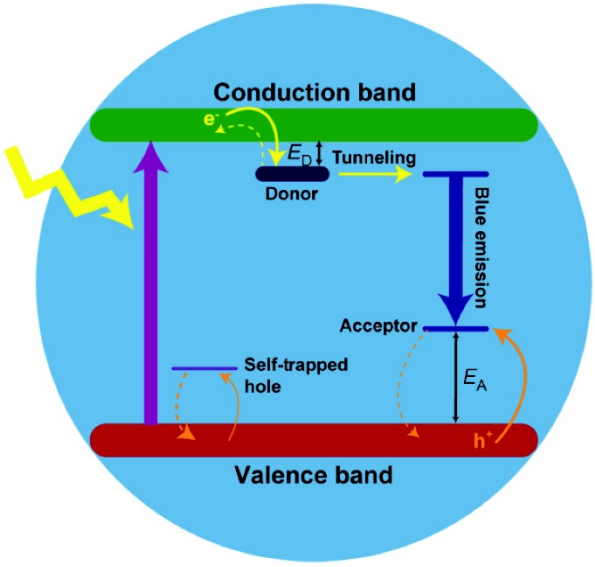

Figure 1. 5: Schematic illustration of the charge carrier pathways resulting in blue DAP emission of γ-Ga_2O_3 NPs. Thin solid arrows indicate carrier trapping and dashed arrows indicate carrier detrapping processes.

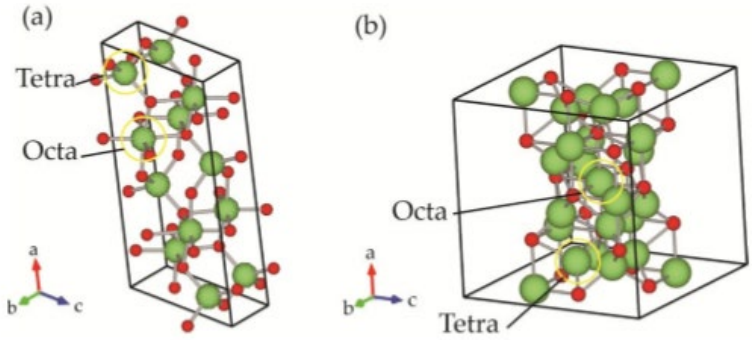

Figure 1. 6: Crystal lattice structure of Ga_2O_3 (a) β-phase (b) γ -phase. Green spheres are gallium ions and red spheres are oxygen ions, while the octahedral and tetrahedral sites are circled.[25]

1.4 Cerium Oxide (CeO_2) Structure and PL

Nanocrystalline cerium oxide (CeO_2) or commonly know as ceria has gained interest over the years for its unique optical, biological, and catalytic properties.[34] It also shows potential for multiple applications in spintronics, gas sensors, fuel cells, phosphors and photocatalyst.[34] Cerium oxide typically crystallizes in the fluorite crystal structure or face-centred cubic (FCC) and it consist of a cubic oxygen sub-lattice with cerium ions occupying alternate cube centres.[35] Each cerium cation is coordinated by eight oxygen anions (octahedral), and each oxygen anion is coordinated by the four nearest cerium cations (tetrahedral).[35] When cerium cations are replaced with lower valent elements or are vacant the lattice oxygens are removed to keep electrical neutrality, therefore introducing oxygen vacancies.[36,37]

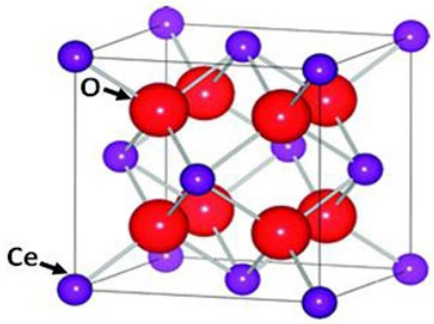

Figure 1. 7: Schematic diagram of CeO_2 crystal structure with oxygen as red orbs and cerium as purple.[34]

Cerium oxide contains mostly oxygen vacancies due to reversible transitions in the oxidation state of two cerium ions from Ce^{3+} to Ce^{4+}. The process can be shown in Kroger-Vink notation as:

$$O^{2-} + 2Ce^{4+} \rightarrow 2Ce^{3+} + \tfrac{1}{2}\, O_2(g) + V_o$$

Due to ease in redox-based reactions and to maintain electroneutrality, cerium oxide can easily occupy both Ce^{3+} and Ce^{4+} oxidation states..[38] Cerium oxide is well known to release significant levels of oxygen at low oxygen partial pressures.[39] For carrier and transport properties, the concentration of vacancies that are more mobile and can contribute to oxygen-ion transport in the solid solutions should be considered.[40] The formation energy of these oxygen vacancies is high at the (111) exposed facet and lower at the (110) and (100) facets, the stability of the planes follows the order (100) < (110) < (111).[40] Therefore, there are more oxygen vacancies at the (110) and (100) planes compared to the (111) facet. A diagram indicating cerium oxide facets (111,110,100) is demonstrated in **Figure 1.8**. The concentration of oxygen vacancies can be influenced by many internal and external factors such as temperature, synthesis method, and doping/alloying elements.[38]

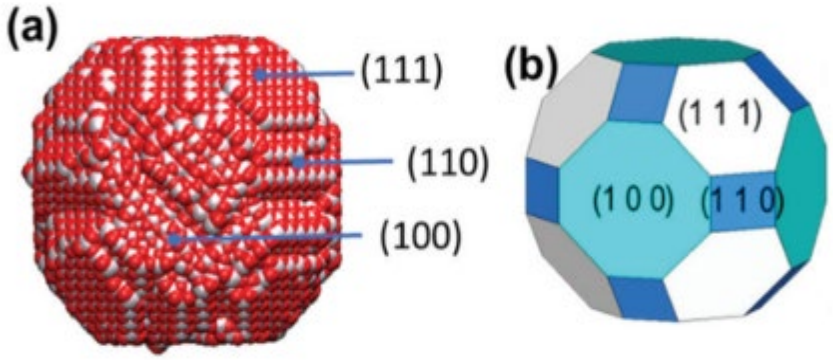

Figure 1. 8: (a) Full atomic level model f cerium oxide NPs. (b) showing more clearly the surfaces exposed by the NP.[38]

Studies on the photoluminescence mechanism of CeO_2 have been done and the consensus is that its emission is derived from several processes.[36,41] Low temperature PL measurements from a study done by Bazhukova et al. (2019) noticed several possible peaks in their PL spectra in **Figure 1.9**.[41] The peak at ~2.0 eV is attributed to a charge transfer (CT) between the 2p orbital of

oxygen and 4f orbital of Ce^{4+}.[41] The peak at ~3.0 eV is attributed to radiative intracentre transitions in the Ce^{3+} ion. The 5d-4f radiative transition which is known to appear usually as a doublet of broad, partial overlapping bands.[41] These bands are caused by radiative transition from relaxed lower 5d excited states to the ground 4f state split by spin-orbit interactions.[34,38] The weak band observed at ~2.5eV is associated with the emission of F_o centres related to the formation of oxygen vacancies.[38,41]

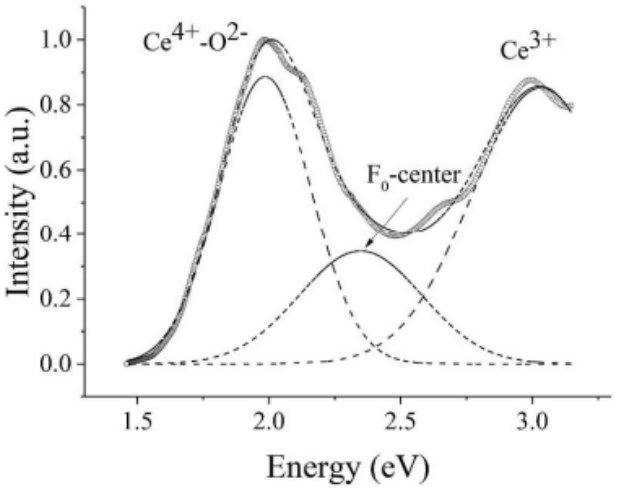

Figure 1. 9: Low temperature PL data of CeO_2 from literature.[41]

1.5 Doping Semiconductors

Dopants affect the optical, luminescent, physical, magnetic, and electronic properties of semiconductors.[3,7] By using various dopants, semiconductors can be tailored for specific applications such as electroluminescence devices, electronic displays (LEDs), solar cells, touch panels and bioimaging to name a few.[15] Dopants introduce new energy states in the band gap. Depending on if the dopant is electron donating or electron accepting the resulting semiconductor will be n- or p- type.[11]

There are several kinetic and thermodynamic factors that can effect the efficiency of dopant incorporation into a crystal structure.[42] One of these thermodynamic factors is the self-purification properties of NPs.[4] As a NP is annealed (heated) defects and dopants are removed from the lattice and onto the surface of the crystal as the Gibbs free energy is minimized.[42] This is due to the thermostability of the crystal at high temperatures favoring a structure with less defects or

dopants.[42] As stated earlier the γ-Ga_2O_3 defect lattice when heated to 900ºC will phase shift into the beta polymorph because it has the least defects in its structure.

1.6 Alloying and Mixed Semiconductors

The ability to mix semiconductors of different chemical compositions and stoichiometry can lead to changes in properties that are not seen in the single components that make up the mixed semiconductor.[43,44] An alloyed semiconductor is mixed structure semiconductor made by combining two or more metallic elements or anions.[27] The mixture of two metal elements would be heterogeneous with no defined structure.[43] Traditionally a semiconductor alloy is made of combining two or more elements or compounds which are in group 3 or 5 of the periodic table, examples being, GaAs and InP.[27,44] However, the alloying of TCO polymorphs as heterostructures of varying elements have been of interest. The idea behind alloys is to create semiconductors having intermediate properties with respect to already existing natural semiconductors. Properties such as the band gap of semiconductors can be controlled by alloying.[44]

One of the difficulties of getting a good alloy or heterostructure is matching of the phases and getting good combination of the two different phases. One way to remedy this is to alloy two TCOs with similar phases.[21] For example, gallium and aluminum oxide both have similar polymorphs and studies have shown that theoretically an aluminum gallium oxide alloy should be possible due to phase matching.[45] Other difficulties include energy favorability, dislocation defects affecting phase interfaces and appropriate substrate for growth.[44] The use of buffer layers to distribute lattice mismatch over a large thickness has been employed to mediate some of these challenges.[44] Different synthesis methods can also produce variable alloys, a method that nucleates and grows as an alloy is interesting as it requires no substrate.[44] Here, Al_2O_3 and Ga_2O_3 are

attempted to be alloyed together specifically in the γ-phase to control and tune the band gap to higher energy levels for UV applications.

1.7 Mechanisms of Chemical Doping in Semiconductors

Dopants can occupy vacancies, interstitial, and substitutional sites. In vacancy doping a vacancy forms a free positive hole or free electrons, as charge carriers.[3] Interstitial sites are sites

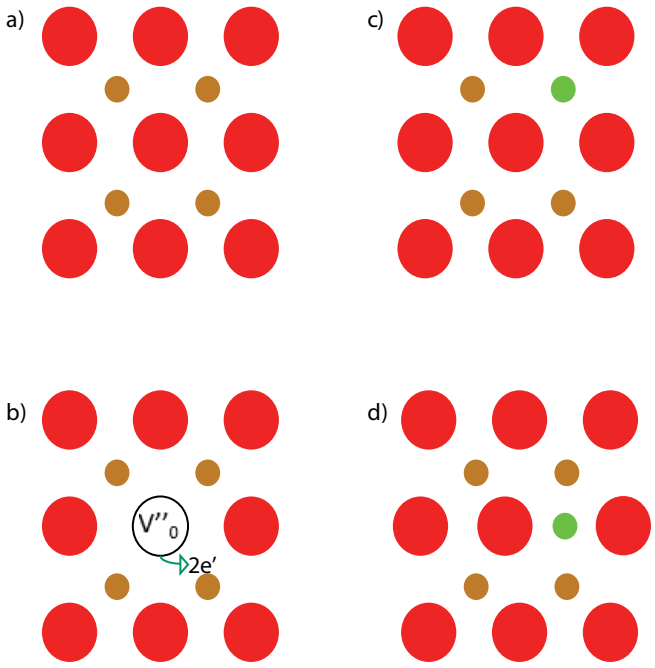

Figure 1. 10: Schematic diagram of different types of doping. (a) native lattice, (b) vacancy, (c) substitutional and (d) interstitial sites.

caused by incorporation of impurities in-between regular sites.[3] Substitutional sites are when an atom in the pure lattice is replaced with a dopant.[3] For both interstitial and substitutional doping the dopant can be aliovalent meaning the dopants have different valence than the atoms that make the host lattice.[46] The aliovalent dopants cause free electrons or holes, making n- and/or p-type semiconductors.[3]

1.8 Surfactants and Post Ligand Treatments in Semiconductor Synthesis

Surfactants are molecules that have a hydrophilic (polar) and lipophilic (non-polar) ends or amphiphilic properties.[47] Surfactants lower the surface tension between substances.[47] They are used in a wide range of applications such as in detergents, emulsifiers, and NP synthesis.[47]

Impurities require energy to deposit on a lattice's surface, this impurity formation energy can be changed due to the presence of surfactants on the surface.[48] This is due to the surfactants affecting the surface energy of the semiconductor allowing it to trap dopants in growing NPs.[49] The dopant is first incorporated to the surface of the crystal and as the crystal grows, bulk material will form on top of the impurity.[47] The method of synthesizing NPs by using surfactants is called the colloidal method, as a colloidal structure forms around the NP.[48]

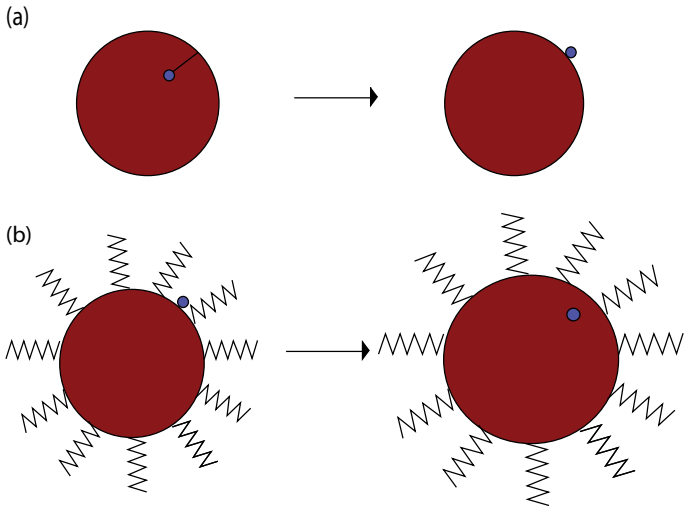

Figure 1. 11: Different mechanisms during doping (a) self-purification of dopant (blue sphere) from bulk (red sphere). (b) Colloidal structure with surfactant (black zigzags) trapping of dopant into the bulk.

Surfactants also play a key role in protecting the NP from degradation as well as control and modify properties of NPs. The study of surfactants as surface ligands and their effect on nanoparticle properties have been thoroughly investigated. Surfactant molecules such as tri-octylphosphine oxide (TOPO), Oleic acid (OA) and oleylamine (OAM) have proven in many

pieces of literature as an effective solvent and surface modifier in nanoparticle synthesis. OA, OAM, and TOPO have shown reducing power and can coordinate reactions.[50] TOPO is used widely as capping agents to control size and solubility.[50]

1.9 Metal Ligand/Ligand Metal Charge Transfer

Ligands also play an important role in energy transfer on the surface of NPs. A metal to ligand charge transfer (MLCT) may occur if the metal is in a low enough oxidation state and the ligand possess low-lying empty orbitals.[51] The process begins with the absorption of light onto a metal ligand complex, the valence electrons in the metal orbitals are excited to the ligand Π-orbitals, the electron can then recombine with the resulting holes to cause fluorescence.[52] **Figure 1.12** demonstrates an example of a MLCT between a d^5 uncoordinated metal and a ligand with low-lying empty Π-orbitals.[51] MLCT can occur on the surfaces of NPs and can act as sensitizers or as a method to tune photoelectric properties of NPs.[52]

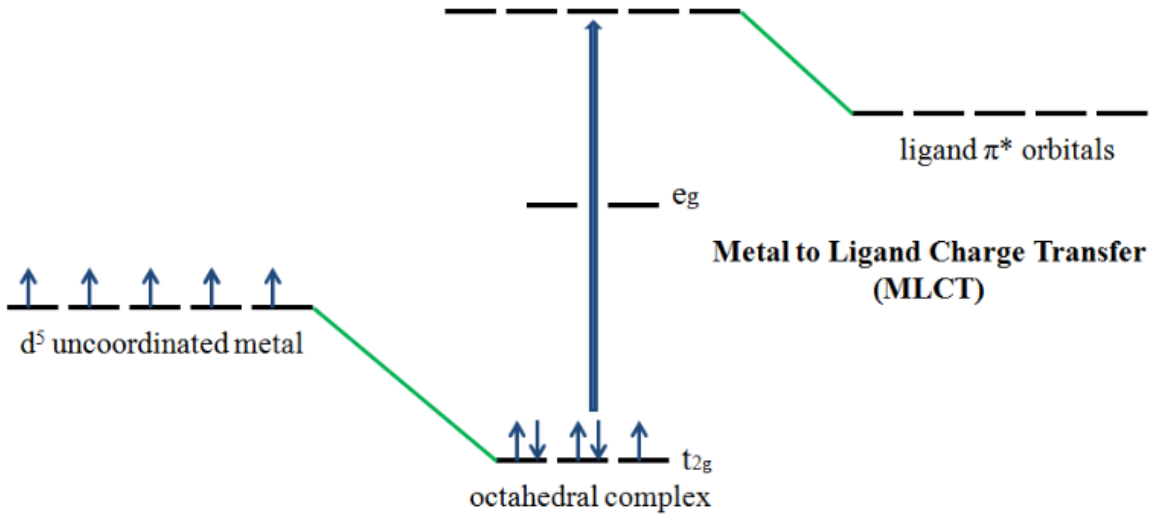

Figure 1. 12: Schematic diagram of an example of MLCT between an octahedral d^5 complex and ligand.[51]

It is also possible for a ligand to metal charge transfer (LMCT) to occur with a ligand bound to metal NP surfaces.[51] LMCT occurs between MOs of ligands that are full and empty or partially filled metal d-orbitals.[51] LMCT occurs similarly to MLCT where it starts with an absorption of light and an excitation of an electron, the resulting recombination can also cause fluorescence.[52] **Figure 1.13** depicts an example of LMCT between ligand sigma orbitals and partially filled metal d-orbitals.[51] MLCT or LMCT mechanism will be explored herein for the elucidation of novel properties found in the results.

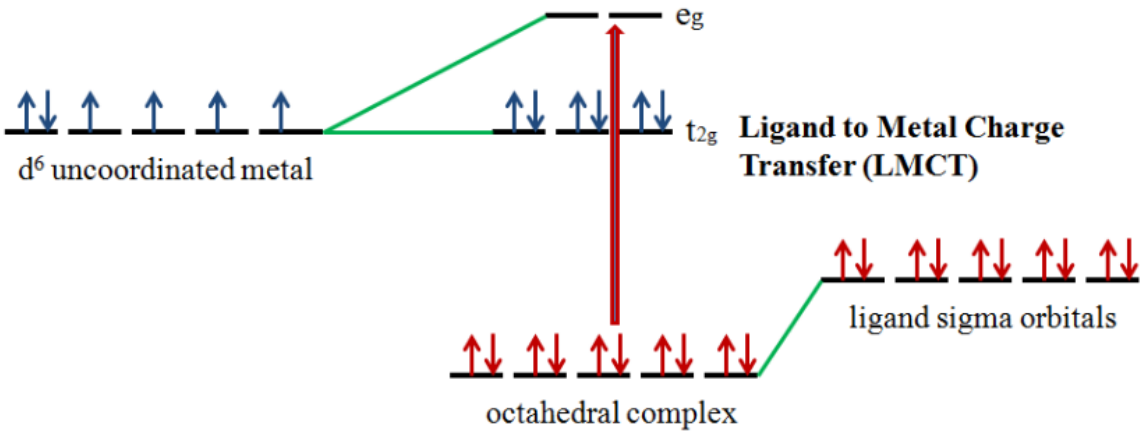

Figure 1. 13. Schematic diagram of an example of LMCT between ligand sigma orbitals and partially filled metal d-orbitals.[51]

1.10 Lanthanides

Research in lanthanides is pursued for their unique properties and for their use in bioimaging, telecommunications, lighting, and sensors.[53] The lanthanides comprise of 15 elements from atomic numbers 57-71 and are named lanthanides due to their similarity to the element lanthanum.[53,54] They are also commonly referred to as the rare-earth elements or metals. The Ln's are f-block elements and have continuously filled 4f orbitals which are shielded by the filled 5s and 5p outer shells.[54] Ln's also contain numerous energy states. 4f-4f transitions are expected in lanthanides however, the probability of such transitions is governed by selections rules. In particular, the 4f-4f transition in Ln's is forbidden due to the Laporte selection rule, which states that transitions between the states that are symmetric with respect to an inversion centre will not be observed.[9] Lanthanide's ground and excited state energy levels have the same symmetry with respect to an inversion center and therefore their 4f-4f transitions posses low absorption coefficients and the radiative decay of their excited states often last for milliseconds.[54]

Because of the symmetry forbidden character of lanthanides, they are challenging to incorporate into optoelectronic devices, however there are methods to still exploit the properties of lanthanides and considerable effort has been put into this. Lanthanides can be useful as they can resist photobleaching, cause upconversion in doped NPs and increase in PL band width to cover the entire visible and NIR region.[55] For lanthanides to be incorporated into nanomaterials the lanthanide dopants must be sensitized by the host materials. The right host lattice must be chosen carefully, it must be chemically and photophysically stable as well as have reduced nonradiative recombination processes.[9,53] In literature the most widely used host systems are alkaline earth fluorides and recently oxides have been investigated as an alternative.[54]

1.10.1 Lanthanide Sensitization

Sensitization or photosensitization is the process of initiating a luminescent process through one absorbing species that in turn transfers energy to a desired fluorophore, causing photoluminescence of the desired fluorophore.[56] Lanthanides are one such reactant that is commonly sensitized by energy-transfer from some other strongly absorbing chromophore or species.[56] This is done to overcome the main problem with direct excitation of lanthanides, which is that they are Laporte forbidden and have weak transitions. Sensitized lanthanide complexes are an attractive luminescent material due to their characteristic narrow bands and long emission lifetimes.[56] Usually, a ligand with a high absorption in the UV region will act as the light absorbing fragment to in turn sensitize the lanthanide luminescence.[56] However, in recent years the variety of different species and NPs used to sensitize lanthanide-based luminescence have increased. A study published by the Radovanvoic group have demonstrated the use of NPs as sensitizers for lanthanide-based emissions.[9] They demonstrated the use of γ-Ga_2O_3 DAP emission as an energy transfer source for lanthanide-based photoluminescence.[9] In more recent studies researchers such as Hasegawa et al. (2018) have been able to demonstrate effective photosensitized, electrosensitized and mechanosensitive luminescence of lanthanide complexes.[56] They were able to demonstrate lanthanide (III) complexes with photosensitized luminescence that was sensitized by LMCT bands.[56] A combination of new discoveries and a need for effective and efficient photonics has led to further study of lanthanide sensitization. Herein, UV emitting CeO_2 NPs are studied as potential sensitizers for lanthanide dopants. New methods of sensitizing lanthanides can lead to novel NPs and complexes for use in photonics, solar cells, and sensing devices.

1.11 Pertinent Literature Review

1.11.1 Surface Effects

The study of NP surface ligands and their effect on nanoparticle properties have been thoroughly investigated. Common studied surface ligands are based on organic thiols, amines, phosphines, carboxylic acids, and hydroxyl surfactants.[49,57] Molecules such as tri-octylphosphine (TOP), TOPO, OA and OAM are common surface ligands that have proven in literature to be effective coordinating solvents and/or surface modifiers in NP synthesis.[58] OA and OAM have shown reducing power and can coordinate reactions.[48] TOP and TOPO are used widely as capping agents to control size, solubility and to act as a protective layer against oxidation.[58] In a study by Abel et al. (2008), TOP was used as a capping agent for PbS nanoparticles, and it has also been demonstrated that the TOP-treated samples when compared to non-treated ones had a photoluminescence quantum yield (PLQY) increase and size tunability.[58]

Surface modifiers are also capable of impacting the optical properties of NPs. Giri et al. studied the rational surface modification of Mn_3O_4 nanoparticles to induce change in their optical properties.[52] In one study Mn_3O_4 was functionalized with –OH (hydroxyl group of glycerol), –OH and $–NH_2$ (hydroxyl and amine groups of ethanol amine), $–NH_2$ (amine group of guanidine), $–COO^-$ (carboxylate group of succinate), $–COO^-$ and $–NH_2$ (carboxylate and amine groups of glycine), and $–COO^-$ and –SH (carboxylate and thiol groups of thioglycolate) functional groups of the ligands.[52] In **Figure 1.14** the absorption of as-synthesized Mn_3O_4 and surface modified Mn_3O_4 is shown. In all cases except for as-synthesized sample, a characteristic absorption band (marked by arrows in **Figure 1.14**) between 300 and 360 nm is observed. This high energy absorption band

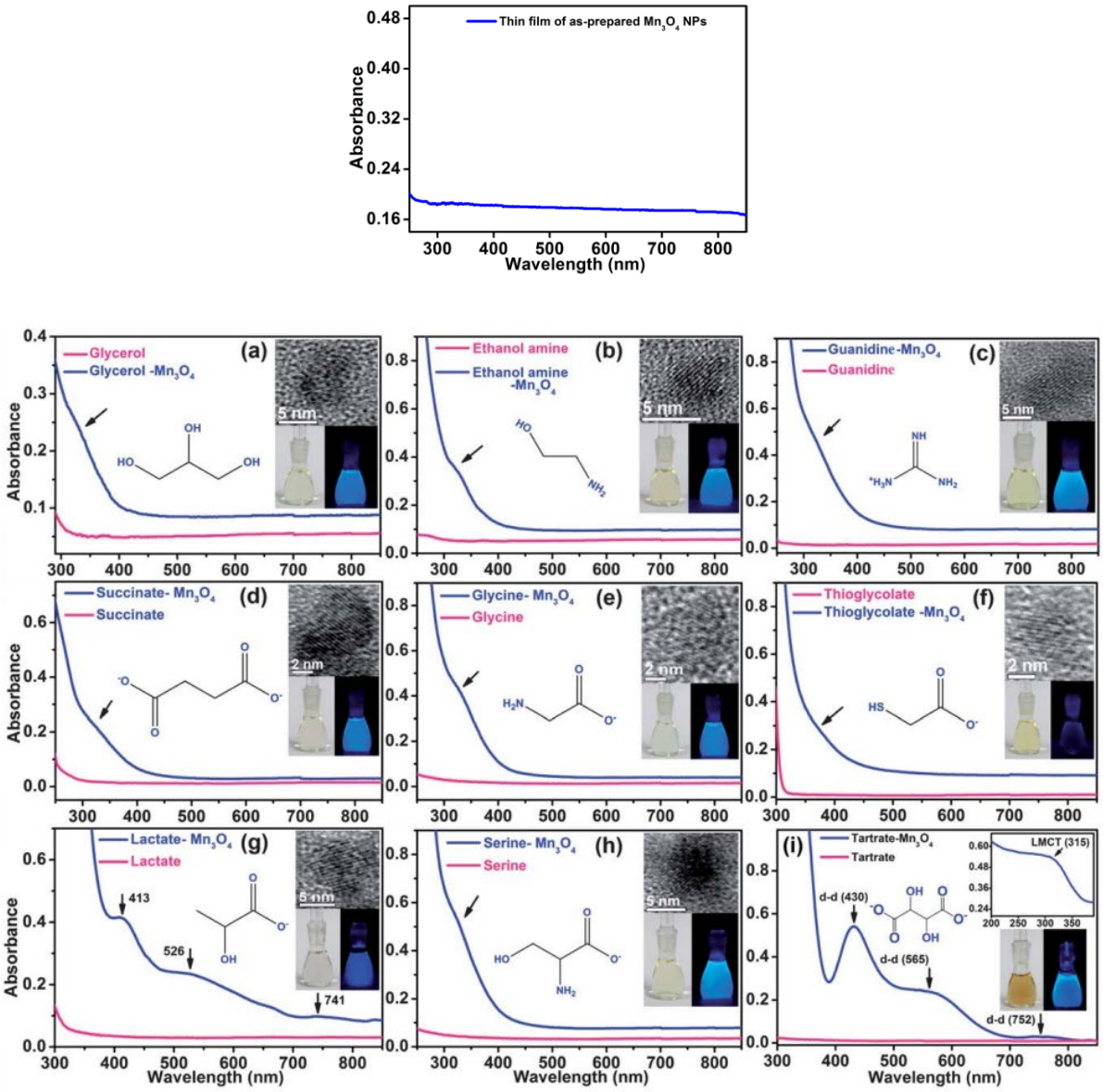

Figure 1. 14: Absorption spectra of Mn_3O_4 (top) and absorption spectra of surface functionalized Mn_3O_4 based on varying surface modifiers (bottom).[52]

is the result of the interaction between the ligand functional groups and the Mn^{2+}/Mn^{3+} on the NPs surface, therefore assigned as a LMCT band.[52] From the study they determined that a-hydroxy carboxylate moiety on the surface coordinating ligand is necessary to activate the observed distinct absorption features, where they see that the tartrate ligand has two a-hydroxyl groups which shows the best results in terms of most pronounced features in **Figure 1.14.** To further study the ligand-metal charge transfer band they studied the PL of tartrate-Mn_3O_4.[52]

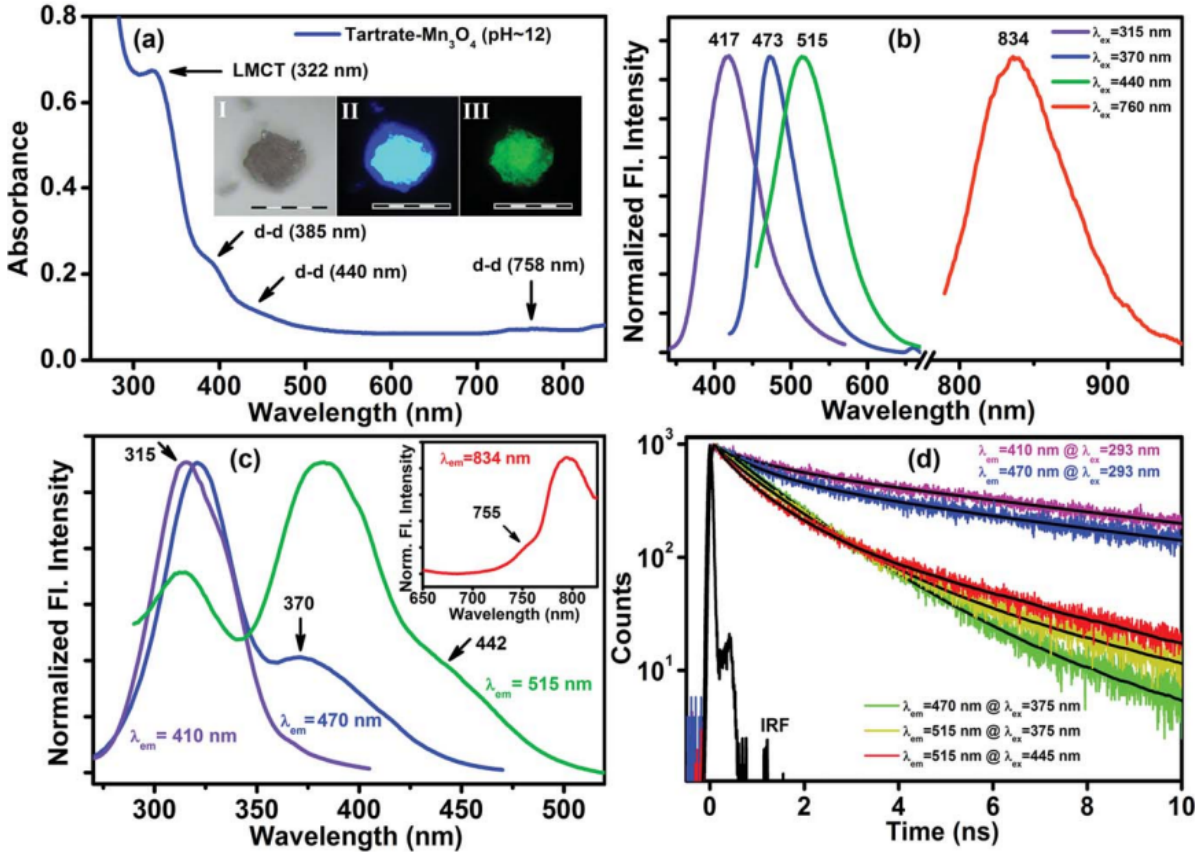

Figure 1. 15: (a) UV-V absorption spectrum of T-Mn_3O_4 NPs after treatment (at pH 12 and 70 C for 12 h). The inset shows the fluorescence microscopic images of the same NPs under irradiation with white light (bright field, I) and light of two different wavelengths: 365 (II) and 436 (III) nm. The scale bars in the images are 500 mm. (b) Normalized steady-state PL spectra collected from T-Mn_3O_4 NPs at four different excitation wavelengths of 315, 370, 440 and 760 nm at pH 12. (c) Excitation spectra of T-Mn_3O_4 NPs at different PL maxima of 410, 470, 515 and 834 nm. (d) Picosecond-resolved PL transients of T-Mn_3O_4 NPs in water measured at emission wavelengths of 410, 470 and 515 nm upon excitation with excitation sources of 293, 375 and 445 nm wavelengths.[52]

Figure 1.15 shows the absorption, PL excitation and emission spectra and the picosecond time resolved PL transients of tartrate-Mn_3O_4. In the excitation spectra (**Figure 1.15 (c)**) of tartrate-Mn_3O_4 at their respective PL maxima, the observed peaks directly correlate with the absorption peaks involving LMCT and d–d transitions (**Figure 1.15 (a)**). Therefore, the PL as shown in **Figure 1.15 (b)** may originate predominantly from the LMCT between tartrate excited states and Mn^{3+} d orbitals.[52] **Figure 1.15 (d)** represents the PL decay transients of tratrate-Mn_3O_4 NPs at three different PL maxima of 410, 470 and 515 nm using three different excitation wavelengths of 293,

375 and 445 nm, respectively. The observed differences in the lifetime of tratrate-Mn_3O_4 NPs at 410 nm PL compared to the lifetimes at 470 and 515 nm PL, suggest a difference in their origin of PL. Furthermore, distinctly different lifetime values of 470 nm PL upon excitation using 293 (4.04 ns) and 375 (1.13 ns) nm sources differentiate the origin of the two excitations. Thus, the study concluded that the lifetime data and steady-state measurements suggest that the LMCT excited states are responsible for the PL at 417 nm.[52] Overall, the study represents the rational surface modifications of NPs with organic ligands to introduce changes in optical properties, specifically the introduction of a PL emission based on LMCT excited states. Here, in this thesis similar rational nano-engineering methods will be employed to further explore the effect of surface modifiers on NP optical properties and provide a good platform for manipulating optical properties using surface chemistry on NPs.

1.11.2 Cerium Oxide Pertinent Literature

CNPs have been mostly studied for their biomedical application. However, a small segment of literature has investigated it's use in photonic applications. Pertinent research on CNPs is reviewed here. In their study, Kumar et al. (2009) doped cerium oxide with europium and showed tunability into the visible region.[38] However, only a few studies have explored cerium oxides use for UV applications. Cerium oxides has potential in this area due to its blue and near UV emission in the range of ~400-500 nm.[35]

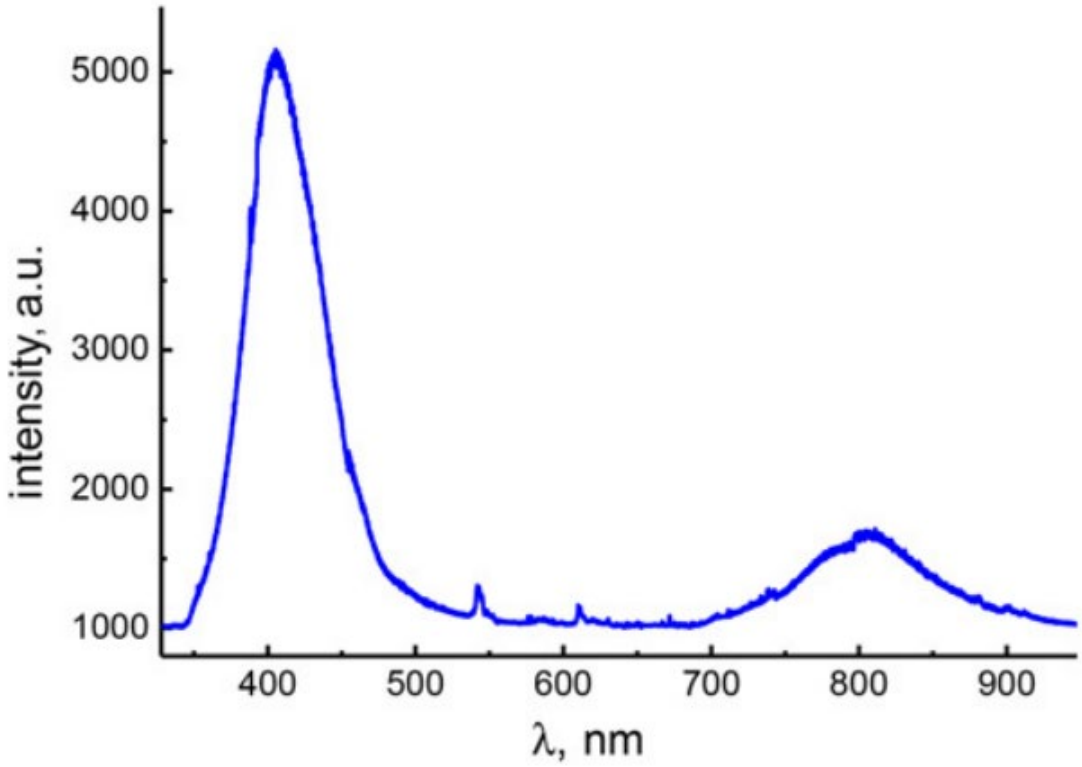

Figure 1. 16: Room-temperature PL spectrum of CeO2 nanoparticles.[40]

In their study, Meng et al. (2016) researched cerium oxide and cerium hydroxide particles that fluoresce in the blue/near UV region, the PL spectrum of such particles are shown in **Figure 1.16**.[40] There is a strong emission peak around 405 nm, which has been assigned to the near UV to blue excitonic emission.[59] Another study by Aslam et al. (2016) reported that the major peaks

in the PL spectra of CeO_2 appeared at 470 and 520 nm.[60] Therefore, the study by Meng et al. (2016) demonstrated the possibility of deeper UV emitting CNPs.[59]

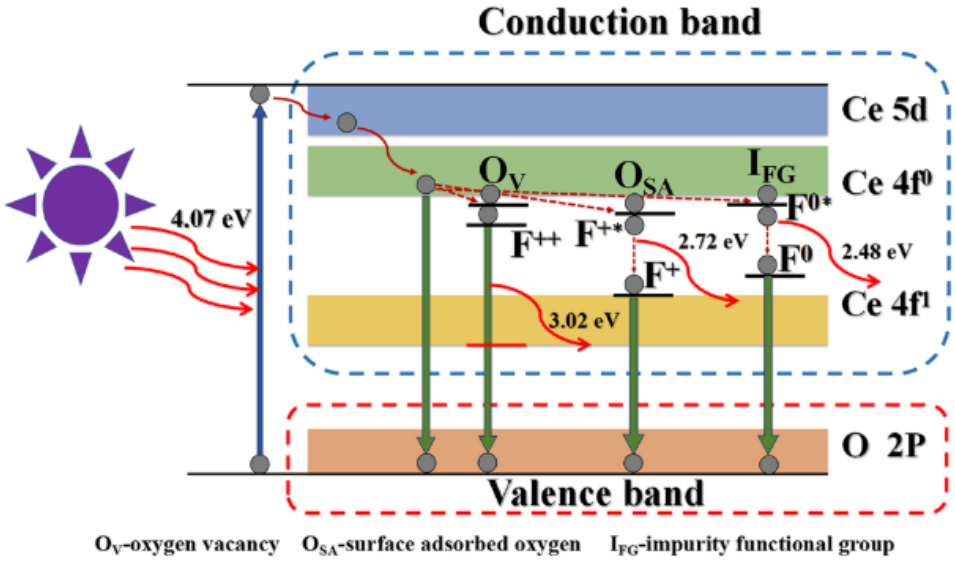

Figure 1. 17: Photoluminescence mechanism of CeO_2 nanoparticles modified by functional groups. The different charge states include neutral (F^0), singly charged (F^+), and doubly charged (F^{++}). The Oxygen vacancy (O_v), surface adsorbed oxygen (O_{SA}), and impurity functional group (I_{FG}) act as defect energy levels in the band gap.[61]

A few studies have explored surface modifications to CNPs, for example in a recent study by Wang et al. (2021) they were able to synthesize CNPs via a novel polyacrylamide gel method using cerium sulfate as a precursor.[61] They polymerized acrylamide and methylene diacrylamide (AMMD) with cerium sulfate to obtain a gel, which was then dried to obtain CNP powder. The resulting CNPs had their surface modified by the AMMD where the study determined about 0.3 AMMD content.[61] The resulting modifications affected the electronic structure of the particles by introducing oxygen vacancies, surface adsorbed oxygens and surface functional groups with different charge states. The different charge states include neutral (F^0), singly charged (F^+), and doubly charged (F^{++}).[61] The oxygen vacancy (O_v), surface adsorbed oxygen (O_{SA}), and impurity functional group (I_{FG}) act as defect levels in the system as shown in **Figure 1.17**. They reported a PL emission peak at 456 nm while other similar methods resulted in an emission peak at 470 nm, demonstrating that their CNPs were blue shifted.[61] Wang et al. (2021) concluded that the

synergistic effects of oxygen vacancy, surface adsorption oxygen concentration, and impurity functional groups resulted in high tunable photoluminescence properties of CeO_2 nanoparticles.[61] The thesis hopes to expand on the literature and determine the effect of several surface modifications on the electronic structure of CNPs and how it can be exploited to further develop PL applications of near UV emitting cerium oxides.

The colloidal synthesis of cerium oxide is still being tested and surface treatment of CNPs is currently being investigated. Surface modification has been shown to reduce surface ions, control size, and affect PL.[48,49,62] Due to the abundance of cerium and the increasing interest of UV technology, the literature has led to a need for the investigation of colloidally synthesized surface treated CNPs for photonic application.

1.11.3 Gallium Oxide Pertinent Literature

Much research has been done on TCO's and QD's with respect to PL. In a previous study by Farvid et al. (2011) colloidal γ-gallium indium (In) oxide NPs were formed for tunability throughout the visible region, **Figure 1.18** demonstrates this tunability.[21] It has also been shown that γ-Ga_2O_3's blue spectrum can be tuned by controlling their size via synthesis temperature.[10,31] As more indium was added the PL emission shifted towards the IR region. Indium was chosen as a dopant in this study due to In_2O_3 (E_g = 3.7 eV) similarities to Ga_2O_3. Both Ga and indium both belong to the same group in the periodic table and have the same oxidation states of +3.[21,63] From this literature, similar methods will be employed here to instead push the PL of γ-Ga_2O_3 to the UV-region.

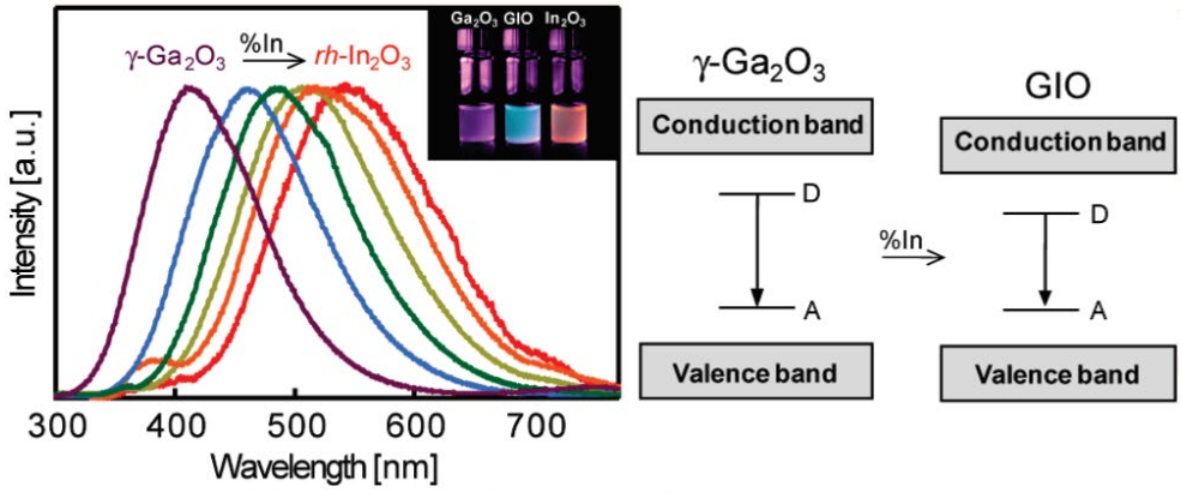

Figure 1. 18: Photoluminescence spectra of GIO NPs with 0 (purple), 13% (blue), 24% (green), 47% (olive), 84% (orange), and 100% (red) In content synthesized at 200°C (left) and Schematic representation of the possible origin of photoluminescence in undoped and doped NPs.[21]

In literature the common methods used to form NPs were the colloidal and solvothermal method.[64] In both methods surfactants such as OAM and TOPO were used to control NP size.[63] Precursors for NP synthesis can be metal salts such as gallium (III) nitrate and tin (IV) chloride.[65] Another common precursor used are coordination complexes such as metal acetylacetonates (acac), for example $Ga(acac)_3$, $Al(acac)_3$, $In(acac)_3$ among others.[64] From literature similar methodology and chemicals are used to form doped or alloyed gallium oxide NPs.

1.12 Motivation

Here cerium oxide was examined. Currently cerium is being mined and wasted as it is considered a "side product" of mining and so most of it is thrown away or unused.[66] Recent studies have shown that 89.02% of cerium can be recovered from rare earth polishing waste.[65] To investigate the uses of cerium oxide, synthesis and engineering methods were tested and a novel UV emitting CNPs was achieved by a TOPO surface treated colloidal synthesis method. The mechanism of the emission is examined and exploited for applicative use in photonics. In this work lanthanides are also used as dopants to be incorporated into CNPs to induce unique effects such as generating white light and lanthanide sensitization for photonic applications. Overall, this thesis demonstrates the use of surface modification and doping in nanomaterial engineering, particularly in cerium oxide systems and how it can improve NP functionality for photonic applications.

Aluminum gallium oxide (AGO) NPs were also examined. AGO NPs were synthesized via the colloidal and solvothermal method, with PL tunability in the near-UV region (300-400nm) controlled by concentration of aluminum (Al), temperature, reaction solvent and reaction duration. TCO NPs have been tuned to near-IR and near-UV however PL emission tunability into the near UV is much more difficult.[9] Determining the mechanism of PL in near UV emitting TCOs can help contribute to the understanding of band gap control, exciton recombination, donor acceptor pair recombination, and the effect of defects, dopants, and vacancies on PL emission.

The defective polymorph γ-Ga_2O_3 emits at ~410 nm which is near the UV-region making it a promising material for tunability into the deep UV region.[26] By incorporating with aluminum, the PL emission shifts to UV due to the large band gap of Al_2O_3 (~6.4 eV for nanostructured film and 8.8 eV for bulk).[67] Aluminum (Al) and gallium (Ga) are in the same group in the periodic table so they share similar electron configuration and have high stability and wide optical-bandgaps.[15]

Gallium oxide and cerium oxide is studied for applications in display/lighting devices, solar cells, as well as in deep UV photodetectors. The UV-emitting TCOs can also be used in plant growing lighting sources which emit UV light for growing specific plants/crops. The results of this work provide deeper understanding of the role of nano engineering in tailoring the optoelectrical properties of TCOs which is pivotal for the design of new functional materials. Developing the concept of rational doping, alloying and surface chemistry to alter the electronic structure of nanoscale materials is a promising and important area of research, serving as a prerequisite for the architecture of novel multifunctional systems. The motivation for the development of novel functional nanomaterials comes from the pressing need for sustainable energy, achieved in an efficient scalable fashion and environmentally friendly techniques.

2.0 Experimental

2.1 Chemicals

All chemicals used were purchased from Sigma-Aldrich and were used without any further purification. Gallium acetylacetonate (99.99%, $Al(acac)_3$), aluminum acetylacetonate (99.99%, $Ga(acac)_3$), cerium acetylacetonate (99.99%, $Ce(acac)_3$), erbium acetylacetonate ($Er(acac)_3$) and terbium chloride ($TbCl_3$) were purchased from Sigma-Aldrich and were used as precursors for the AGO NPs. Tri-n-octylphosphine oxide (90%, TOPO), Tri-n-octylphosphine (97%, TOP), Oleylamine (70%, OAM), Oleic acid (80%, OA), acetone (HPLC grade), Ethanol (EtOH, HPLC grade), and Hexane (HPLC grade) were used during synthesis and were purchased from Sigma-Aldrich.

2.2 Solvothermal Synthesis of AGO NPs

The solvothermal (ST) synthesis used was modified from work developed by previous group members.[33,64] The solvothermal method involves the use of a Teflon autoclave which is shown in **Figure 2.1**. For pure Ga_2O_3 samples approximately 0.5000 g of $Ga(acac)_3$ was weighed

Figure 2. 1: Teflon container (right), steel autoclave (middle) and fully setup reaction vessel (left).

on the analytical balance. For aluminum doped samples the amount of $Ga(acac)_3$ would be decreased, and $Al(acac)_3$ was added to eventually achieve % molar ratios of Ga%:Al% of 75%:25%, 50%:50% and 25%:75% and 100% aluminum.

The weighed-out precursors were added to labeled 10 mL beakers, then 10 mL of ethanol and 4 mL of OAM were added to each beaker and the solutions were then mixed using a magnetic stir bar and stirrer. The contents were then put into labeled 45 mL Teflon-lined stainless-steel autoclaves, and the autoclaves were placed into a preheated oven at 200°C. The synthesis temperature was varied to determine the effect of temperature on synthesis. The autoclaves were left in the oven for 24 hours, after which the oven was turned off and the autoclaves were left to cool naturally in the oven. The brownish gel-like substance obtained from the autoclaves were transferred to labeled test tubes and washed with a mixture of acetone and ethanol via 4-5 centrifugation, or until no more brownish color remains. Approximately 2 g of TOPO was added to each test tube and was TOPO treated at 90°C for 1 hour. The resulting samples were then washed via centrifugation, a small amount of the sample was dried onto a watch glass for structural analysis while the rest were dispersed in hexane for optical measurements.

2.3 Colloidal Synthesis of γ-Ga_2O_3, AGO, CeO_2 and Lanthanide-CeO_2 NPs

The colloidal method used in this project was modified from previous work developed by our group.[68] Amount of precursor for pure Ga_2O_3 and AGO is the same as described above for the solvothermal synthesis. A 3-necked round bottom flask (RBF) is placed onto an analytical balance where $Ga(acac)_3$ and/or $Al(acac)_3$ precursor was weighed out into the flask. 7g of OAM was then added, the mixture was stirred using a magnetic stirrer at room temperature till fully dissolved and stirred during the reaction. The RBF is then placed onto a heating mantle situated on top the magnetic stirrer. A reflux apparatus is then setup by placing a condenser in the middle neck, a thermometer in the right neck and a N_2 gas flow tube on the left neck and a gas out flow tube on top of the condenser. Steal wool was wrapped around the RBF to keep a constant temperature thought-out the flask, the reflux setup can be seen in **Figure 2.2**.

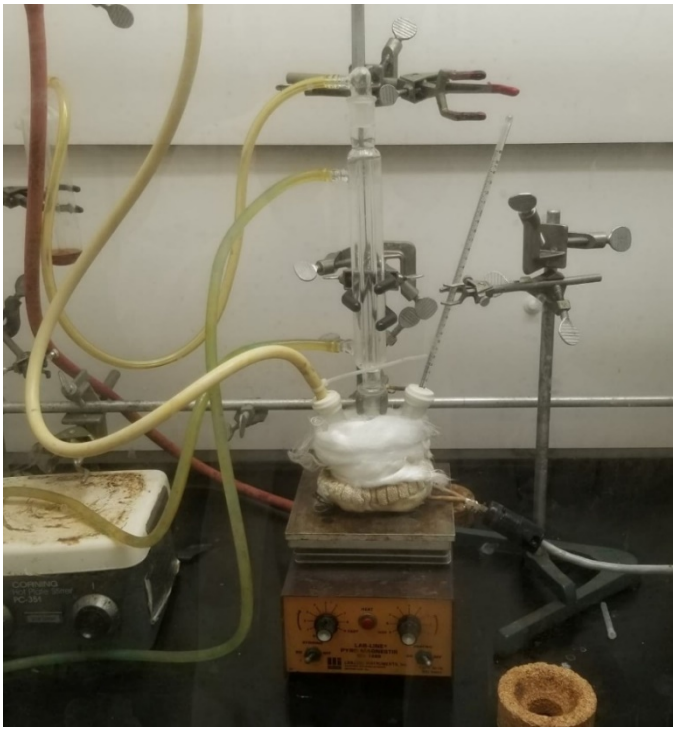

Figure 2. 2: Reflux condenser setup for colloidal synthesis

The thermocouple is then turned on with an electric potential of 140V and set to a desired temperature. The temperature was varied between synthesis from 160ºC, 180ºC and 200ºC. Once the desired temperature was reached the reaction was left to reflux for 1 hour. The crude sample is then placed into test tubes and washed with a mixture of ethanol and acetone using 4-5 centrifugation cycles. For surface treatment 2 g of TOPO is then added to each test tube and the sample is TOPO treated at 90ºC for 1 hour. The sample is then washed as previously described and dispersed into hexane.

The synthesis of cerium oxide and lanthanide cerium oxide colloidal particles was done in a similar method with slight deviations. With using the precursors $Ce(acac)_3$, $Er(acac)_3$, $Gd(acac)_3$ and $TbCl_3$ in tandem with using a two-part solvent of 4g of OAM and 2g of OA. Experiments were done to determine the best reaction temperature. The samples were then surface treated similarly to gallium oxide, however different surface modifiers were used on pure CNPs to test their effects. TOPO, OA, DDA, DHA, Tri-butylphosphine (TBP) were used for surface treatment in a similar method described earlier.

2.4 Synthesis of Ce^{3+} TOPO Complexes

The synthesis of Ce^{3+} TOPO complexes was down using a similar reflux setup previously explained. $Ce(acac)_3$ precursor is added to a 3-neck round bottom flask with TOPO and octadecene as solvents. The reaction mixture was heated to 85ºC and reflux under N_2 gas flow for 15-30 min. The resulting mixture was then washed several times with ethanol and the purified product was dispersed in hexane.

2.5 Characterization Techniques

2.51 X-ray Powder Diffraction (XRD)

XRD is an effective technique used to identify the three-dimensional crystal structure of NPs. From an XRD spectrum the size of a NP can be calculated based on the Debye-Scherrer equation[13]:

$$L_{hkl} = \frac{K\lambda}{\beta\cos(\theta)} \quad \textbf{(Eq. 2)}$$

Where L_{hkl} is the average crystalline size of the NP, K is a dimensionless shape factor, λ is the wavelength of the X-ray, β is the full width half-maximum of an XRD peak, and θ is the Bragg's angle.[11] The XRD used during this project for all samples were an INEL XRD diffractometer with a position sensitive detector and monochromatic Cu-Kα radiation ($\lambda = 1.5406$ Å) from UW professor Dr. Holger Kleinke's group in the Department of Chemistry.

2.52 Ultraviolet-Visible-Near-Infrared (UV-Vis-NIR) Spectroscopy

UV-Vis-NIR spectroscopy is a common technique used to measure the absorption for a variety of samples including NPs. During this project a Varian Carey 5000 UV-vis-NIR spectrophotometer was used to measure the band gap absorption of our samples. A cuvette sample holder was used instead of a solid sample holder, as our samples are dispersed in solvent. The spectrophotometer has a wide range of 175 nm to 3300 nm, which is necessary as it encompasses the UV range.

From the absorption spectrum, the optical band gap can be evaluated using TAUC's relation[21]:

$$(\alpha h\nu)^{\frac{1}{r}} = C(h\nu - Eg) \quad \textbf{(Eq. 3)}$$

Where C is a constant, α is a molar extinction coefficient, E_g is the average band gap, and r is the type of transition, where here r = ½ for direct band gap transition.[21] From TAUC's relation a TAUC plot can be made to evaluate the band gap energy.

2.53 Photoluminescence (PL) Spectroscopy

PL spectroscopy is a technique used to measure the excitation and emission spectra of a sample to determine its PL. During this project a Varian Carry Eclipse Fluorescence Spectrophotometer is used to measure the fluorescence and phosphorescence of our samples. Like the UV-Vis-NIR a cuvette sample holder is used, and the spectrophotometer has a wide range of 175 nm to 3300 nm. For low temperature measurements a cryostat was used to hold samples and liquid nitrogen and helium were used to cool samples down to 5K.

2.54 Transition Electron Microscopy (TEM)

TEM is a powerful tool used to observe the morphology, crystal structure and NP size of a sample. A high energy beam of electrons is passed through a sample where the interactions between the electron and atoms of the sample produce a high-resolution image that can be studied. TEM used were from UW Department of Biology for Ga_2O_3 NPs and McMaster University for CNPs.

2.55 X-ray Photoelectron Spectroscopy (XPS)

XPS is a technique that utilizes the photoelectric effect to determine the elements that exist within a material or on the surface, as well as their chemical state, electronic structure, and density of states in said material. The incident X-rays from XPS cause electron emission where the kinetic energy of the emitted electron is measured. The binding energy of the emitted electrons can be calculated using the photoelectric effect equation. XPS is used here to determine the elements, their oxidation states, and density of certain elements on a materials surface.

2.56 Photoluminescence Quantum Yield Measurements (PLQY)

The comparative method is used here, which involves the use of a well characterized standards/references with known QY to be compared to a sample with an unknown QY.[24] Solutions of the standard and unknown samples with identical absorption intensity excited at the same excitation wavelength can be assumed to be absorbing the same number of photons. By using an equation for the ratio of the integrated fluorescence intensities of the two solutions (recorded under identical conditions) will yield the ratio of the quantum yield values. Because the QY of the reference is known it is then to calculate the QY of an unknown. The ratio can be described by the equation:

$$\Phi_x = \Phi_{ST}\left(\frac{Grad_x}{Grad_{ST}}\right)\left(\frac{n_x^2}{n_{ST}^2}\right) \quad \textbf{(Eq.4)}$$

Where X and ST subscripts represent the unknown and standard respectively. Φ represents the quantum yield. Grad is the gradient from the plot of integrated fluorescence intensity vs absorption. N is the index of refraction of the solvents used for both samples.

For the experiments here a standard of quinine bisulfate (QBS) was used. QBS when dissolved in 0.05M H_2SO_4 has a QY of 54.6% at an excitation range of 300-360 nm. The samples studied in this thesis will be excited in the same range, making QBS a good reference for PLQY studies here.

2.57 Fourier Transform Infrared Spectroscopy (FTIR)

FTIR is a technique that measures the absorption or the transmittance of a solid, liquid or gas. The FTIR used herein the thesis was an attenuated total reflectance (ATR) FTIR. The ATR accessory measures changes that occur in an internally reflected IR beam after the beam has contacted the sample. The FTIR used measures within the range of 0 to 4000 cm^{-1}.

Chapter 3.0 Cerium Oxide Results and Discussion

3.1 Structural Analysis of Cerium Oxide NPs

3.11 XRD

XRD spectra were recorded for CNPs. Here the XRD for TOPO treated and non surface treated CNPs are shown. XRD in **Figure 3.1** shows that NPs synthesized here have the crystal structure of CeO_2 (bulk refraction pattern is shown as red lines). However, the broadness of peaks indicate that the particles are very small.

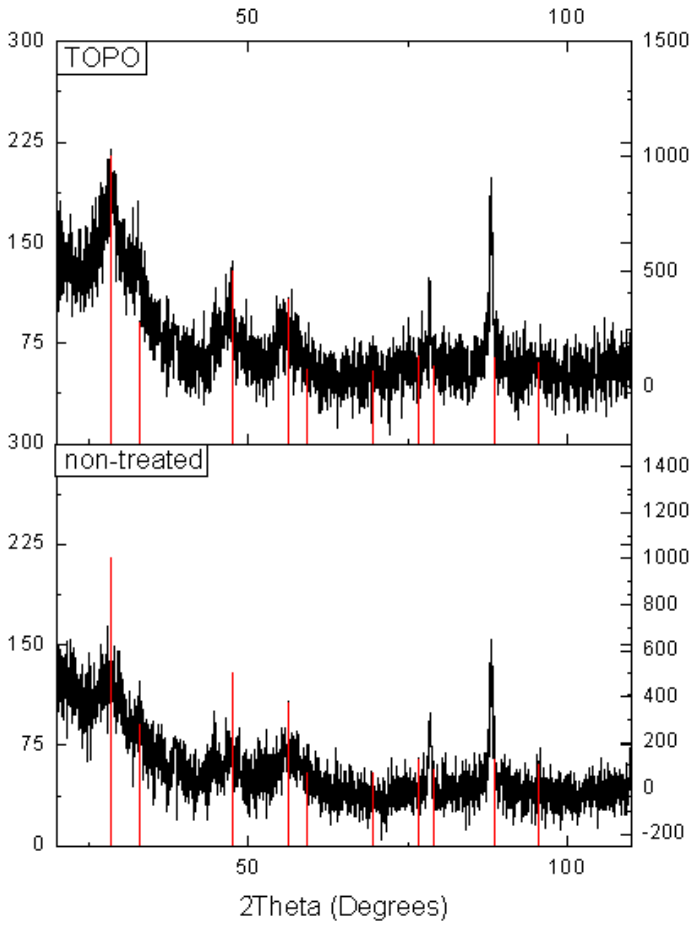

Figure 3. 1: XRD of TOPO and non-treated CNPs. Red lines indicate CeO_2 structure.

3.12 TEM

Reference CeO_2	
Plane	d-spacing
111	3.12
002	2.71
022	1.91
113	1.63
222	1.56
004	1.35

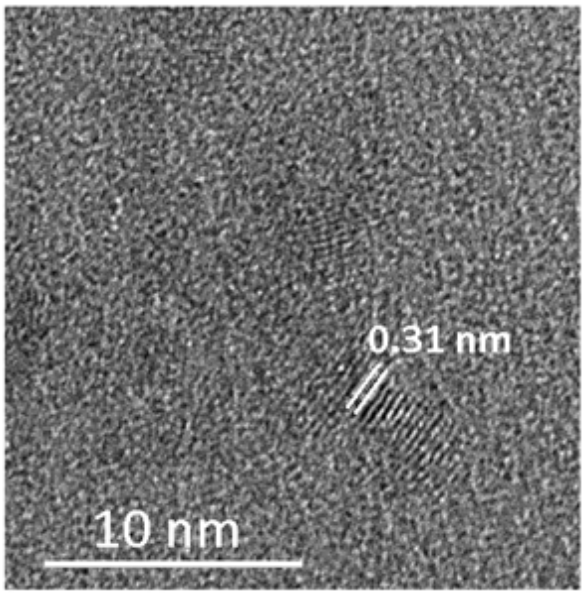

Figure 3. 2: HR-TEM images of CeO_2 TOPO treated samples and the d-spacing for CeO_2 planes.[68]

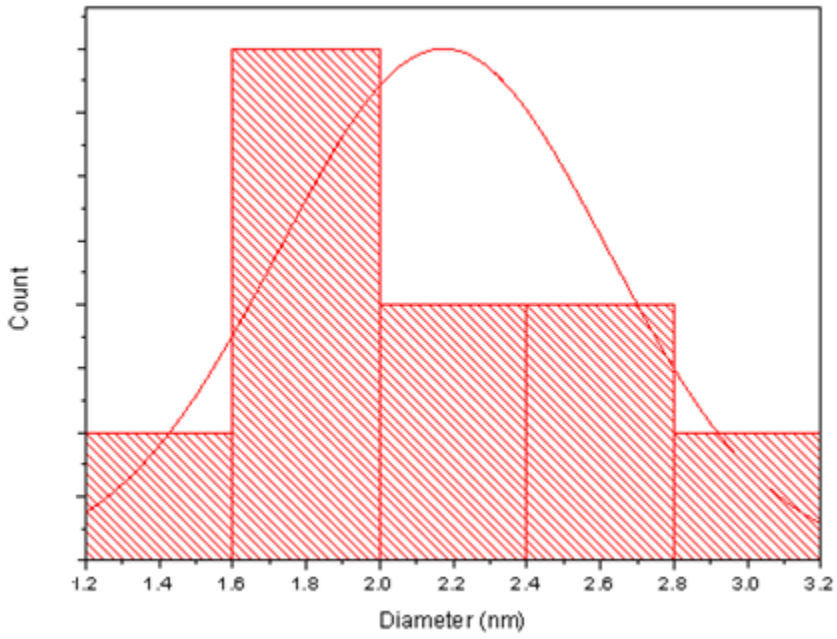

Figure 3. 3: Average sizes of CeO_2 NPs.

The HR-TEM data shows CNPs of varying size. Particles were analyzed in multiple HR-TEM images. From the HR-TEM images it was determined that the particle size is mostly between 2-3 nm which is well below the Bohr exciton radius of cerium oxide.[69] The d-spacing was also

determined to be 0.31 nm or 3.10 angstroms, which agrees with literature values of 3.12 angstroms for the d-spacing in the {111} plane.[70] This indicates in tandem with XRD data that the NPs indeed adopts the CeO_2 crystal structure.

3.13 XPS

XPS studies were done on TOPO treated samples. The XPS spectra were deconvoluted using the CasaXPS software and baseline corrected using a U4 Tougaard method. After deconvoluting and comparing to literature, most of the integrated intensity is composed of Ce^{3+} peaks.[40] According to Burrough's convention, the six peaks associated with Ce^{3+} are designated as u + u″ + u‴ + v + v″ + v‴ and the four associated with Ce^{3+} are represented as u^0 + u′ + v^0 + v′.[63] Comparing the main peaks of both Ce^{3+} and Ce^{4+} the calculated ratio is 80% Ce^{3+} to 20% Ce^{4+}, which when compared to literature is much larger then previously recorded.[39] The large amount of Ce^{3+} here demonstrate that the synthesis was successful in reducing the surface of cerium oxide by OAM and produced samples with largely Ce^{3+} on the surface.[48]

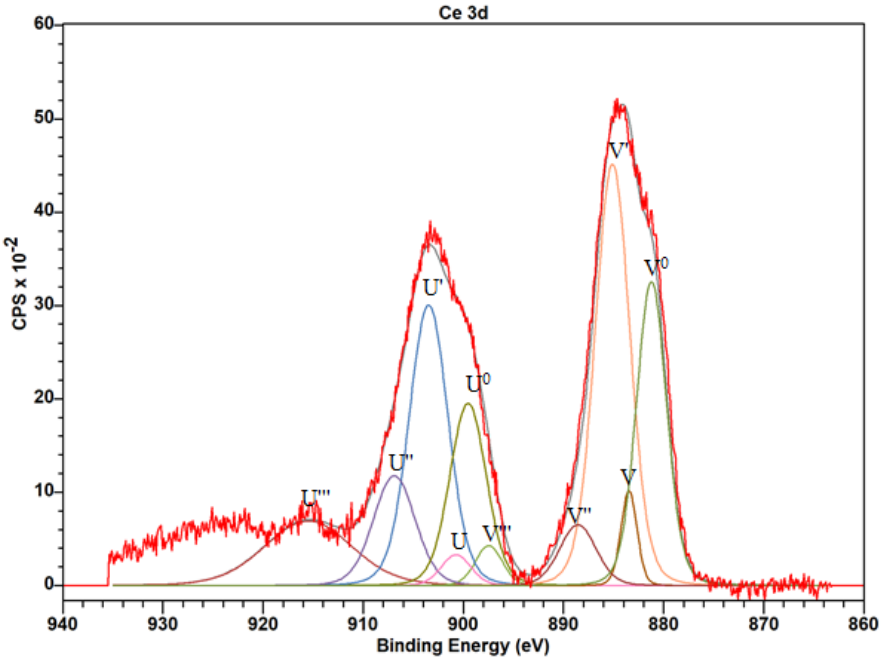

Ce 3+	Binding Energy (eV)
U'	903.4779
U^0	899.5365
V'	885.1127
V^0	881.2185

Ce 4+	Binding Energy (eV)
U'''	915.4808
U''	906.9022
U	900.7186
V'''	897.4589
V''	888.5628
V	883.4658

Figure 3. 4: XPS spectrum of cerium oxide Ce 3d. Peak position of Ce^{3+} and Ce^{4+} peaks are shown in the legend in the inset.

3.14 FTIR

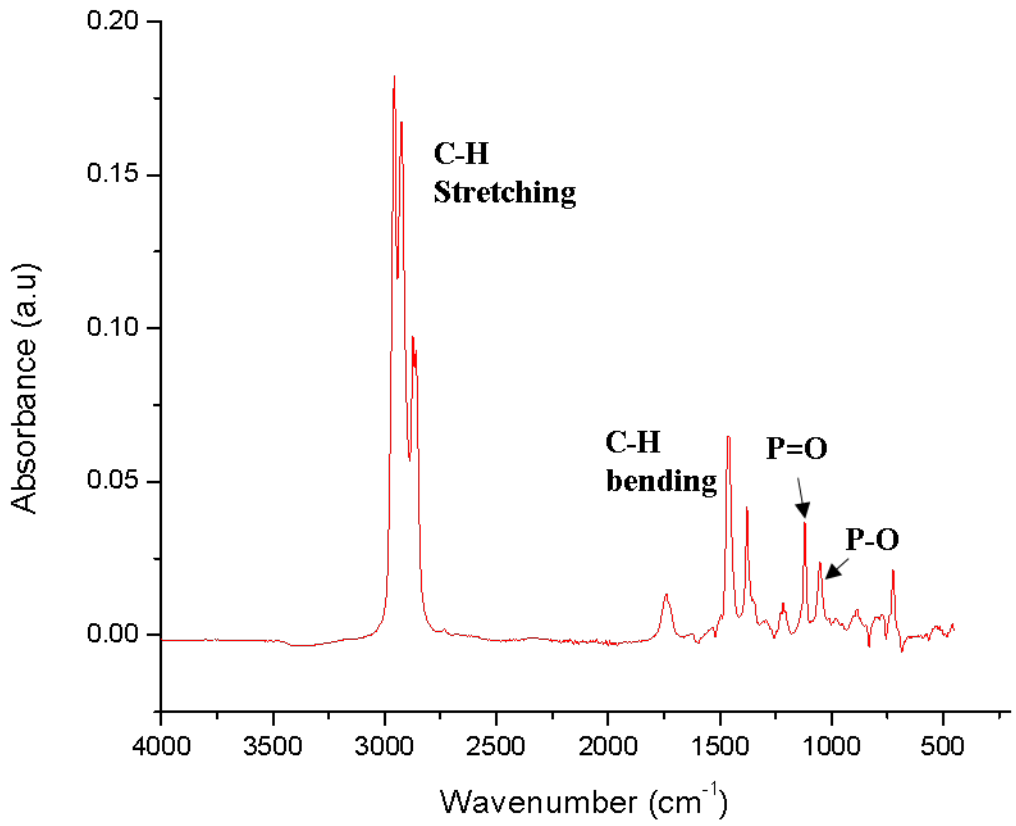

Figure 3. 5: FTIR absorption spectrum of TOPO CNPs using ATR.

Figure 3.5 shows the FTIR spectra for the TOPO treated CNPs. The measurement was done on CNPs dispersed in hexane. The peaks at 3000 cm^{-1} and 1500-1700 cm^{-1} can be attributed to the hexane solvent C-H stretching and bending, respectively. The peaks at 1120 cm^{-1} and 1048 cm^{-1} are attributed to P=O and P-O stretching, respectively.[71] The P=O and P-O stretching is a result of the TOPO treatment. The results in tandem with XRD and TEM confirms the crystal structure of the CNPs and that the CNPs have been successfully surface treated with TOPO ligands. Taken together, the results indicate a CeO_2 bulk crystal structure with high amounts of Ce^{3+} on the surface including the presence of TOPO ligands.

3.2 Optical Properties of Cerium Oxide NPs

3.21 PL of Surface Treated CNPs

Varying surface ligand exchanges were used following colloidal synthesis. Several ligands such as TOPO, dodecanedioic acid (DDA), docosahexaenoic acid (DHA), TBP, OA and others. Firstly, the phosphorus (TOPO, TBP) ligands were used. Studies have demonstrated that phosphoryl and phosphate groups were able to inhibit the segregation and oxidation of Ce^{3+} to Ce^{4+}.[39,72] From the optical data **(Figure 3.6**) for the TOPO modified CNPs there was an emission centred at 370 nm and absorption peak at 300 nm. Each sample was excited by an excitation wavelength of 300 nm and absorption of each samples were standardized to control concentration. When compared to most cerium oxide studies this emission is much more UV shifted.[73] The TOPO samples have a much sharper peak compared to other surface treated samples. The sharpness of the absorption band of TOPO CNPs indicates that there is a transition of energy states involved with the surface ligand that overpowers other transitions such as possible band-to-band transitions and so the TOPO samples have a much more defined transition that occurs in the UV region. the PL spectra TOPO CNPs had the highest intensity by far compared to other surface treated CNPs. For the untreated and other ligand treated samples such as carboxylic acid ligand (OA) and amine ligands (DDA and DHA), they did not result in emitting particles and so are not discussed into detail here. The result demonstrates the key factor of phosphorus oxide ligands in the resulting PL emission. At the time the mechanism of this novel UV emission has not yet been completely elucidated however, the hypothesis is that there is a MLCT that occurs between Ce^{3+} and oxygen, and Ce^{3+} intracentre transition (5d-4f) could also be involved. This theory will be further investigated in the following sections.

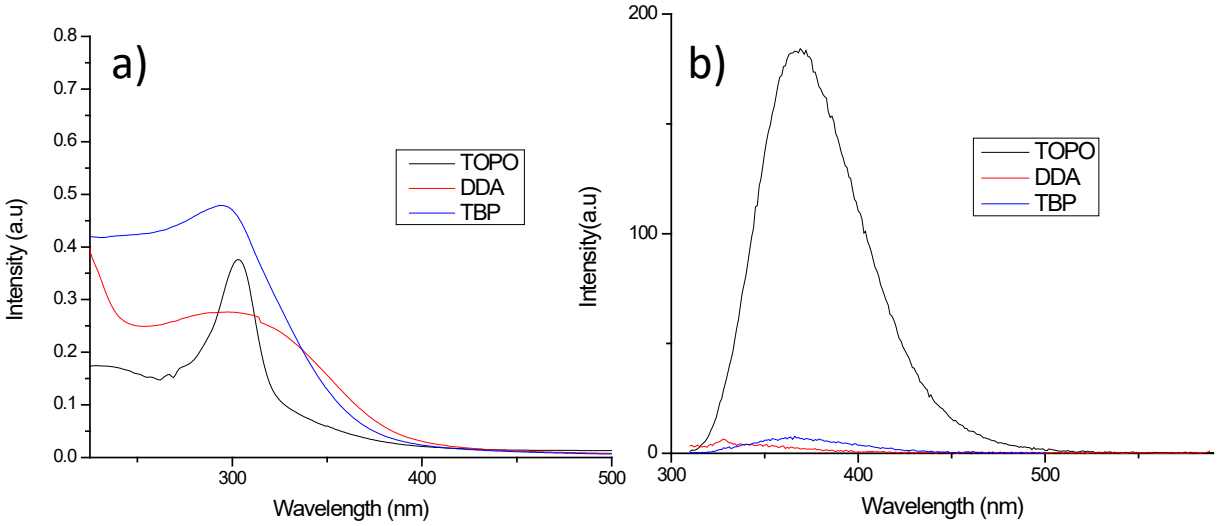

Figure 3. 6: Absorption (a) and PL spectra (b) of varying surface treated CNPs.

3.22 Temperature Dependent Synthesis and PLQY of TOPO CNPs

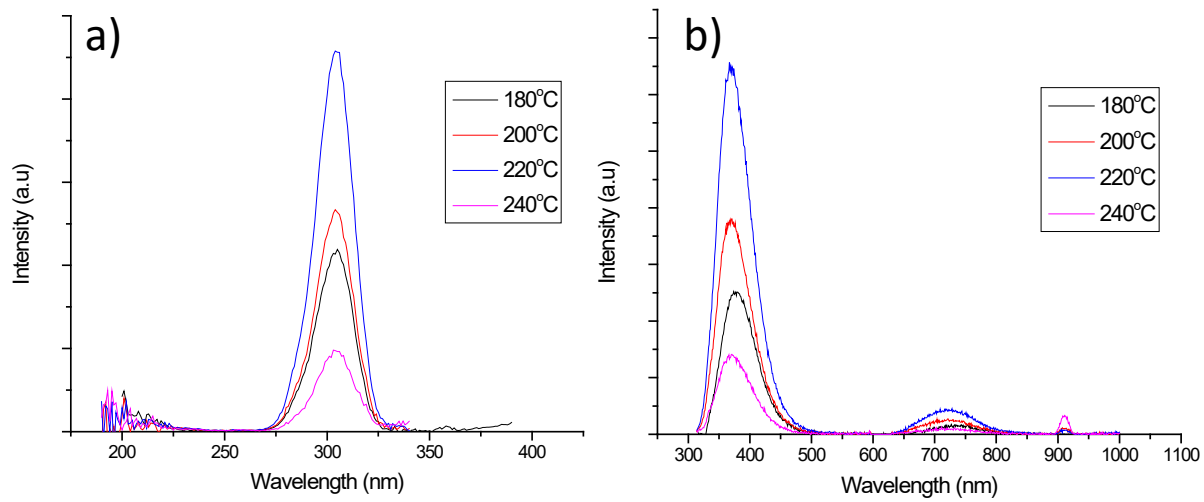

Figure 3. 7: Excitation (a) and emission spectra (b) of TOPO CNPs synthesized at varying temperatures.

Figure 3.7 compares the PL spectrum of CNPs synthesized at several different temperatures. The experiment was done as a control to determine the best temperature for growth and PLQY of TOPO treated CNPs. 180ºC is chosen as a baseline as many pieces of literature have demonstrated that it is a minimum temperature required for the formation of CeO_2 NPs. Temperature has been well-established to increase the size of particles as it is increased.[10] To provide NPs with large enough surface area for substantial MLCT but still small enough to produce phenomenon such as quantum confinement. The PL spectrum in **Figure 3.7** show that the intensity of PL or PLQY of samples synthesized at 220ºC is the highest compared to all other temperatures probed. Furthermore, there is a significant drop off in intensity at 240ºC attributed to larger particle size leading to aggregation and lower surface area for MLCT. The data indicates that the optimal temperature for synthesis is determined to be 220ºC for TOPO treated CNP synthesis. When calculating PLQY it was determined that particles synthesized at 220ºC had the highest PLQY of ~20%.

3.23 Low Temperature Fluorescence Measurements

Cerium oxide has several emission risings from its multiple PL mechanisms. To determine if multiple emissions mechanisms are involved here and to compare to literature, low temperature fluorescence was done on 2hr synthesized TOPO treated CNPs, varying temperature from 300K-20K (**Figure 3.8**). Spectra at temperature's bellow 50K showed no discernable difference in emission. From low temperature measurements from a study by Bazhukova et al. (2019) showed at least three transitions involved, shown in **Figure 1.9**.[41] The most red-shifted transition is from O^{2-} (2p) to Ce^{4+}(4f) while the middle is from oxygen vacancies and the most blue-shifted is from Ce^{3+} intracentre transitions (5d-4f). From 300K to 20K there is an increase in intensity as well as emission shift into the UV region. Temperature patterns involving peak shift and integrated fluorescence can be seen in **Figures 3.9** and **3.10** where the Varshni fitting is shown and integrated area as temperature changes is described. The Varshni law describes the change in the energy bandgap of a semiconductor with temperature. The Varhsni fit was done using the equation[74]:

$$E_g = E_{g0} - \frac{AT^2}{B+T} \qquad \textbf{(Eq. 5)}$$

Where E_g and E_{g0} are the band gap energy in eV at varying temperatures and at 0K, respectively. T is temperature in Kelvin. A and B are material-specific parameters. Here the band gap at 0K was interpolated to be approximately the same as the band gap at 20K as no differences were seen in emission spectra under 20K. The Varhsni fit was simulated using the Origin program, the parameters A and B were floating parameters which were changed over several simulations to determine the best fit.

Examining the data collected here there are two peaks at 355nm and 385nm, found in the PL spectra at 20K indicating the presence of at least two transitions involved. The 385 nm peak

can be ascribed to Ce^{3+} intracentre transitions. Ce^{3+} transitions shown in literature where 20 nm sized CNPs were synthesized demonstrated emissions at approximately 3 eV or ~410 nm while from the data here of particles there is an emission at 385 nm.[59] The increase in energy could be due to quantum confinement as another study demonstrated an increase in direct band gap from 3.15 to 3.78 eV from the quantum confinement effect.[69] However, if the emission comes from local processes and not from the band gap of the NP itself quantum confinement would not play a significant role.

The most UV-shifted peak at 355nm is not been observed in literature and is UV shifted in comparison to what has been found for CNPs.[75] Several studies have demonstrated phosphorus-based charge transfer between metals and ligands.[76] Usually, the phosphorus is in the form of blue or black phosphorus, but literature is lacking in oxide phosphorus ligands as a source of CT.[76] From these studies and the results that only TOPO CNPs demonstrated a strong absorption band, the hypothesis is that the transition at 355 nm occurs due to charge transfer between surface Ce^{3+} and TOPO ligands.

Some studies have recorded a blue shift in emission as temperature is decreased which is also seen in the Varshni fit in **Figure 3.11**, however such a significant of a UV shift of CNP emission cannot be completely described by the Varshni law.[71] The UV emission reported here is remarkable for cerium oxide and has not been demonstrated in recent studies.

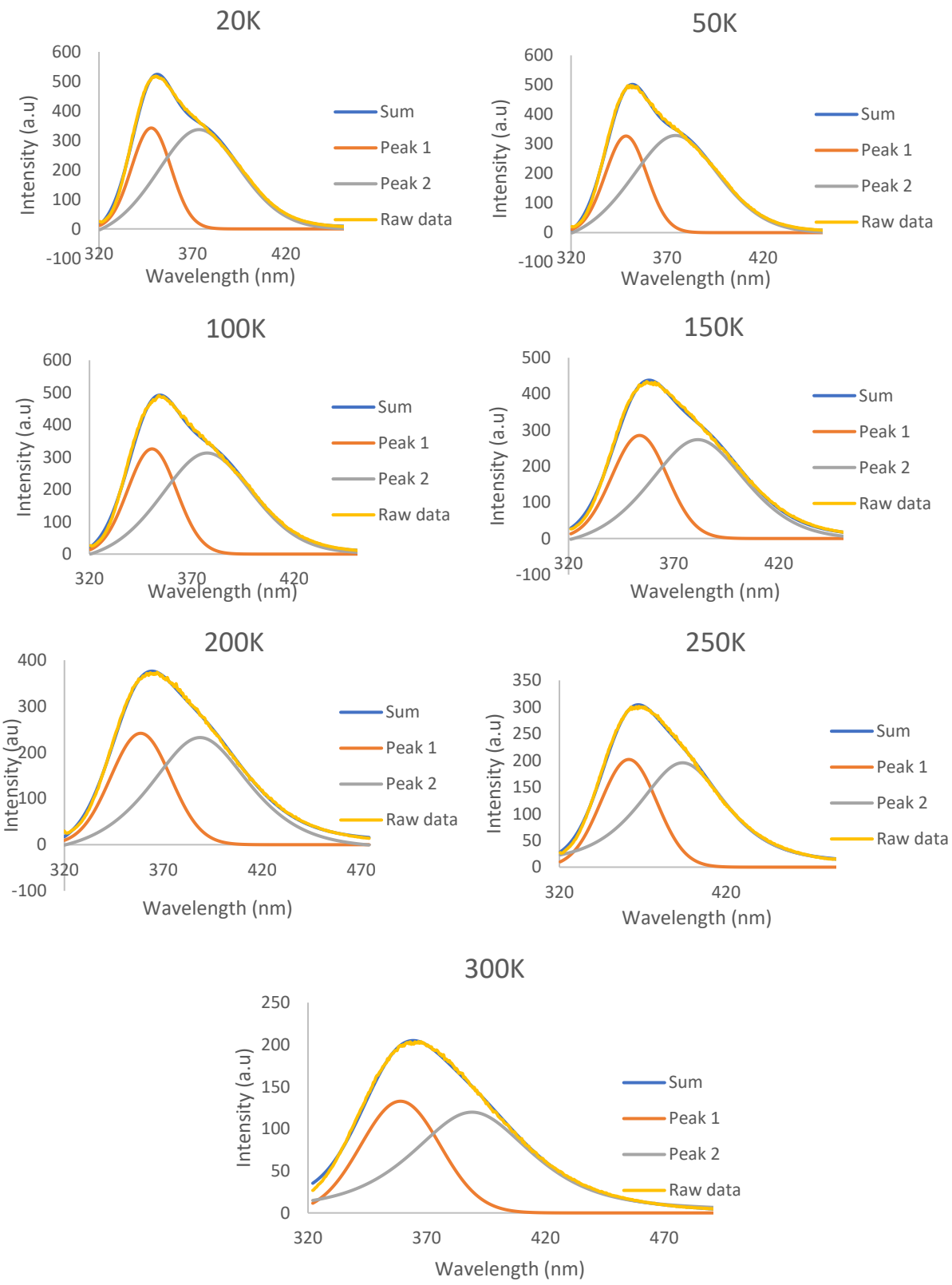

Figure 3. 8: Low temperature PL data of TOPO treated CNPs. 20K to 300K.

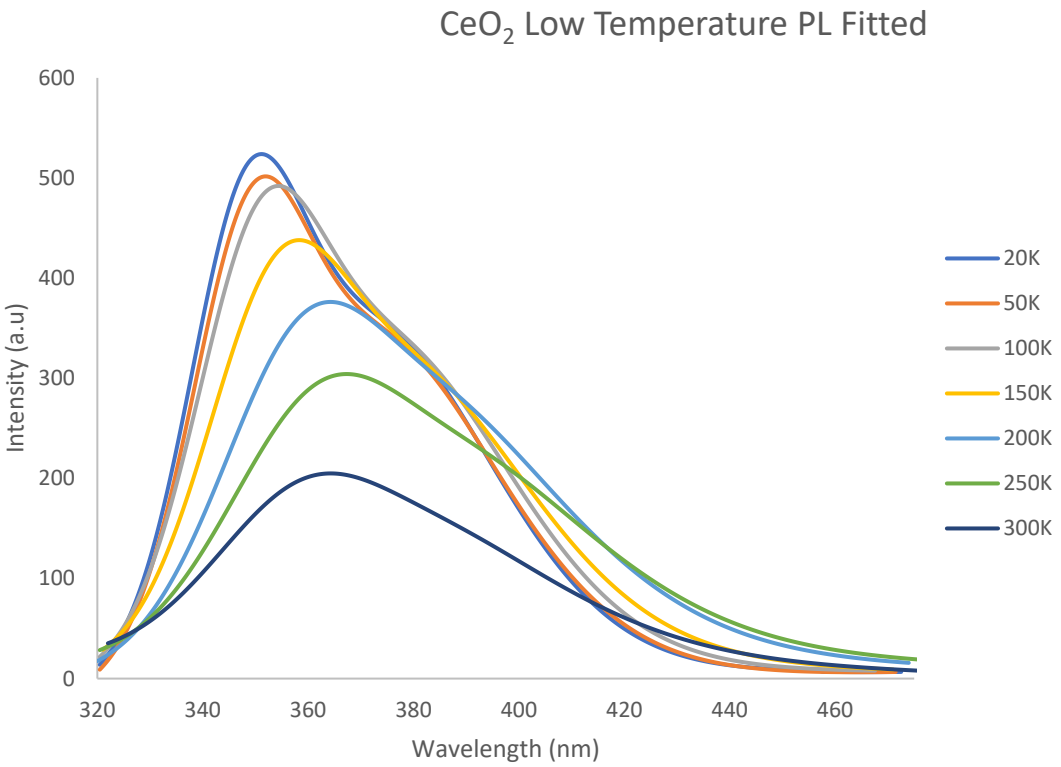

Figure 3. 9: Combine fitted curves of low temperature PL data.

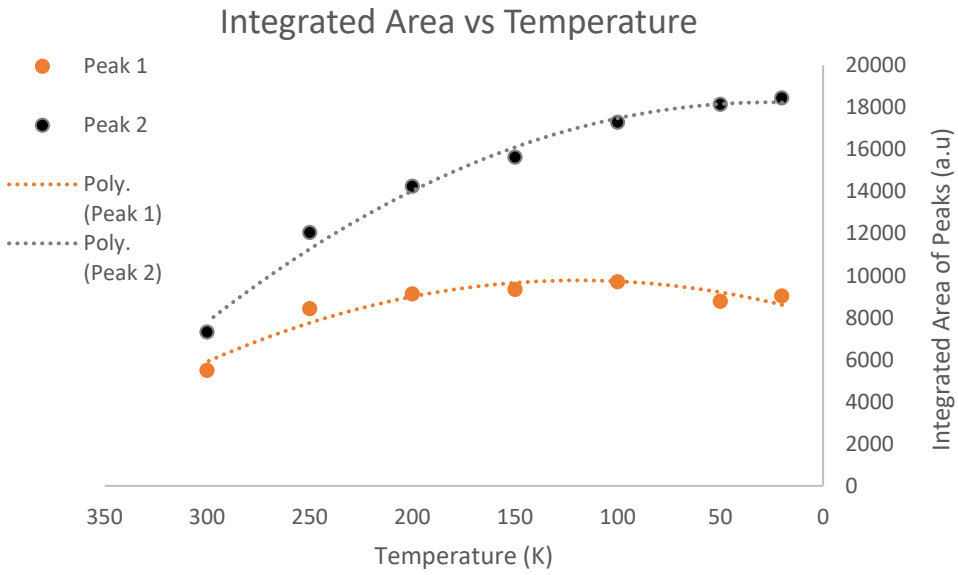

Figure 3. 10: Integrated area vs temperature of low temperature PL spectra for TOPO CNPs.

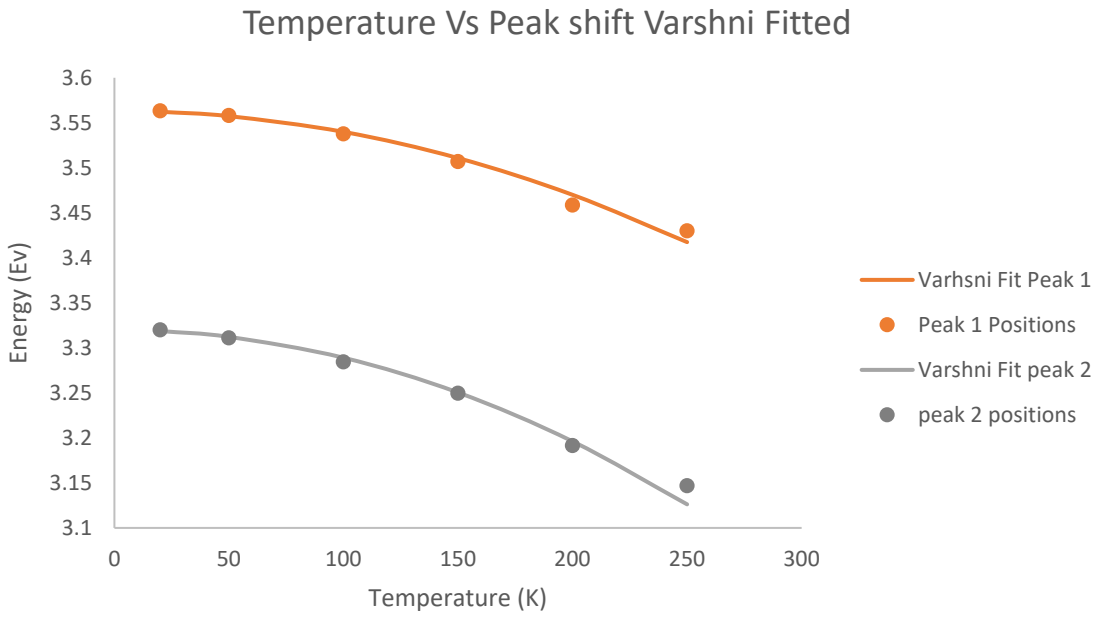

Figure 3. 11: Temperature vs peak shift and Varshni fitting of low temperature PL spectra of TOPO CNPs.

3.3 Ce^{3+} TOPO Complexes

To Further investigate the mechanism of the novel UV emission found in the TOPO treated CNPs, an alternative synthesis described in the experimental section was used to synthesize Ce^{3+} TOPO complexes depicted in **Figure 3.12**. A low temperature of <180ºC was used to prevent formation of NPs and to establish formation of complexes. This was done to determine if the mechanism is based on a MLCT as theorized earlier. The Ce^{3+} TOPO complexes were structurally analyzed using FTIR and XRD. The FTIR shows the presence of C-H, P-O and P=O stretching which indicate the presence of TOPO. The XRD did not show any discernable diffraction pattern of crystalline CeO_2, and any pattern seen is from background peaks, indicating that a macromolecule or complex was formed instead.

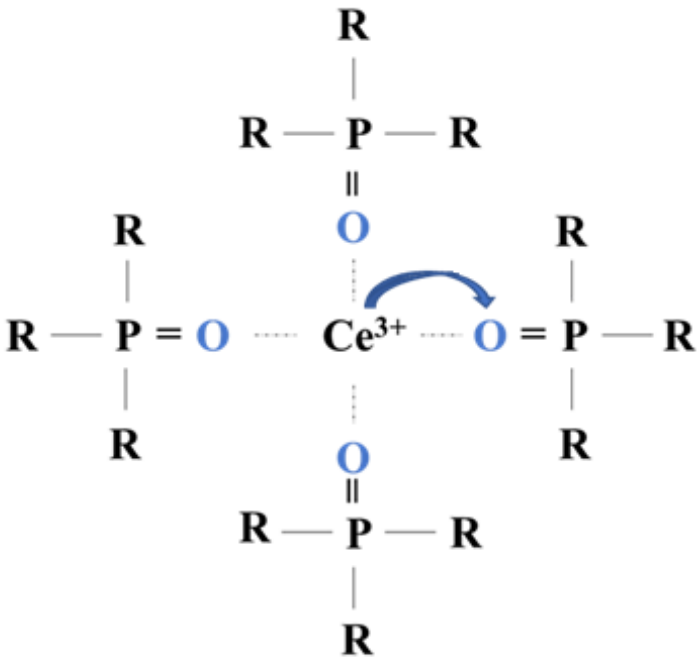

Figure 3. 12: Schematic diagram of proposed Ce^{3+} TOPO complex and arrows indicate possible MLCT between Ce^{3+} d-orbital electron and TOPO ligands.

Emission and absorption spectrum of the Ce^{3+} TOPO complexes are shown in **Figure 3.14**. The results show that the UV emission is present within the complex. The absorption band is also

very similar shape to what was found for TOPO CNPs in **Figure 3.6**. The results here give evidence of the theorized MLCT between Ce^{3+} and oxygen. Control experiments were also done on pure TOPO which did not show any signs of PL in the UV region. The results are indicative of the theorized MLCT and Ce^{3+} transitions as the mechanism behind the novel UV emission found in TOPO CNPs, as those are the only transitions available in the complex.

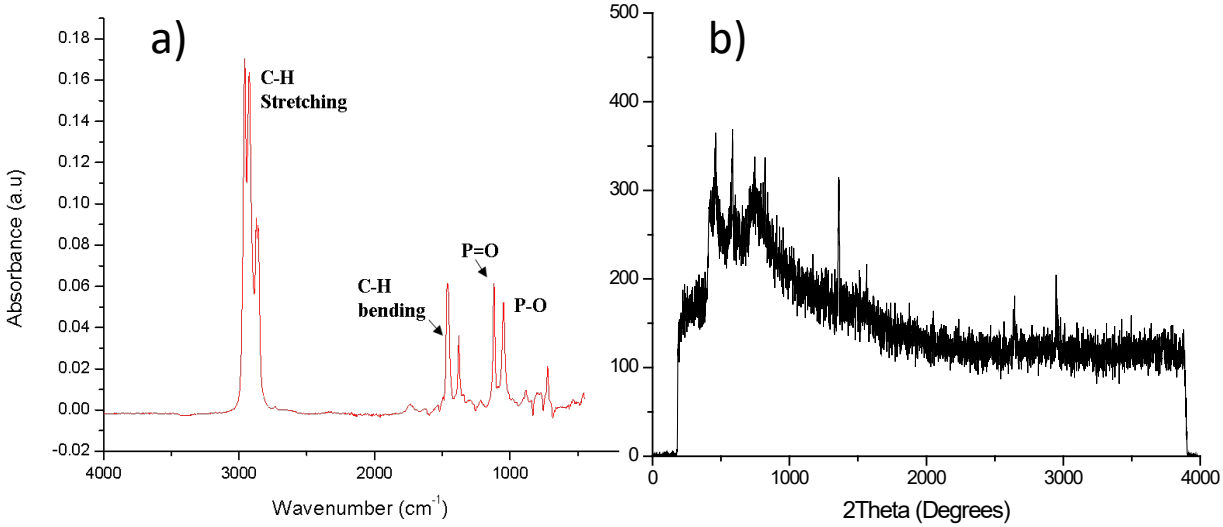

Figure 3. 14: FTIR (a) and XRD (b) of Ce^{3+} TOPO complexes.

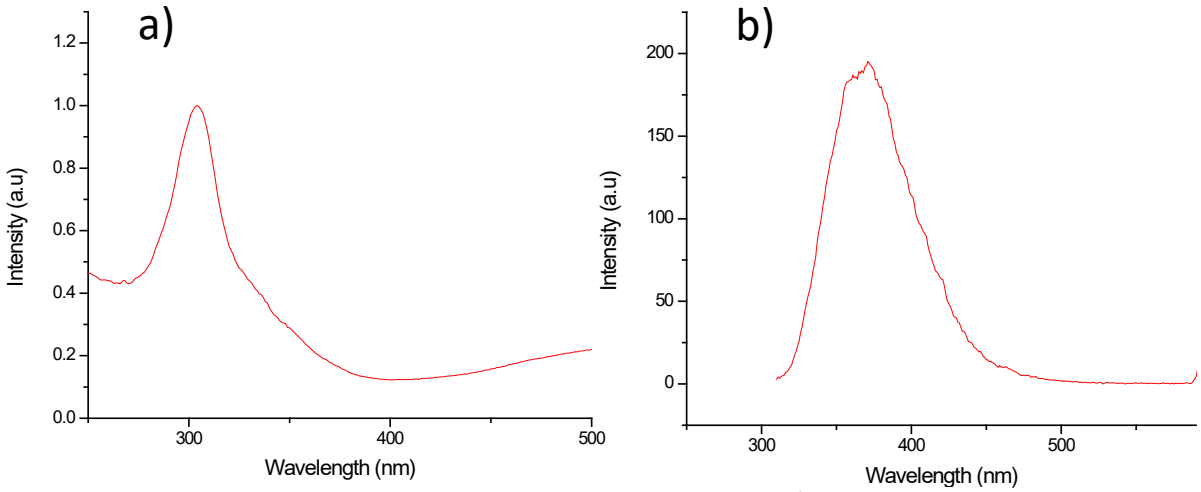

Figure 3. 13: Absorption (a) and PL emission spectra (b) of Ce^{3+} TOPO complexes.

3.4 Introduction of Lanthanides into CNPs

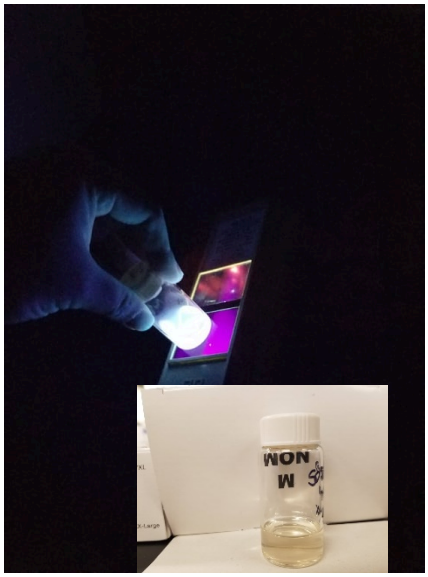

Figure 3. 15: Er-CNPs in colloidal suspension in hexane, white emission under UV excitation and under ambient lighting (inset).

To further investigate applications of CNPs the manipulation of CNPs through lanthanide doping was explored herein. White light emitting erbium cerium oxide nanoparticles (Er-CNPs) were synthesized via the colloidal method using 50% erbium to 50% cerium precursor ratio. Their absorption and PL spectra and CIE chromaticity is shown in the **Figures 3.16** and **3.17**. The photo in **Figure 3.15** shows TOPO treated Er-CNPs distributed in hexane under UV excitation and under ambient lighting. As the photo demonstrates the light emitting from the mixture under UV light is white while the sample under ambient lighting has a light brown/yellow hue. The PL spectra and the CIE diagram shows that the resulting light covers mostly the blue region peaking at 420 nm in the UV-vis and extends into the 500-600 nm region which results in the white light that is shown. An interesting finding is seen in the absorption and excitation spectra, as there are two defined transitions that can be seen at 255 nm and 320 nm. Interestingly, when exciting the sample at both 255 and 320 nm the PL spectra are the same, with the excitation at 320 nm resulting in a higher PLQY emission. The finding indicates that two transitions here give the same emission which can have interesting applicative uses. For example, the excitation source of 255 nm is very high and requires expensive UV LEDs however an excitation around 320 – 400 nm is a much more achievable and cost friendly. The emission is theorized to originate from a combination of cerium and erbium inter band gap states. Overall, the results demonstrate the tunability of cerium oxide by addition of lanthanide metals in this case erbium.

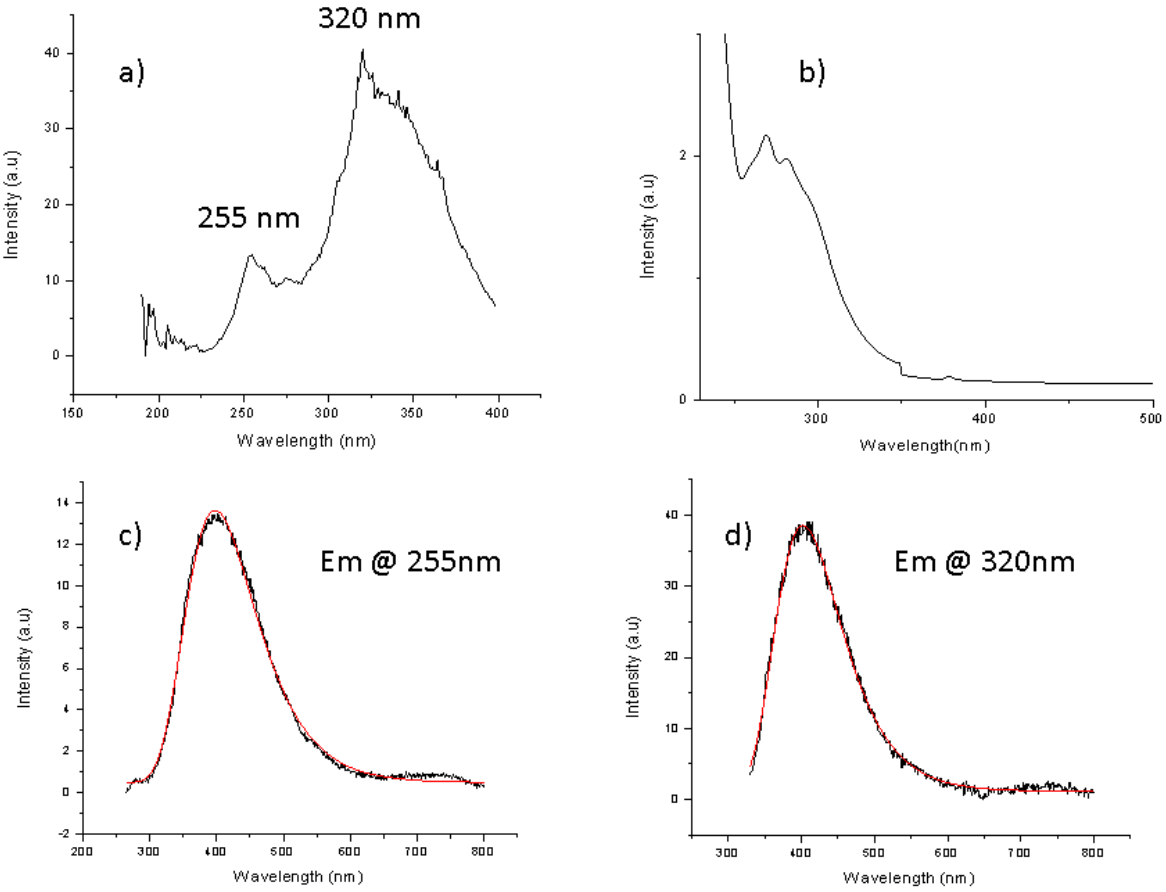

Figure 3. 16: Excitation(a), absorption (b), and emission spectra at 255 nm excitation (c) and 320 nm excitation (d) of Er-CNPs TOPO treated.

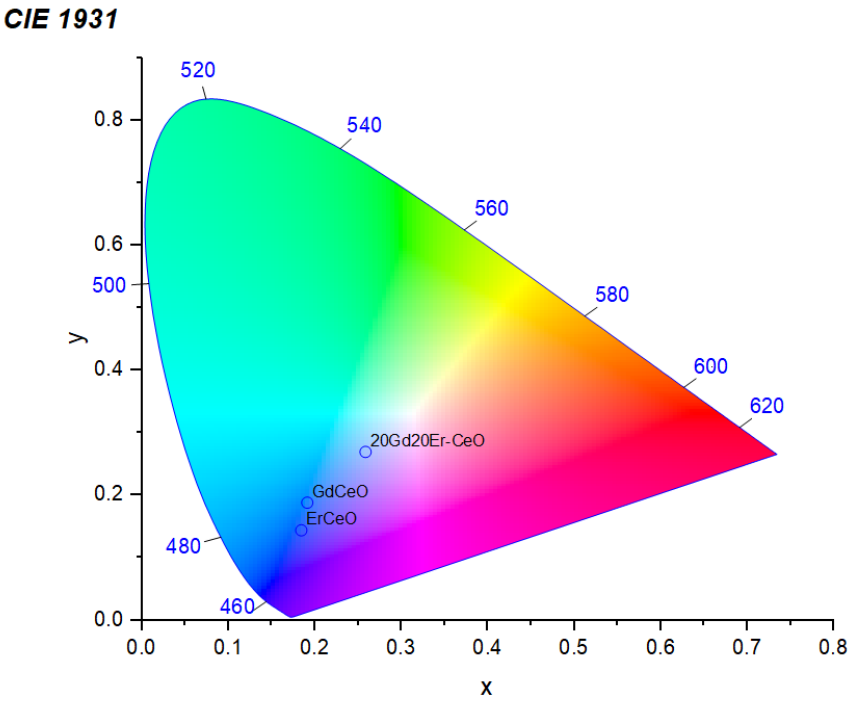

Figure 3. 17: CIE diagram of Varying Lanthanide CeO_2 NPs.

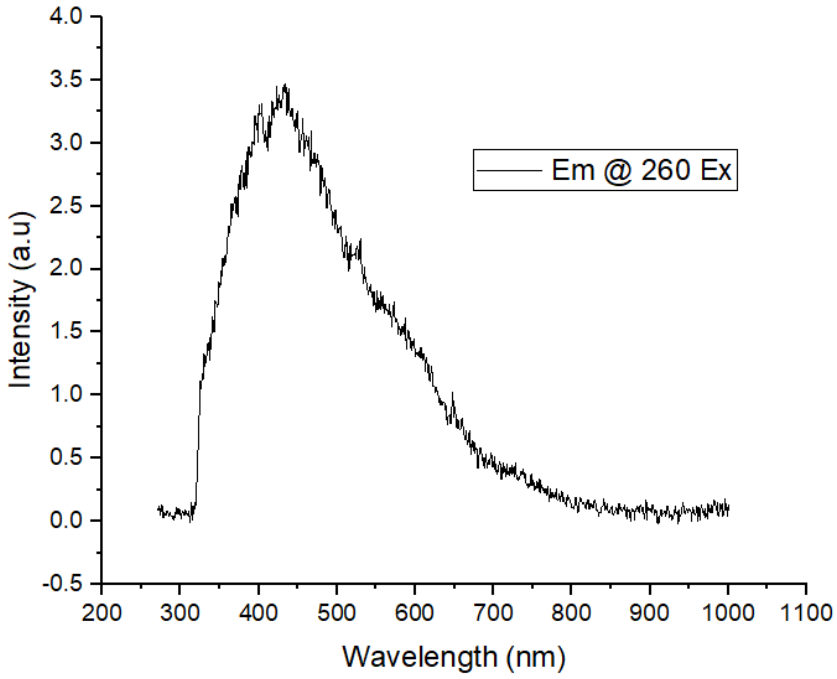

Figure 3. 18: PL emission spectra of GdEr-CNPs excited at 260 nm.

To further expand the PL range of the NPs in the visible region, multiple lanthanides were incorporated with cerium oxide to provide tunability. Er-CNPs showed considerable white light emission however, it is clear from the chromaticity diagram that the emission lacks red, and the quality of white light needs to be softened. Previous studies have shown that lanthanide co-doped systems with gadolinium demonstrated red shifts due to introduction of interstitial band gap states that provide the necessary energy levels for red or near IR light emissions.[77] Here in this study gadolinium (Gd) and Er were co-incorporated into cerium oxide to soften its white light and to further control the tunability of the NPs in the visible region. GdEr-CNPs were synthesized using 20% Gd, 20% Er and 60% Ce precursor molar ratios.

After excitation at 260 nm the spectra are broadened when compared to ECO. The GdEr-CNPs PL emission ranges from 300 – 700 nm (**Figure 3.18**) in contrast to 300-600 nm that is seen for ECO. After converting the spectra and plotting it onto a CIE diagram it is much closer to white light compared to ECO. However, when comparing PL intensity and quantum yield GdEr-CNPs has a much lower QY compared to the ECO. Unfortunately, the complete transitions involved for the white light emission have not yet been elucidated however, the results prove that white light emission is possible and tunable in cerium oxide and lanthanide systems. The results are useful in today's photonic applications and can lead to further discovery in the field.

3.41 Sensitized Lanthanides in TOPO CNPs

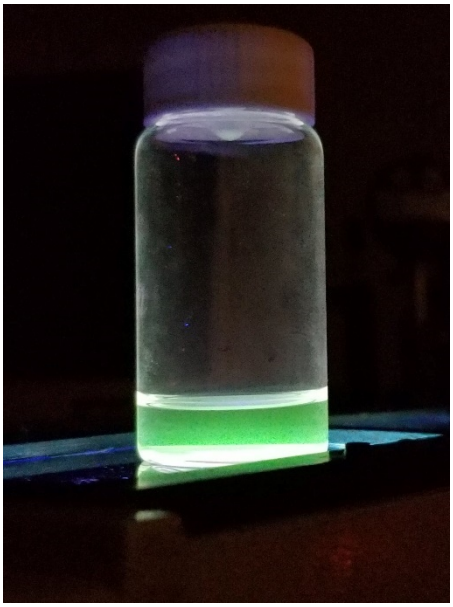

Figure 3. 19: Image of green emitting Tb-CNPs in colloidal suspension in hexane, under near UV excitation

The novel UV emission studied here is theorized to occur due to a MLCT from a molecular complex that does not require NP synthesis, however the presence of this UV emission in CNPs have been confirmed through analysis and this can be taken advantage of for various applications. To further investigate the application of TOPO CNPs, Tb^{3+}-doped CNPs were prepared, with the goal to sensitize lanthanide incorporated into CNPs as shown in the schematic bellow. Here in the thesis Tb^{3+} was attempted to be sensitized by the MLCT emission to produce a green emission. Ce^{3+} on the surface of CNPs excited by a UV source, causes a MLCT between Ce^{3+} and TOPO. The resulting MLCT UV-emission sensitizes and excites the Tb^{3+} doped

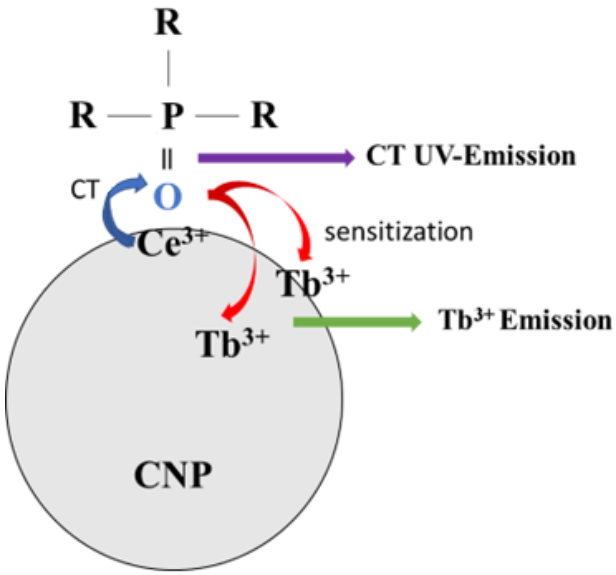

Figure 3. 20: CNP Schematic diagram of proposed sensitization and CT mechanism, where blue arrow indicates the MLCT leading to the UV-emission shown in purple arrows. The red arrows indicate the sensitization to excite surface or doped Tb^{3+} which leads to the Tb^{3+} emission depicted by the green arrow.

in the CNP host lattice or on the CNP surface causing a green Tb^{3+} emission which is depicted in **Figure 3.19**.

Figure 3.21 (a) compares the steady-state and time-gated PL spectra of 10% Tb^{3+} CNPs (Tb-CNPs) after excitation at 300 nm. As demonstrated earlier the steady-state PL spectrum is dominated by a broad band centered around 370 nm, which has been theorized to correspond to a Ce^{3+} MLCT. The time-gated spectrum is measured with a delay time of 0.1 ms and a gate time of 5 ms. After the 0.1 ms delay the MLCT has completely decayed, and the resulting spectrum only consist of Tb^{3+} emission patterns. The four major peaks at 620, 583, 550 and 490 nm can be attributed to Tb^{3+} $^5D_4 \rightarrow {}^7F_{3,4,5,6}$ intra-4f transitions, respectively. The 10% Tb^{3+} CNPs demonstrate relatively high incorporation or doping concentration because both the MLCT and Tb^{3+} emissions are observed in the steady-state spectrum. However, only one Tb^{3+} transition is observed at 550 nm in the steady-state spectrum. The data here indicates that the MLCT emission has a higher

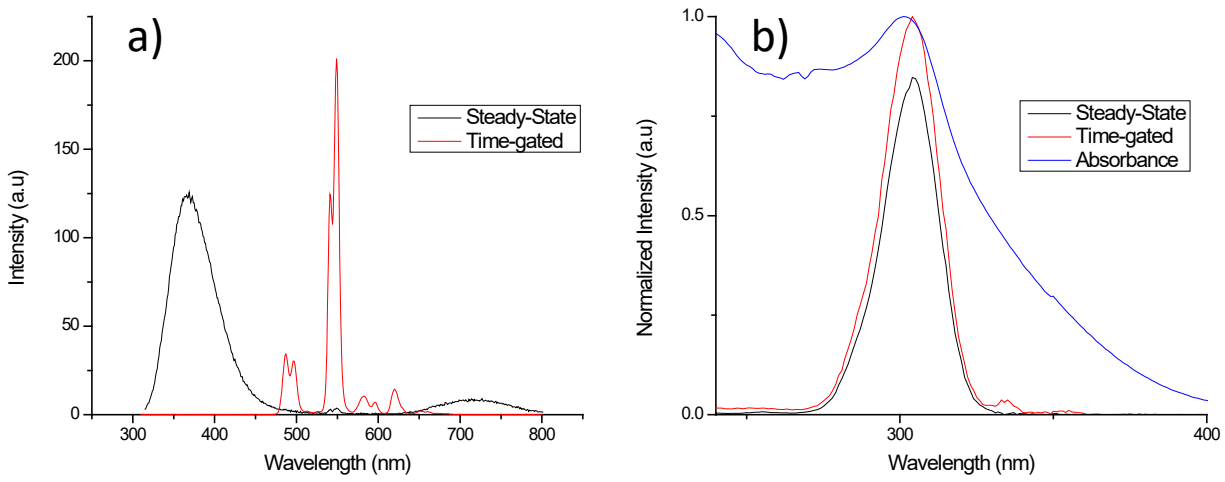

Figure 3. 21: Steady-state and time-gated PL emission (Ex = 300nm) spectrum of Tb-CNPs (a). Absorption and excitation spectra for steady-state (Em = 370nm) and time-gated (Em = 550nm) of Tb-CNPs (b).

intensity and a faster decay compared to the Tb^{3+} emission. Furthermore, observation of the Tb^{3+} transition by MLCT excitation indicates its sensitization by surface transitions on the NP. **Figure 3.21 (b)** demonstrates the absorption spectrum together with the steady-state and time-gated excitation spectra of Tb^{3+} CNPs from **Figure 3.21 (a)**, for the 370 nm and 550 nm (Tb^{3+} $^5D_4$ → $^7F_5$) emissions, respectively. The time-gated and steady-state excitation spectra are identical with the only difference between the two is intensity, showing a deep-UV peak at 304 nm, which coincides near the absorption edge which is attributed to the MLCT. The result confirms the sensitization of the Tb^{3+} by MLCT involved Ce^{3+} on the NPs surface.

3.42 Low Temperature Tb-CNPs PL

To examine the sensitization, including Tb^{3+} ion site symmetry and effect of TOPO on energy transfer, low temperature PL was performed on Tb-CNPs that were treated with one TOPO treatment (1x TOPO) vs three TOPO treatments (3x TOPO). Theoretically, the 3x TOPO Tb-CNPs should have a cleaner surface where less surface Tb^{3+} ions are available for sensitization. The low temperature data provides insight in the site symmetry and therefore the local environment of the

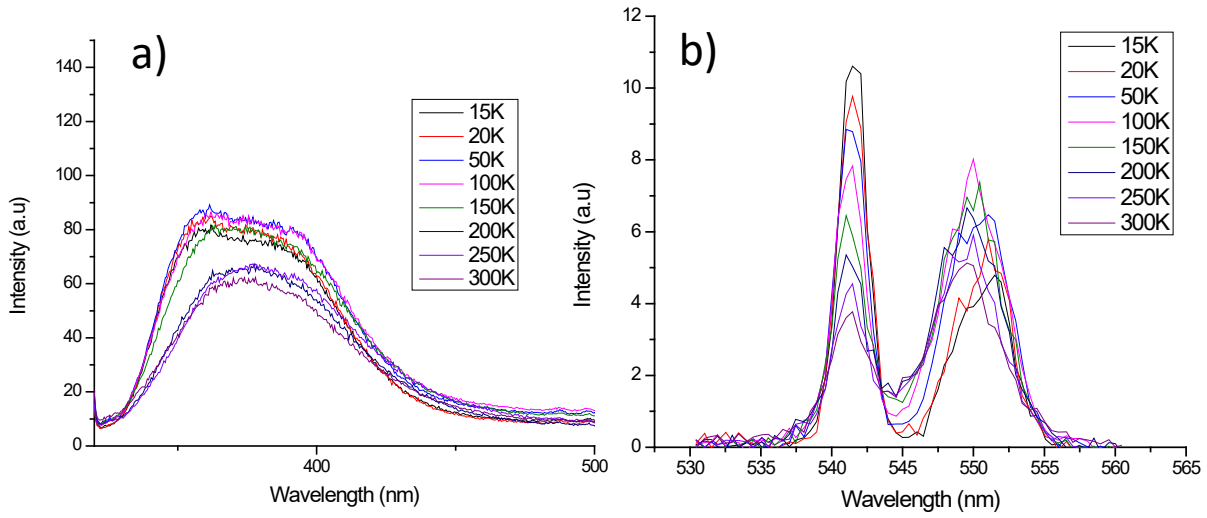

Figure 3. 22: Low temperature PL spectra of 3x TOPO 10Tb-CNPs of UV emission (a) and Tb^{3+} emission (b).

Tb^{3+}. Measurements were done at 15K-300K for 3x TOPO samples while a temperature range of 50K-300K were used for 1x TOPO.

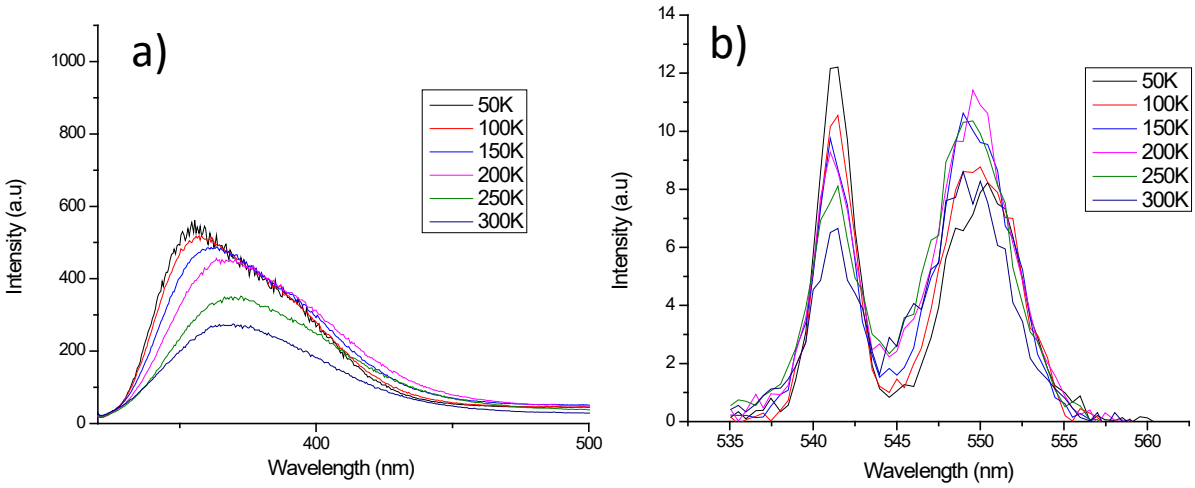

Figure 3. 23: Low temperature PL spectra of 1x TOPO 10Tb-CNPs of UV emission (a) and Tb^{3+} emission (b).

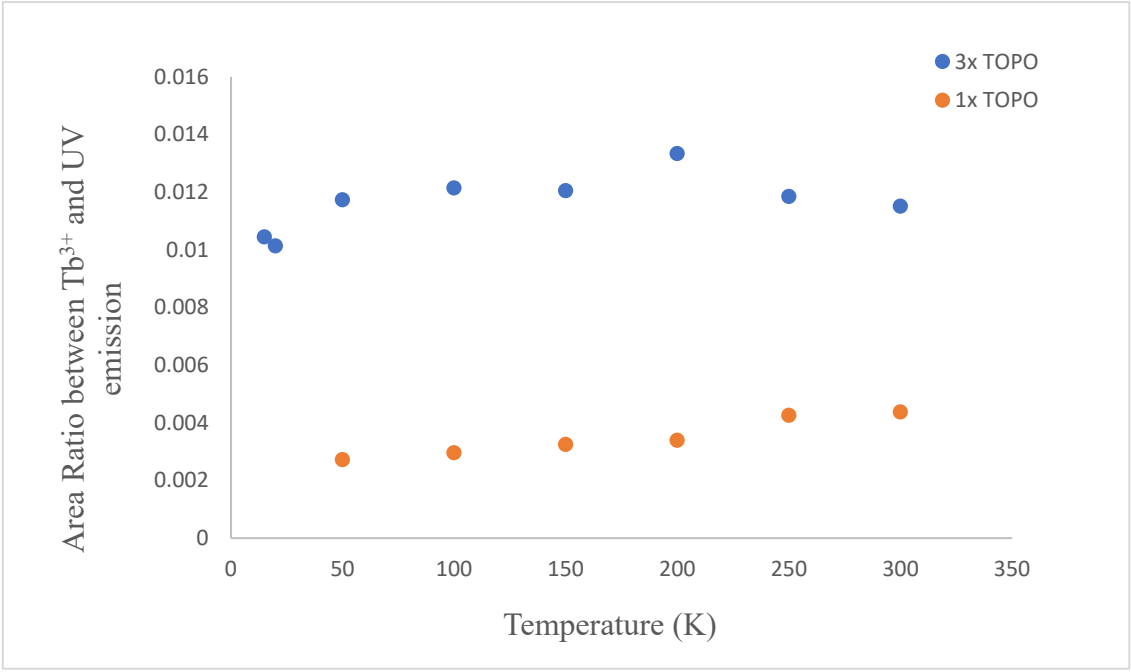

Figure 3. 24: Area ratio between UV and Tb^{3+} Emission vs Temperature of 1x and 3x TOPO samples.

The steady-state PL spectra at low temperature for 1x and 3x TOPO Tb-CNPs are shown in **Figure 3.22** and **3.23**. The band shape of 1x TOPO Tb-CNPs UV emission in **Figure 3.23 (a)** resembles the same band shape as seen in undoped TOPO CNPs. Where a shoulder appears at low temperature indicating the two proposed transitions of Ce^{3+} intra centre transitions in the 385 nm region and a MLCT in the 355 nm region. An important difference is found in the 3x TOPO samples in **Figure 3.22 (a)** where the band shape significantly differs from that in **Figure 3.23 (a)** such that the MLCT peak in the 350 nm region is quenched and the Ce^{3+} intracentre transition is more discernable. The quenching of the MLCT in **Figure 3.22 (a)** can be explained by an increase in energy transfer and therefore sensitization of Tb^{3+}, as an increase in energy transfer between MLCT and Tb^{3+} would result in a quenching and decrease of the MLCT intensity and an increase in the Tb^{3+} emission. To further confirm this the integrated area ratio between the Tb^{3+} and UV emission for both 1x and 3x TOPO samples and was plotted as a function of temperature in **Figure 3.24**. The results show that temperature did not change the ratio significantly and that the ratio was higher for 3x TOPO samples, indicating that there was an increase in sensitization and therefore, an increase in the Tb^{3+} emission. The increasing amount of TOPO on the surface through 3x treatment could increase the sensitization by simply creating more sites for MLCT on the surface and therefore increasing the probability that energy transfer will occur with internal or surface Tb^{3+} ions. Loosely bound Tb^{3+} could also coordinate to the surface of the NP increasing Tb^{3+} sites for energy transfer as well, increasing the efficiency of energy transfer. To further indicate if Tb^{3+} is being sensitized more in the 3x TOPO treated samples, absorption and PL emission spectra were collected for 3x and 1x TOPO treated samples at similar concentrations in colloidal suspension. The results are shown in **Figure 3.25** and from the spectra it is difficult to determine if there are any significant differences. However, after calculating integrated areas of both UV and Tb^{3+} peaks

for the 3x and 1x TOPO treated samples the ratio between Tb^{3+} to UV emission were determined to be 0.00507 and 0.00387, respectively. Because the 3x TOPO samples have a higher value for this ratio, it indicates that the 3x TOPO treated samples have a higher Tb^{3+} emission and therefore better sensitization.

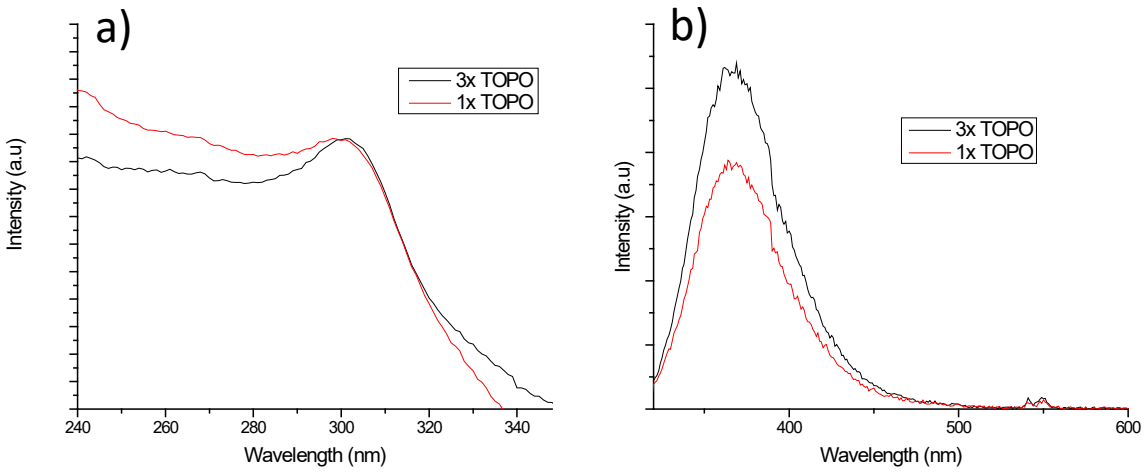

Figure 3. 25: Absorption (a) and PL emission (b) spectra of 1x and 3x TOPO treated 10Tb-CNPs in suspension.

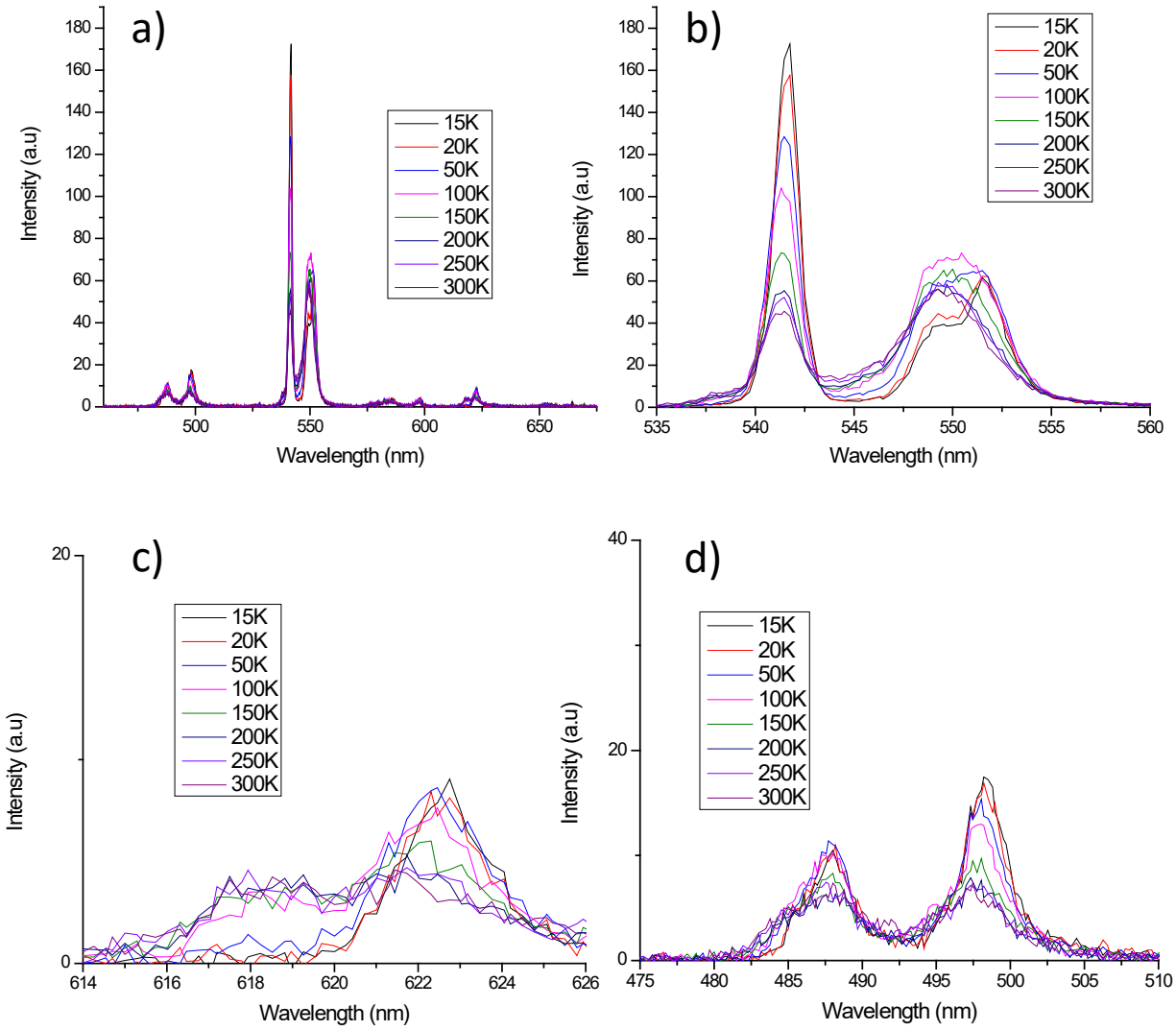

Figure 3. 26: Low temperature time-gated PL emission spectra of 3x TOPO treated 10Tb-CNPs. The total spectra (a), zoomed into $^7F_5$ transition (b), into $^7F_6$ transition (c) and into $^7F_3$ transition (d).

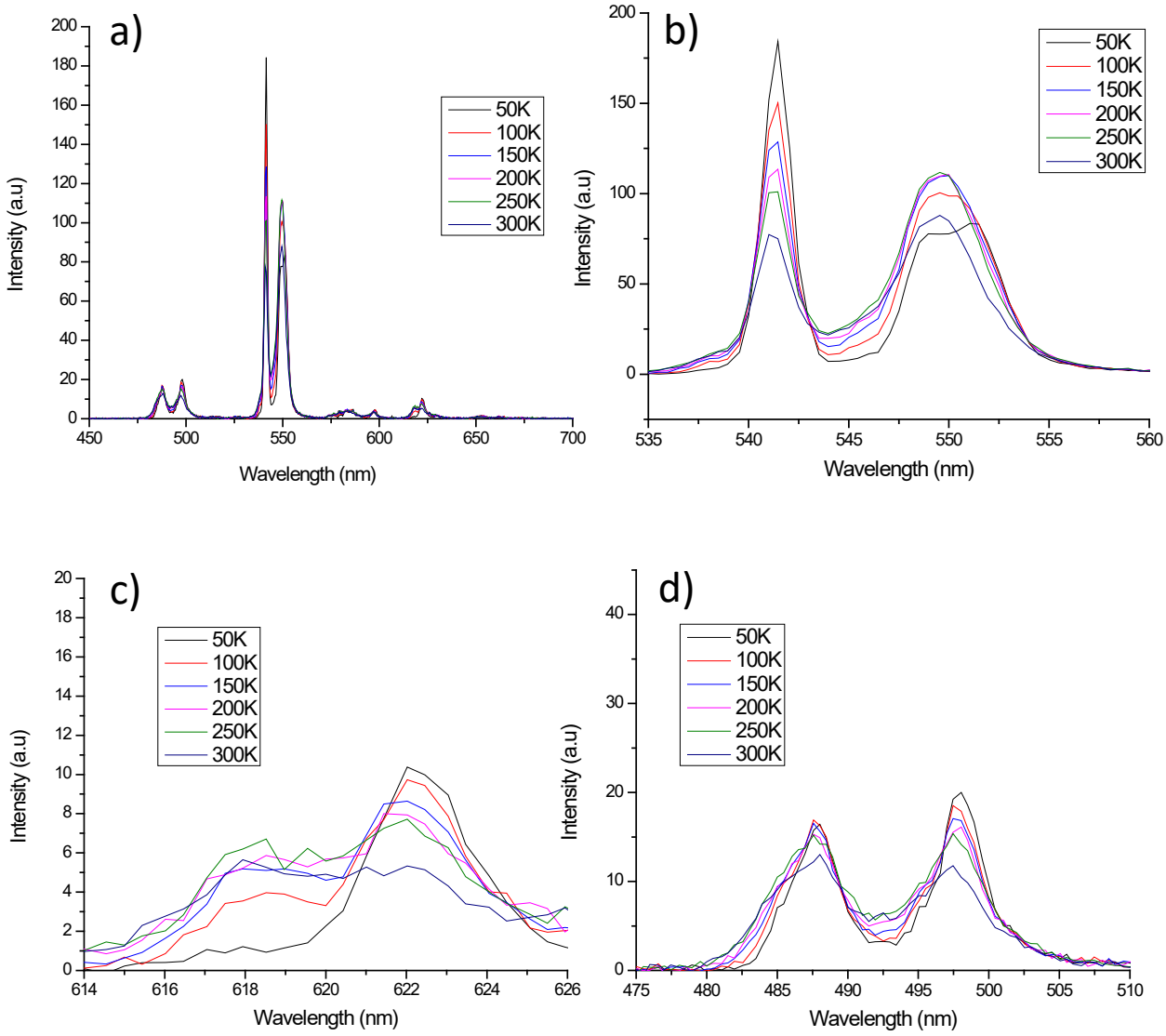

Figure 3. 27: Low temperature time-gated PL emission spectra of 1x TOPO treated 10Tb-CNPs. The total spectra (a), zoomed into $^7F_5$ transition (b), into $^7F_6$ transition (c) and into $^7F_3$ transition (d).

The low temperature time-gated PL spectra for 3x and 1x TOPO treated Tb-CNPs are shown in **Figures 3.26** and **3.27** respectively. The time-gated spectra are measured with a delay time of 0.1 ms and a gate time of 5 ms. The figures also detail several transitions of Tb^{3+} to examine their splitting to determine the symmetry of Tb^{3+} ions. From analyzing the transitions in **Figures 3.26** and **3.27** it was determined that they share similar peak splitting. For example, in **Figure 3.26 (b)** and **3.27 (b)** the $^7F_5$ transition develops a split at ~550 nm for both samples at low temperature. Again, in **Figure 3.26 (c)** and **3.27 (c)** for the $^7F_6$ transition both samples show splitting at 618 nm at high temperatures. The results indicate that the Tb^{3+} ion site symmetry is similar for both 1x and 3x TOPO treated samples.

The emission peak intensity is also related to the symmetry of its lattice sites. Tb^{3+} $^7F_6$ transitions are related to the electric-dipole mechanism while the $^7F_5$ transitions are related to the magnetic-dipole mechanism.[78] The peak height ratios of F_5:F_6 defined as the ratio between intensities from the $^7F_5$ transition and $^7F_6$ transitions give insight into the site symmetry around the Tb^{3+}.[72] A higher ratio indicates a higher symmetry, while a lower values indicate a decreased symmetry.[78] Calculating this ratio at room temperature for both 3x and 1x TOPO treated samples gives 8.454 and 7.797, respectively. The values are close to one another again indicating in both cases the symmetry of Tb^{3+} ions are very similar. The high value of the ratio indicates that Tb^{3+} is mostly in low symmetry sites, which indicates surface bound Tb^{3+}. The result is surprising for the 3x TOPO treated samples, for which lower number of surface Tb^{3+} was expected. However, the structures of the samples have not been fully elucidated yet and more insight into the Tb^{3+} symmetry sites could still be determined in future work. Overall, the results indicate that 3x TOPO treated Tb-CNPs have increase Tb^{3+} sensitization and that in both cases of 3x and 1x TOPO treated samples the symmetry of Tb^{3+} sites stay relatively similar.

3.5 Conclusion

In summary, the synthesis of TOPO treated CNPs were successfully achieved by colloidal synthesis method. The size of the particles was determined to be approximately 2-3 nm and the bulk crystal structure was determined to be CeO_2, from XRD and TEM results. The composition of the surface of these particles was determined to be mostly made of Ce^{3+} (80%) and only a small fraction of Ce^{4+} (20%). The results show a novel UV emission at 370 nm in the PL data, which was ascribed to two transitions: a Ce^{3+} intracentre transition and a MLCT between surface Ce^{3+} and surface TOPO ligands. Other ligands based on different metal-ligand bonding were also tested, such as amine and carboxylic acid ligands. Untreated samples were also tested. However, these demonstrated zero or low UV PL emission demonstrating the importance here of using oxygen phosphorus-based ligands to achieve this emission. To reveal more information about the transitions involved, low temperature PL was taken of TOPO samples. Both indicating that there are at least two transitions involved. From the low temperature PL results, the hypothesis is that the transitions at peak 355 and 385 nm are due to a MLCT and Ce^{3+} intracentre transitions as described earlier, however the exact transitions have not been fully elucidated. Further indication of the theory is demonstrated with the synthesis of Ce^{3+} TOPO complexes which also demonstrate the same band shape as the novel UV emission found in TOPO CNPs. Lasty, PLQY studies were done on varying TOPO samples. TOPO treated samples demonstrated a high PLQY of 12-20%. Different TOPO treated samples synthesized at different temperatures. From **Figure 3.7** there is an increase in PLQY till 220ºC and then a sharp drop off afterwards. The PLQY of the TOPO treated CNPs are relatively high when compared to literature and demonstrate their efficiency and stability.[73] Proper nano-engineering of CNPs via synthesis control, surface treatment and defect control have led to novel discoveries in cerium oxide PL. The approach taken in this work can be

developed to other systems as understanding the nature and role of surface ligands in PL mechanics and quantum yield is pivotal for the design of enhanced UV photonics.

The introduction of lanthanides into CNPs has proven to demonstrate valuable tunability for the rational design of white light emitting phosphors. As the results indicate a white light emission from UV excited Er-CNPs and GdEr-CNPs were achieved. Lanthanides, particularly Tb^{3+} was shown to be able to be sensitized by TOPO CNPs MLCT. 3x TOPO treated Tb-CNPs also demonstrated better sensitization due to higher probability of MLCT sensitizing Tb^{3+} either on the surface or in the lattice. The successful sensitization of Tb^{3+} here leads to further exploration of lanthanide sensitization through novel methods and can improve future technologies. Overall, the results of the lanthanide incorporated cerium oxides have demonstrated the potential for tunable and multifunctional conducting cerium oxides for photonic applications.

Chapter 4.0 Gallium Oxide Results and Discussion

4.1 Structural Characterization of AGO

4.12 XRD

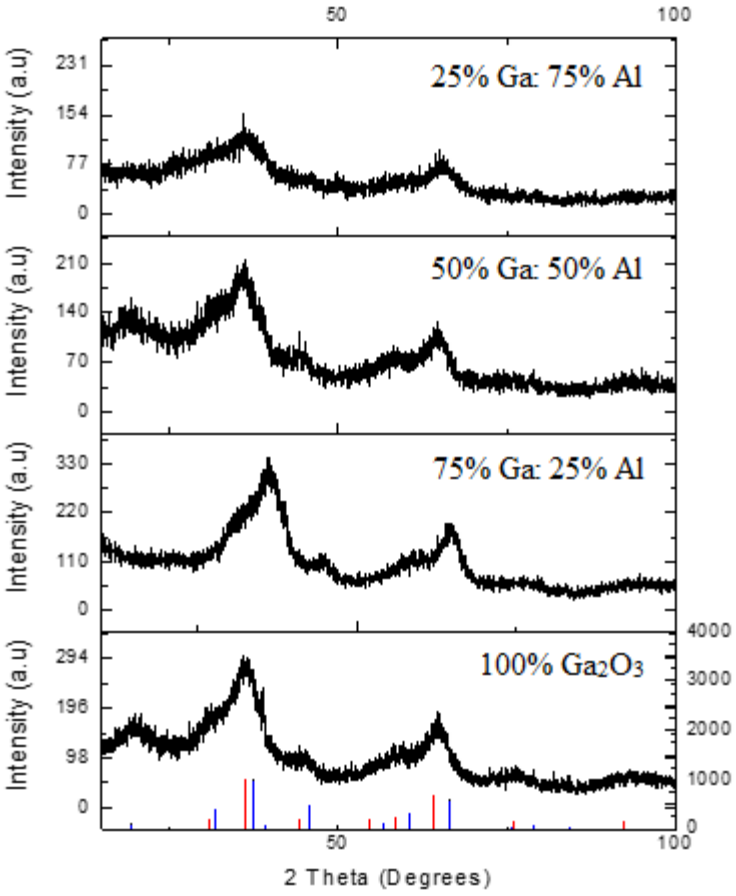

Figure 4. 1: XRD of AGO NPs at varying Al and Ga contents. Red lines represent γ-Ga_2O_3 and blue lines γ-Al_2O_3 crystal structure.

In **Figure 4.1** the XRD pattern of ST synthesized AGO TOPO treated NPs are shown with increasing Al concentration. The red lines represent γ-Ga_2O_3, and the blue represent γ-Al_2O_3 structural patterns, which both have a defect spinel structure. It is difficult to discern the γ-Ga_2O_3 and γ-Al_2O_3 peaks due to their similar lattice structure however, the peaks are in line with the defect spinel structure pointing towards the γ-polymorph for the NPs. As more Al is added the peaks become broader indicating that the NPs are becoming amorphous. From the peaks and using the Debye-Scherrer equation the average grain size of the NPs was determined to be approximately 2 nm. There is also a small shift in peaks to lower angles as Al content is increased, this indicates a change in lattice parameters most likely due to incorporation of Al_2O_3 γ-polymorph phase. In conclusion from the XRD the formation of small ~2 nm sized amorphous heterostructure NPs of AGO can be determined.

4.13 TEM

TEM images of ST synthesized 50:50 (%Ga:%Al) AGO TOPO treated NPs are shown here. The particles agglomerated however, there are a few that were able to be analyzed through multiple images. The average size was determined to be approximately 2.5 nm which aligns well with XRD data.

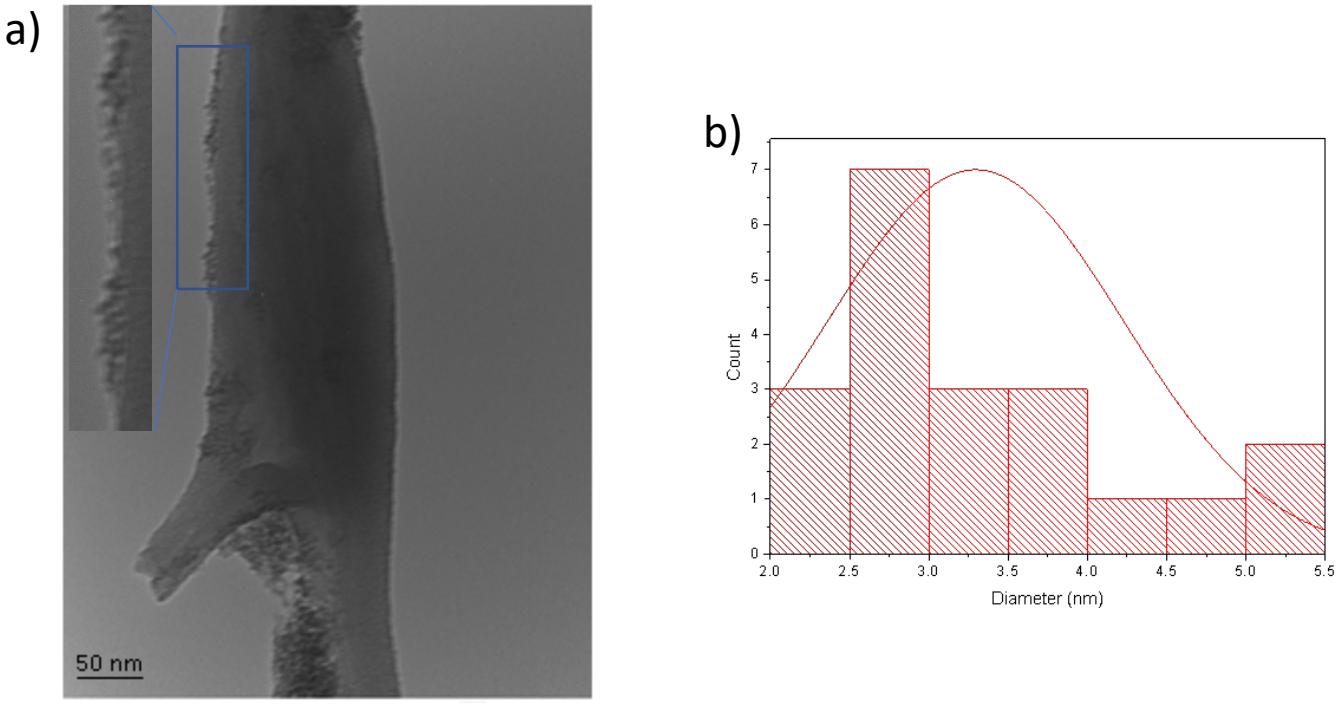

Figure 4. 2: Gallium oxide TEM images (inset is of the furthered zoomed in area) (a) and histogram with distribution curve (b).

4.14 XPS

The XPS shown here demonstrates the amount of Al vs Ga on the surface. The XPS spectra were deconvoluted using the CasaXPS software and baseline corrected using a U4 Tougaard method. The results indicate the presences of both Ga and Al from XPS fitting. From deconvoluting and calculating integrated areas the amount of Ga to Al was determined to be 9:1 (Ga:Al). This method of structural analysis is mostly helpful for the surface however it

demonstrated that there is a mix Ga, Al, and O phase on the surface of the particle, indicating some sort of heterostructure alloy.

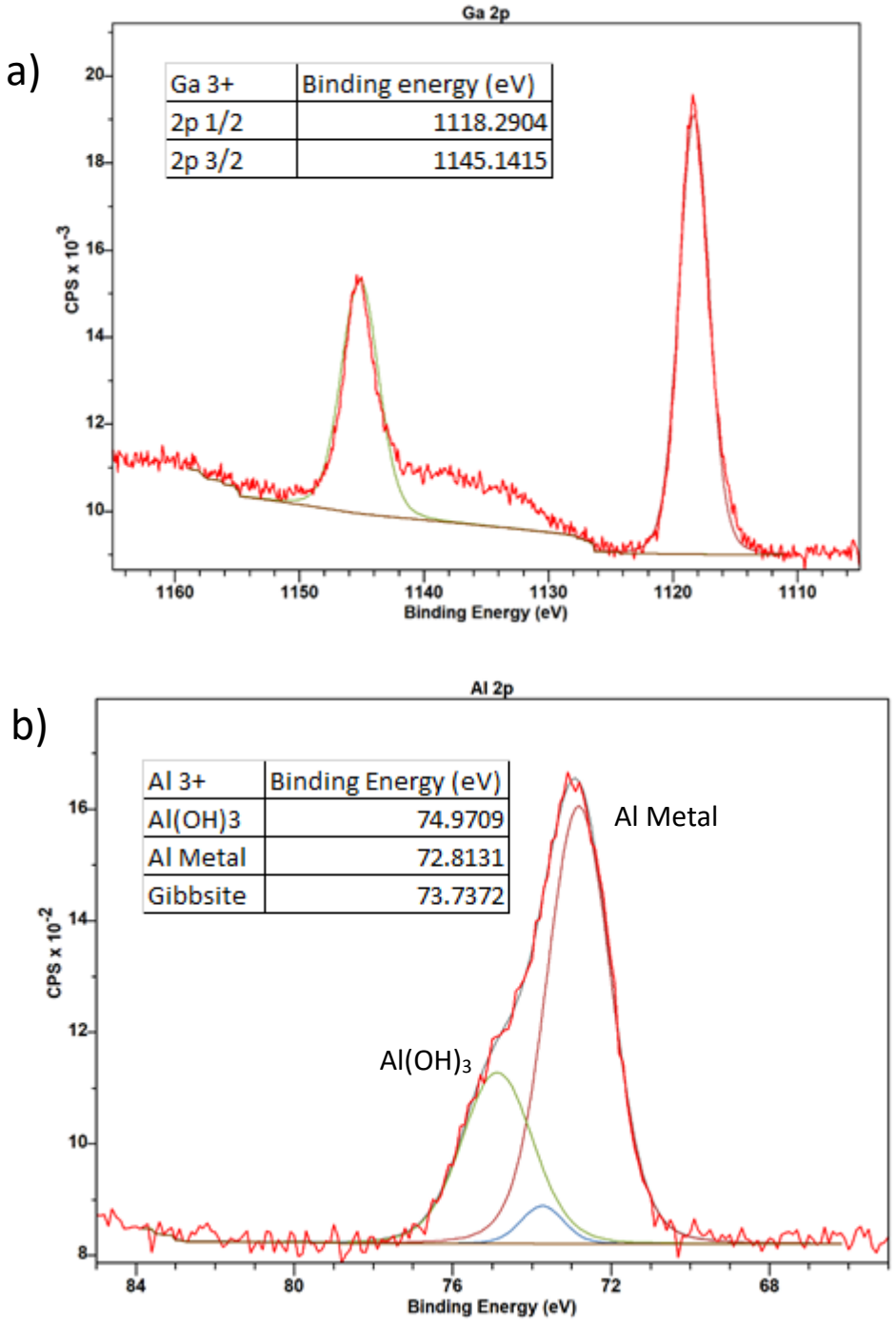

Figure 4. 3: XPS of TOPO treated AGO NPs. Ga 2p (a) and Al 2p (b) XPS spectra.

4.2 Effect of Temperature on Gallium Oxide Synthesis

Pure Ga_2O_3 NPs were synthesized via the colloidal method at varying temperatures of 160ºC, 180ºC and 200ºC to determine the effect of reaction temperature on PL and absorption. Each reaction was done for approximately 1 hour keeping reaction time constant. The fitted PL and absorption spectra are shown in **Figure 4.4** and **4.5**, where the noise and background were subtracted. Similar fitting methods were used throughout PL spectra analysis herein. Hexane was used as a baseline for UV-Vis-NIR measurements. **Table 4.1** shows the emission wavelength at the maximum intensity, where 200ºC gives 422 nm emission and 180ºC shows a blue shift to 410 nm. At 160ºC there is a smaller blue shift to 417 nm and the intensity was low due to the lack of thermal energy needed to form a crystal structure.[4]

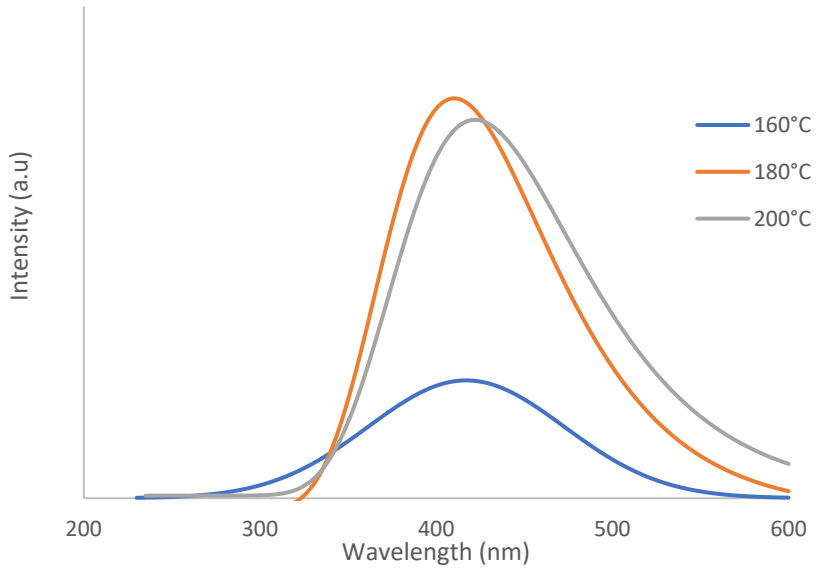

Figure 4. 4: Effect of temperature on PL of colloidal synthesized gallium oxide NPs PL (fitted spectra).

Temperature (ºC)	160	180	200
Emission (nm)	417	410	422

Table 4. 1: Temperature of synthesis and respective maximum emission peak.

The resulting absorption and TAUC plots show that there is no discernible difference in band gap between the varying temperatures however the PL spectrums shows that temperature does influence the emission wavelength. It is possible that a lower temperature synthesis causes a larger concentration of defects, decreasing average donor-acceptor separation.

In conclusion it was determined that a minimum of >160ºC is needed to form NPs with good PL emission. The particles synthesized at 180ºC and 200ºC show very similar emission, however particles synthesized at 180ºC show a deeper UV shift at 410nm. For colloidal synthesis optical analysis both temperatures of 180ºC and 200ºC were tested when synthesizing AGO NPs.

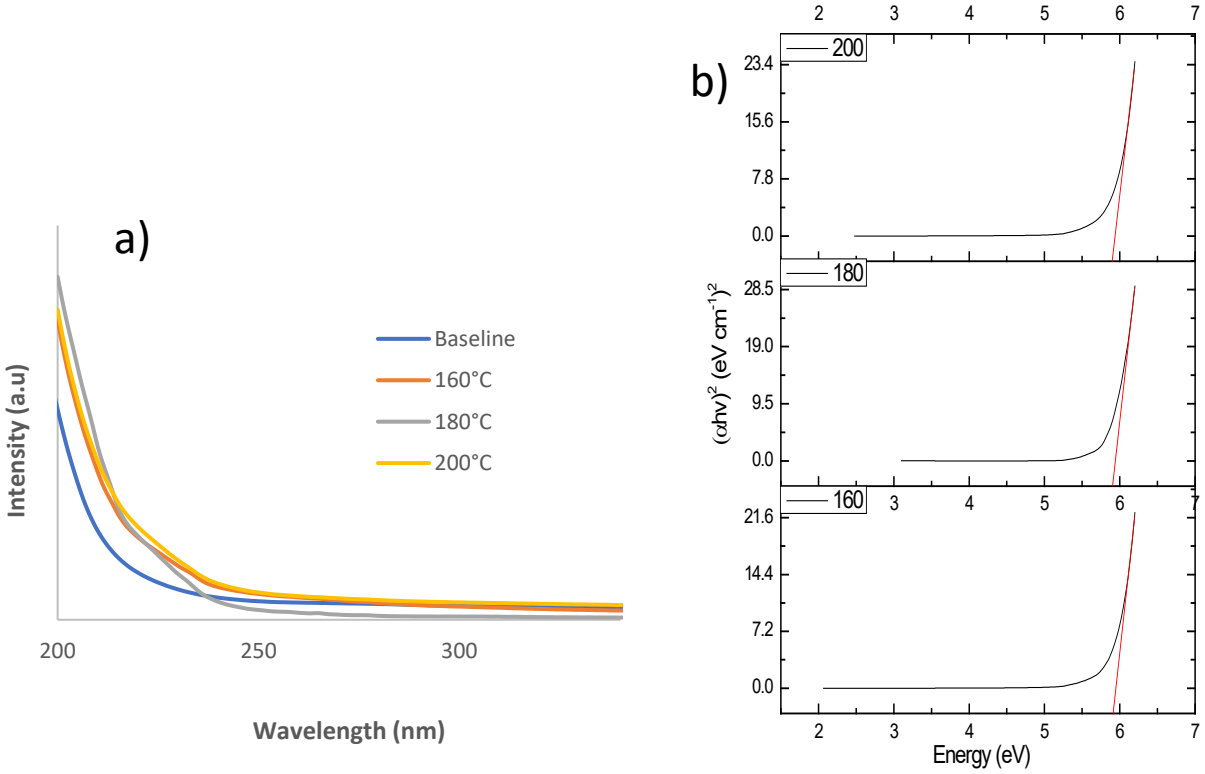

Figure 4. 5: Absorption (baseline = hexane) of gallium oxide synthesized at varying temperatures (a) and their TAUC plots (b).

4.3 Effect of Aluminum on Gallium Oxide Optical Properties

4.31 Colloidal Synthesized AGO NPs

Colloidal AGO NPs with varying precursor molar ratios of 75:25 and 50:50 (%Ga:%Al) were synthesized at 180ºC and 200ºC. The PL, absorption and TAUC plots are depicted in **Figure 4.6** and **4.7**. **Table 4.2** shows the emission wavelength from the PL spectra.

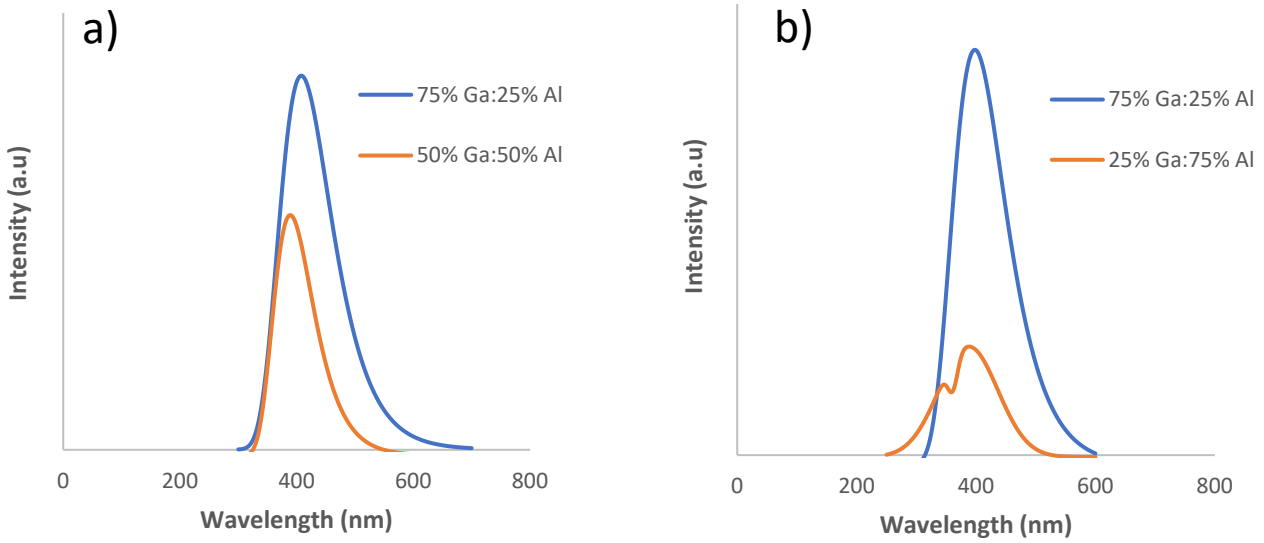

Figure 4. 6: Fitted PL emission spectra of colloidal synthesized Gallium Oxide NPs @ 180ºC (a) and 200ºC (b) and at varying. Al contents

Temperature (ºC)	180	180	200	200
Composition (%Ga:%Al)	75:25	50:50	75:25	25:75
Emission (nm)	408	389	398	387,361

Table 4. 2: Temperature, composition, and respective maximum emission peak of varying Ga:Al alloys

The data shows a decrease in intensity as more Al is added. For 200ºC synthesis temperature and ratio of 25:75 there are two peaks which could indicate the formation of Al_2O_3 phase together with AGO NPs. For all scenarios there is a shift to the UV region with increasing

concentration of Al. The result at 180ºC and a ratio of 50:50 shows relatively high intensity with a discernable UV-shift. absorption and TAUC plots show that there is a slight increase in band gap energy as concentration of aluminum is increased.

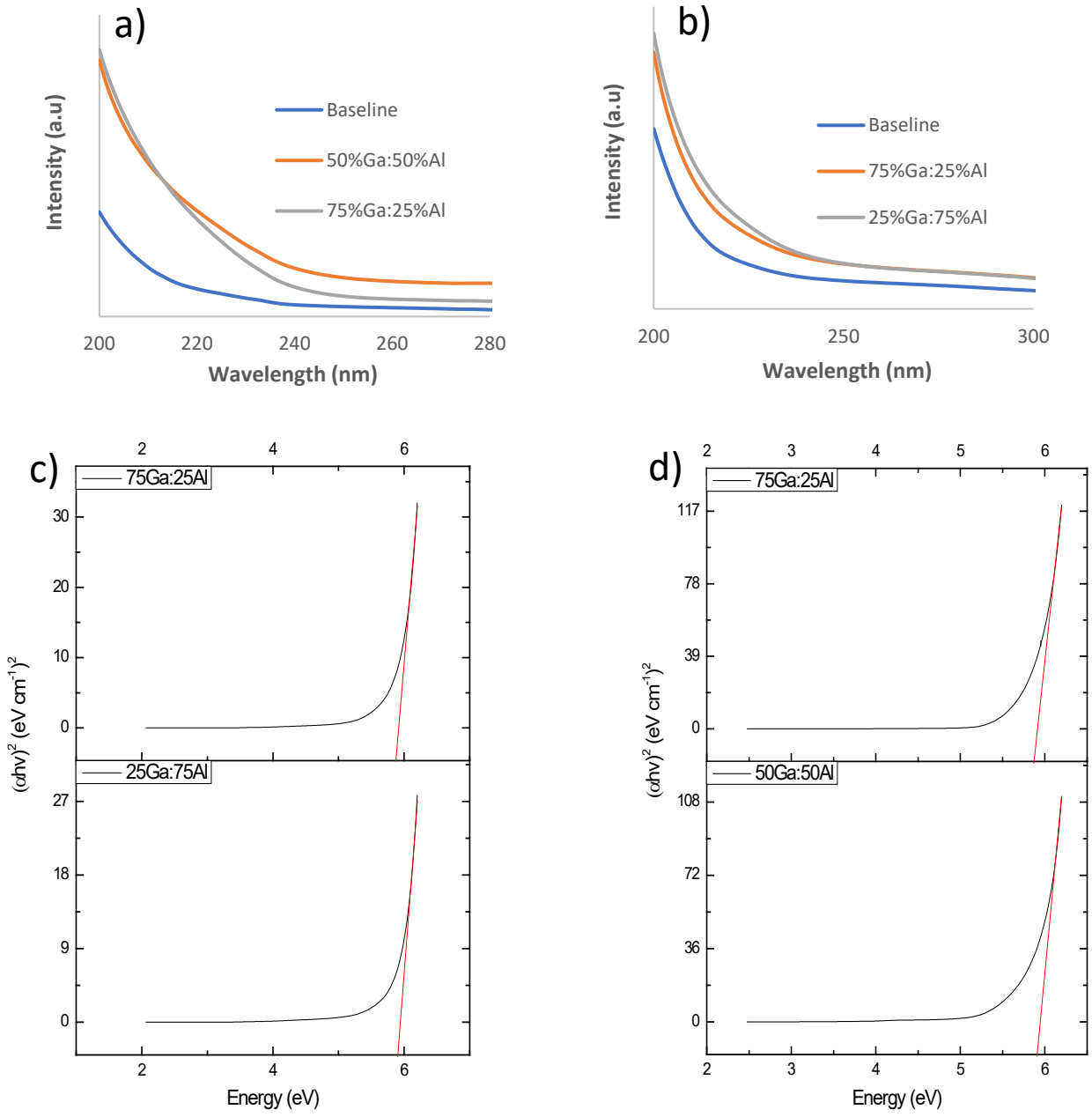

Figure 4. 7: Absorption spectra of colloidal synthesized Gallium Oxide NPs at 180ºC (a) and 200ºC (b) (baseline = hexane) and at varying Al contents and their TAUC plots at 180ºC (c) and 200ºC (d).

4.32 ST Synthesized AGO NPs

Here the ST synthesized AGO particles were evaluated at varying Ga:Al ratios and at 180ºC and 200ºC. The PL, absorption and TAUC plots for ST synthesized AGO NPs are shown in the figures bellow. The PL spectrum at 180ºC and 200ºC both demonstrate a shift to the UV region as aluminum dopant concentration increases. However, like the colloidal synthesis the intensity of the PL decreases as Al concentration increases, with a noticeable drop of in intensity after 75% Al. It was calculated through PLQY studies that the highest PLQY attained from samples were 3%. At 200ºC and a ratio of 50:50 there is a good UV shift to QY lost ratio where there is a shift to 376 nm from 414 nm of pure gallium. The next best result is at 180ºC and a ratio of 50:50 which shows a shift to 380 nm from 410 nm. From both synthesis methods a ratio of 50:50 is the optimal feed ratio to get a relatively high PL intensity with a great shift into the UV region. From the absorption and TAUC plots there is a discernable increase in band gap 5.8eV to 6.1eV and emission peak from 414 nm to 367 nm, with increasing concentration of Al.

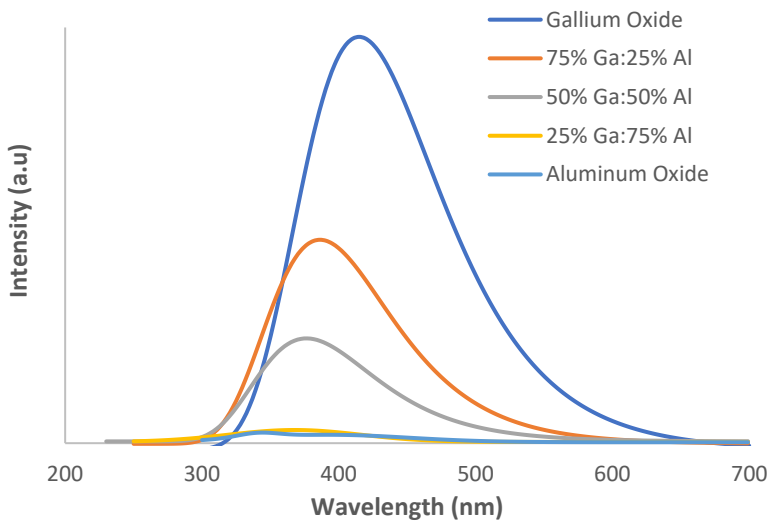

Figure 4. 8: Fitted PL emission spectra of 200ºC ST synthesized Gallium Oxide NPs at varying Al contents.

Composition (Ga%:Al%)	100% Ga	75:25	50:50	25:75	100% Al
Emission(nm)	414	386	376	367	340,393

Table 4. 3: Composition of 200ºC ST synthesized Ga_2O_3 NPs and their respective emission peak maximums.

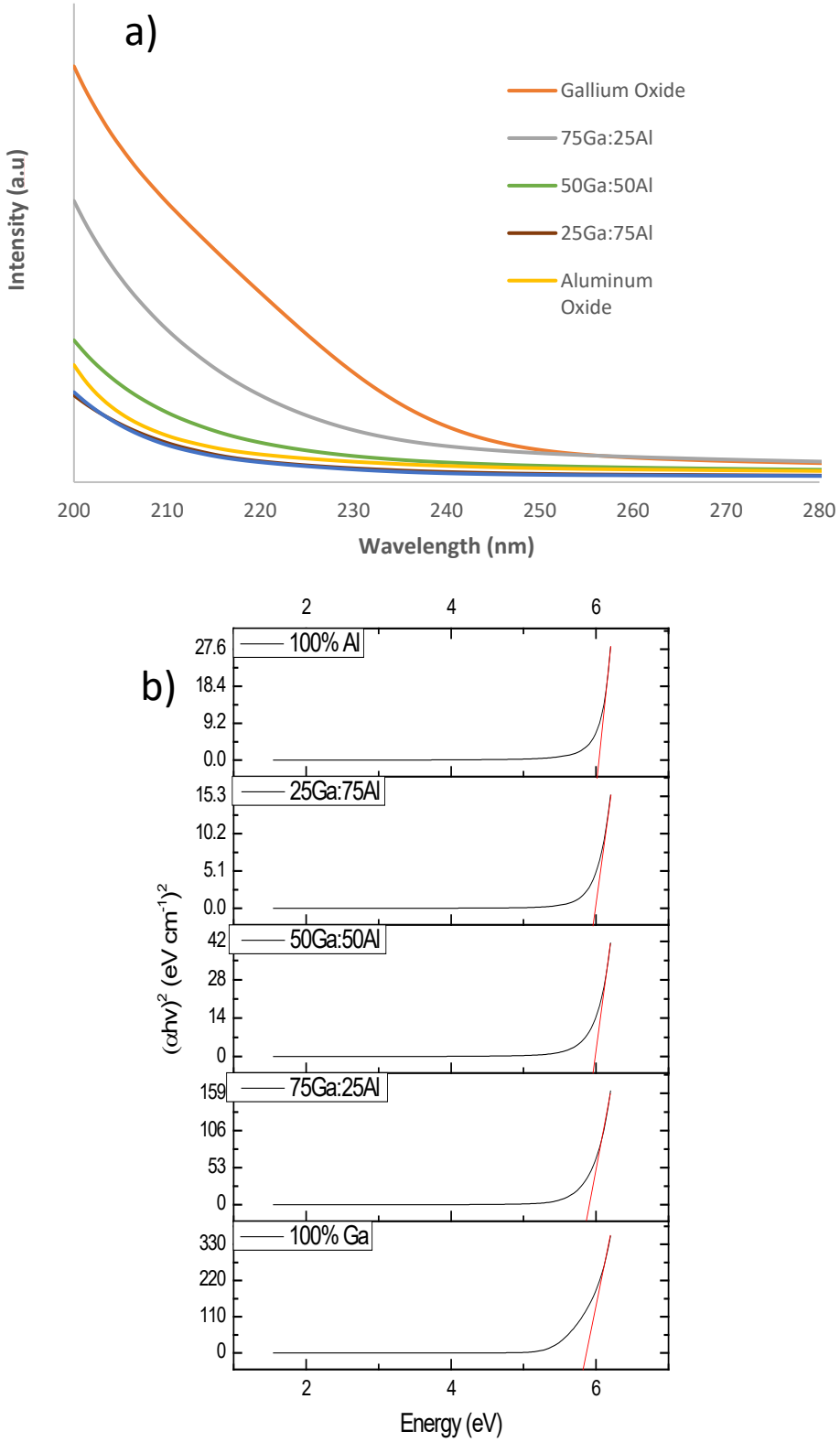

Figure 4. 9: Absorption spectra of 200 °C ST synthesized Gallium Oxide NPs at varying Al contents (a) (baseline = hexane) and their TAUC plots (b).

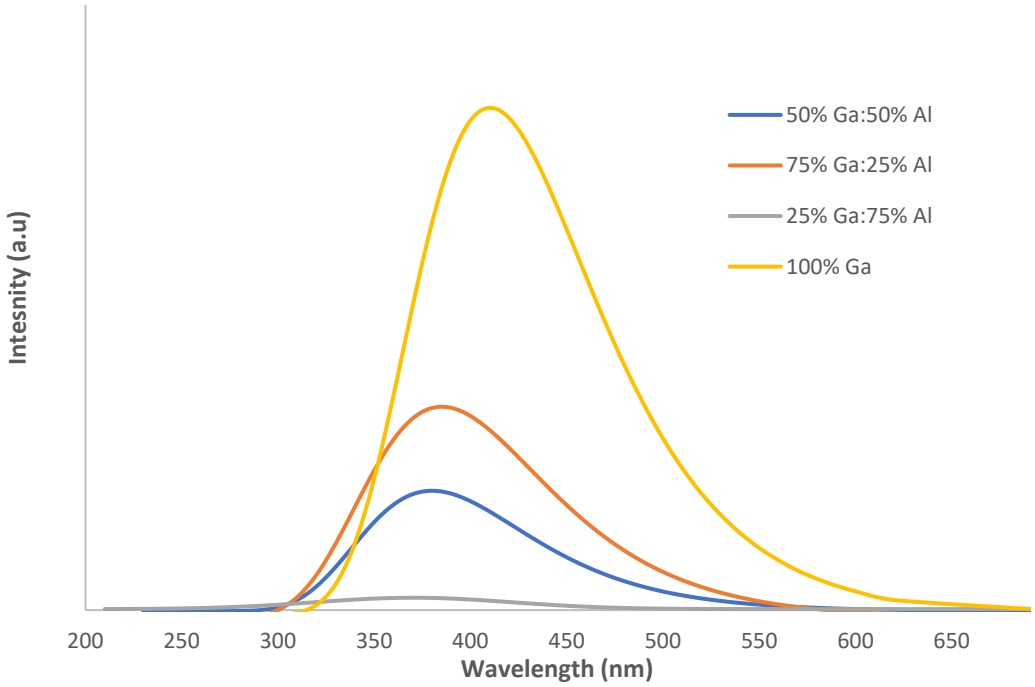

Figure 4. 10: Fitted PL emission spectra of 180°C ST synthesized Gallium Oxide NPs at varying Al contents.

Composition (Ga%:Al%)	100% Ga	75:25	50:50	25:75
Emission (nm)	410	385	380	370

Table 4. 4: Composition of 180°C ST synthesized Ga_2O_3 NPs and their respective emission peak maxima.

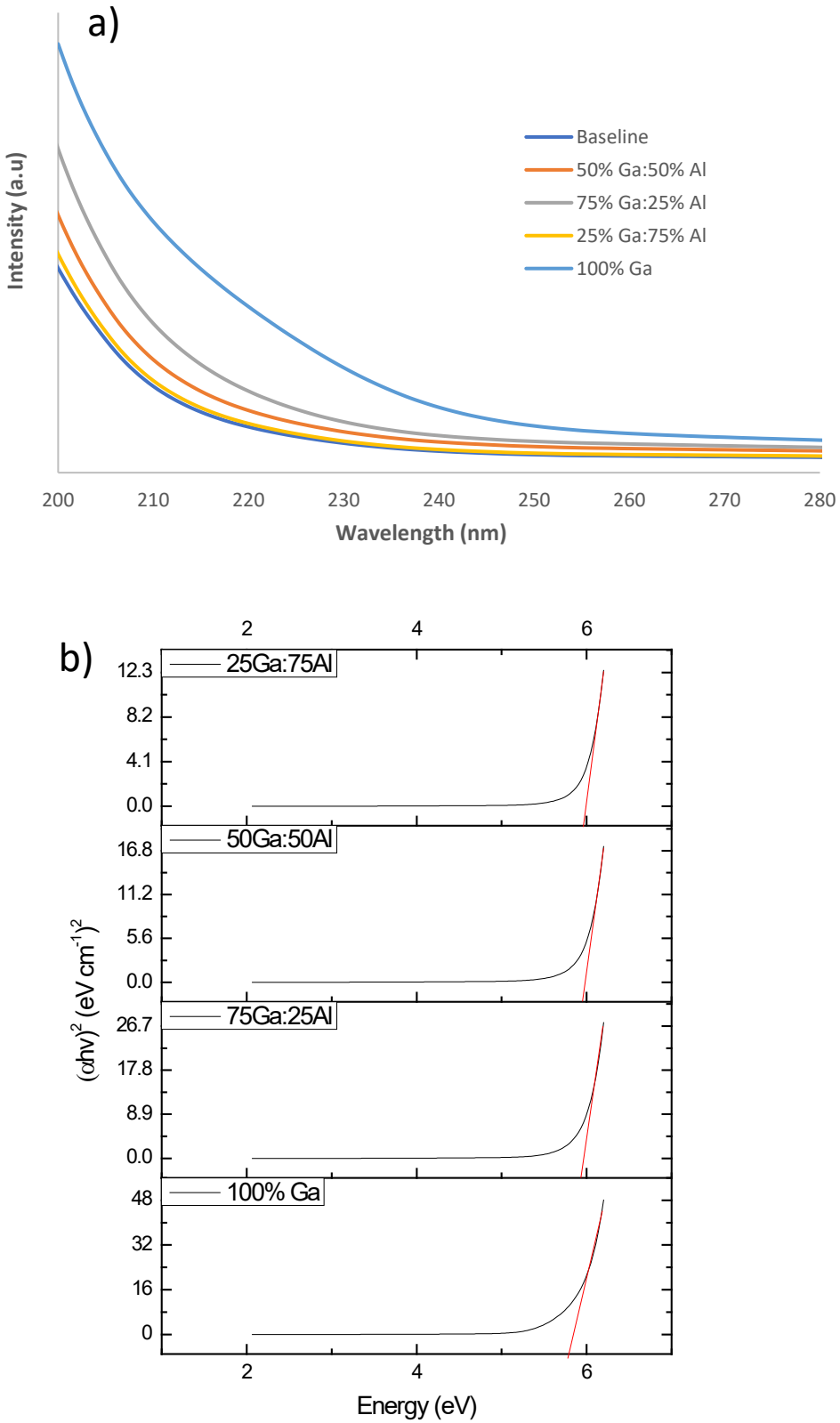

Figure 4. 11: Absorption spectra of 180°C ST synthesized Gallium Oxide NPs at varying Al contents (a) (baseline = hexane) and their TAUC plots (b).

4.4 Conclusion

Gallium oxide and AGO NPs were successfully synthesized both via the colloidal and solvothermal method at different temperatures and Al concentration. Optical properties for both the colloidal and solvothermal synthesized NPs were examined. A change in band gap of these particles was determined through TAUC plot calculations. From the results the PL emission is shifted to the UV region and the band gap is increased as aluminum concentration is increased. The emission of γ-Ga_2O_3 NPs arises from recombination of an electron trapped in a shallow defect-originated electron donor state with a hole trapped in an electron acceptor state. This DAP emission band is strongly broadened due to the large surface area and a range of separations between participating defect sites, defect sites most likely introduced by alloying with γ-Al_2O_3. Several varying amounts of Al were used for incorporation into gallium oxide. In particular, the result with the best trade-off of intensity to UV shift was from the solvothermal synthesized NPs at 200^oC and at a dopant ratio of 50:50 (%Ga:%Al), giving an emission at 376 nm and QY of 3%. XRD and TEM data was obtained for the solvothermal synthesized AGO NPs, indicating a defect spinel structure and an average NP size of ~2.5 nm.

In conclusion the results demonstrate a capable method of synthesizing tunable UV emitting AGO NPs and displayed their possibility for applicative use in light displays, UV photodetectors, UV lamps and general photonics. The results also demonstrate the effect of alloying and reaction parameters on controlling the band gap and photoelectric properties of γ-Ga_2O_3 NPs. The techniques here can be further explored to enhance the functionality of other TCO systems.

5.0 General Remarks and Future Outlook

Overall, the results here demonstrate the rational design of NPs for the purpose of reducing waste and improving photonic applications. TOPO CNPs were successfully synthesized that produced a novel UV emission. The mechanism of the TOPO CNPs emission is currently being investigated with the results indicating that it originates from a Ce^{3+} 5d-4f transitions and a CT from Ce^{3+} TOPO complexes. TOPO Tb-CNPs were synthesized resulting in green emitting NPs from sensitized Tb^{3+} ions. The Tb^{3+} ions were sensitized by the novel UV emission found in TOPO CNPs. Tb^{3+} sensitization was also shown to be affected by the number of TOPO treatments. To further explore lanthanide sensitization in TOPO CNPs a few experiments can be done such as synthesizing samples with varying Tb^{3+} dopant concentrations and then analyze the samples to determine the effect of Tb^{3+} concentration on sensitization. Analysis on the PL decay dynamics of such samples can also shed light on the energy transfer process during sensitization. AGO NPs were successfully synthesized and demonstrated PL shift into the UV region. However, their PLQY was very low and presents a problem for future prospects. The AGO NPs demonstrated the use of alloying and rational design in control over conducting oxide functionality in photonics. The work here indicates that research into CNPs for use in photonics is very promising and can lead to new avenues for rational design of NPs.

References

(1) Martienssen, W. Semiconductors. In Springer Handbook of Condensed Matter and Materials Data, 2nd ed.; *Springer Berlin Heidelberg*: Berlin, Heidelberg, **2005**, *2*, 575–694. https://doi.org/10.1007/3-540-30437-1_9.

(2) Neamen, D. A. Semiconductor Physics and Devices Basic Principles, 4th ed.; *McGraw-Hill*: New York, NY, **2006**, *9*, 1-21. https://doi.org/10.1016/S1369-7021(06)71498-5.

(3) Erwin, S. C.; Zu, L.; Haftel, M. I.; Efros, A. L.; Kennedy, T. A.; Norris, D. J. Doping Semiconductor Nanocrystals. *Nature.* **2005**, *436*, 91-94. https://doi.org/10.1038/nature03832.

(4) Lounis, S. D.; Runnerstrom, E. L.; Llordés, A.; Milliron, D. J. Defect Chemistry and Plasmon Physics of Colloidal Metal Oxide Nanocrystals. *J. Phys. Chem. Lett*. **2014**, *9*, 1564-1574 https://doi.org/10.1021/jz500440e.

(5) You, H.; Yang, S.; Ding, B.; Yang, H. Synthesis of Colloidal Metal and Metal Alloy Nanoparticles for Electrochemical Energy Applications. *Chem. Soc. Rev.* **2013**, *42*, 2880-2904. https://doi.org/10.1039/c2cs35319a.

(6) Ginley, D. S.; Bright, C. Transparent Conducting Oxides. *MRS Bull.* **2000**, *25*, 15-18. https://doi.org/10.1557/mrs2000.256.

(7) Norris, D. J.; Efros, A. L.; Erwin, S. C. Doped Nanocrystals. *Science*. **2008**, *319*, 1776-1779. https://doi.org/10.1126/science.1143802.

(8) Paine, B. G. lewis and D. C. Applications and Processing of Transparent Conducting Oxides Large-Scale Manufacturing of ITO Thin-Film Coatings. *MRS Bull.* **2011**, *25*, 22-27. https://doi.org/10.1016/S0040-6090(02)00163-3.

(9) Wang, T.; Layek, A.; Hosein, I. D.; Chirmanov, V.; Radovanovic, P. V. Correlation between Native Defects and Dopants in Colloidal Lanthanide-Doped Ga_2O_3 Nanocrystals: A Path to Enhance Functionality and Control Optical Properties. *J. Mater. Chem. C.* **2014**, *2*, 3212-3222. https://doi.org/10.1039/c3tc31823k.

(10) Wang, T.; Farvid, S. S.; Abulikemu, M.; Radovanovic, P. V. Size-Tunable Phosphorescence in Colloidal Metastable γ-Ga_2O_3 Nanocrystals. *J. Am. Chem. Soc.* **2010**, *132*, 9250-9252. https://doi.org/10.1021/ja101333h.

(11) Farvid, S. S.; Dave, N.; Wang, T.; Radovanovic, P. V. Dopant-Induced Manipulation of the Growth and Structural Metastability of Colloidal Indium Oxide Nanocrystals. *J. Phys. Chem. C.* **2009**, *36*, 15928-15933 https://doi.org/10.1021/jp905281k.

(12) Jin, S.; Lu, W.; Stanish, P. C.; Radovanovic, P. V. Compositional Control of the Photocatalytic Activity of Ga_2O_3 Nanocrystals Enabled by Defect-Induced Carrier Trapping. *J.Phys. Chem. Lett.* **2018**, *706*, 509–514. https://doi.org/10.1016/j.cplett.2018.06.046.

(13) Wang, T.; Chirmanov, V.; Chiu, W. H. M.; Radovanovic, P. V. Generating Tunable White Light by Resonance Energy Transfer in Transparent Dye-Conjugated Metal Oxide Nanocrystals. *J. Am. Chem. Soc.* **2013**, *39*, 14520-14523. https://doi.org/10.1021/ja407013z.

(14) Aoki, T. Photoluminescence Spectroscopy. *Mater. Charact.* **2012**, *3*, 212-226. https://doi.org/10.1002/0471266965.com058.pub2.

(15) McKittrick, J.; Shea-Rohwer, L. E. Review: Down Conversion Materials for Solid-State Lighting. *J. Am. Ceramic Soc*. **2014**, *97*, 1327-1352. https://doi.org/10.1111/jace.12943.

(16) Meyer, B. K.; Alves, H.; Hofmann, D. M.; Kriegseis, W.; Forster, D.; Bertram, F.; Christen, J.; Hoffmann, A.; Straßburg, M.; Dworzak, M.; Haboeck, U.; Rodina, A. V. Bound Exciton and Donor-Acceptor Pair Recombinations in ZnO. *Phys. Status Solidi Basic Res.* **2004**, *241*, 231-260 https://doi.org/10.1002/pssb.200301962.

(17) Esteve-Paredes, J. J.; Pakdel, S.; Palacios, J. J. Quenching of Exciton Recombination in Strained Two-Dimensional Monochalcogenides. *Phys. Rev. Lett.* **2019**, *123*, 91-97. https://doi.org/10.1103/PhysRevLett.123.077402.

(18) Wang, T.; Radovanovic, P. V. Size-Dependent Electron Transfer and Trapping in Strongly Luminescent Colloidal Gallium Oxide Nanocrystals. *J. Phys. Chem. C.* **2011**, *121*, 9433-9441. https://doi.org/10.1021/jp205502d.

(19) Kang, T. W.; Park, S. H.; Song, H.; Kim, T. W.; Yoon, G. S.; Kim, C. O. Mechanism of Donor-Acceptor Pair Recombination in Mg-Doped GaN Epilayers Grown on Sapphire Substrates. *J. Appl. Phys.* **1998**, 84, 1998-2082. https://doi.org/10.1063/1.368269.

(20) Binet, L.; Gourier, D. Origin of the Blue Luminescence of β-Ga_2O_3. *J. Phys. Chem. Solids.* **1998**, *59*, 1241-1249. https://doi.org/10.1016/S0022-3697(98)00047-X.

(21) Farvid, S. S.; Wang, T.; Radovanovic, P. V. Colloidal Gallium Indium Oxide Nanocrystals: A Multifunctional Light-Emitting Phosphor Broadly Tunable by Alloy Composition. *J. Am. Chem. Soc.* **2011**, *133*, 6711-6719. https://doi.org/10.1021/ja111514u.

(22) Vanithakumari, S. C.; Nanda, K. K. Synthesis of One-Dimensional N-Doped Ga_2O_3 Nanostructures: Different Morphologies and Different Mechanisms. *Bull. Mater. Sci.* **2011**, *34*, 1331-1338. https://doi.org/10.1007/s12034-011-0324-9.

(23) Lu, W. Manipulation of Defect Formation in Semiconductor Nanocrystals for Photocatalysis and Magneto-Optics. Thesis University of Waterloo: Waterloo, Ontario, Canada, **2020**.

(24) Chirmanov, V.; Stanish, P. C.; Layek, A.; Radovanovic, P. V. Distance-Dependent Energy Transfer between Ga_2O_3 Nanocrystal Defect States and Conjugated Organic Fluorophores in Hybrid White-Light-Emitting Nanophosphors. *J. Phys. Chem. C.* **2015**, *119*, 5687-5696. https://doi.org/10.1021/jp512417h.

(25) Ghodsi, V. Modulating Optical and Photocatalytic Properties of Transparent Metal Oxide Nanostructures via Defect Engineering. Thesis University of Waterloo: Waterloo, Ontario, Canada, **2018**.

(26) Wang, T.; Radovanovic, P. V. In Situ Enhancement of the Blue Photoluminescence of Colloidal Ga_2O_3 Nanocrystals by Promotion of Defect Formation in Reducing Conditions. *Chem. Commun.* **2011**, *47*, 7161-7163. https://doi.org/10.1039/c1cc11957e.

(27) Harris, J. S.; Yuen, H.; Bank, S.; Wistey, M.; Lordi, V.; Gugov, T.; Bae, H.; Goddard, L. Dilute Nitride Semiconductors, 1st ed.; *Elsevier Science:* Amsterdam, NL, **2005**, *1*, 91-92. https://doi.org/10.1016/b978-008044502-1/50001-9.

(28) Kuang, W. J.; Li, Q.; Sun, Y.; Chen, J.; Tolner, H. Near-Band-Edge Emission Characteristics of ZnO-MgO Core-Shell Quantum-Dots. *Mater. Lett.* **2016**, *178*, 27–30. https://doi.org/10.1016/j.matlet.2016.04.164.

(29) Stepanov, S. I.; Nikolaev, V. I.; Bougrov, V. E.; Romanov, A. E. Gallium Oxide: Properties and Applications - A Review. *Rev. Adv. Mater. Sci.* **2016**, *44*, 63–86.

(30) Jin, S. Manipulation of Electronic Band Structure by Doping Colloidal Gallium Oxide Nanocrystals and Its Impact on Photocatalysis. Thesis University of Waterloo: Waterloo, Ontario, Canada, **2018.**

(31) Playford, H. Y.; Hannon, A. C.; Tucker, M. G.; Dawson, D. M.; Ashbrook, S. E.; Kastiban, R. J.; Sloan, J.; Walton, R. I. Characterization of Structural Disorder in γ-Ga_2O_3. *J. Phys. Chem. C.* **2014**, *118*, 16188-16198. https://doi.org/10.1021/jp5033806.

(32) Harwig, T.; Kellendonk, F. Some Observations on the Photoluminescence of Doped β-Galliumsesquioxide. *J. Solid State Chem.* **1978**, *24*, 3-4. https://doi.org/10.1016/0022-4596(78)90017-8.

(33) Ghodsi, V.; Lu, W.; Radovanovic, P. V. Synergistic Effect of the Electronic Structure and Defect Formation Enhances Photocatalytic Efficiency of Gallium Tin Oxide Nanocrystals. *J. Phys. Chem. C.* **2019**, *123*, 433-442. https://doi.org/10.1021/acs.jpcc.8b08613.

(34) Younis, A.; Chu, D.; Li, S. Functionalized Nanomaterials, 1st ed.; *Intech open*: London, UK, **2016**, *3*, 202-208. https://doi.org/10.5772/65937.

(35) Jayakumar, G.; Albert Irudayaraj, A.; Dhayal Raj, A. A Comprehensive Investigation on the Properties of Nanostructured Cerium Oxide. *Opt. Quantum Electron.* **2019**, *51*, 1-15. https://doi.org/10.1007/s11082-019-2029-z.

(36) Singh, S.; Lo, S. L. Single-Phase Cerium Oxide Nanospheres: An Efficient Photocatalyst for the Abatement of Rhodamine B Dye. *Environ. Sci. Pollut. Res.* **2018**, *25*, 6532–6544. https://doi.org/10.1007/s11356-017-0902-5.

(37) Seal, S.; Jeyaranjan, A.; Neal, C. J.; Kumar, U.; Sakthivel, T. S.; Sayle, D. C. Engineered Defects in Cerium Oxides: Tuning Chemical Reactivity for Biomedical, Environmental, & Energy Applications. *Nanoscale.* **2020**, *12*, 6879–6899. https://doi.org/10.1039/d0nr01203c.

(38) Kumar, A.; Babu, S.; Karakoti, A. S.; Schulte, A.; Seal, S. Luminescence Properties of Europium-Doped Cerium Oxide Nanoparticles: Role of Vacancy and Oxidation States. *Langmuir.* **2009**, *25*, 10998–11007. https://doi.org/10.1021/la901298q.

(39) Hokura, A.;Oxidation and Reduction of Cerium during Solvent Extraction with Benzoyltrifluoracetone into Nonpolar Organic Solvent in the Absence and Presence of Trioctylphosphine Oxide. *Chem. Soc. Jap.* **1996**, *1*, 81-86.

(40) Chahal, S.; Kumar, A.; Kumar, P. Erbium-Doped Oxygen Deficient Cerium Oxide: Bi-Functional Material in the Field of Spintronics and Photocatalysis. *Appl. Nanosci.* **2020**, *10*, 1721-1733. https://doi.org/10.1007/s13204-020-01253-w.

(41) Bazhukova, I. N.; Sokovnin, S. Y.; Ilves, V. G.; Myshkina, A. V.; Vazirov, R. A.; Pizurova, N.; Kasyanova, V. V. Luminescence and Optical Properties of Cerium Oxide Nanoparticles. *Opt. Mater. (Amst).* **2019**, *92*, 136–142. https://doi.org/10.1016/j.optmat.2019.04.021.

(42) Zhang, H.; Banfield, J. F. Thermodynamic Analysis of Phase Stability of Nanocrystalline Titania. *J. Mater. Chem.* **1998**, *8*, 2073-2076. https://doi.org/10.1039/a802619j.

(43) Raveendran, P.; Fu, J.; Wallen, S. L. A Simple and "Green" Method for the Synthesis of Au, Ag, and Au–Ag Alloy Nanoparticles. *Green Chem.* **2006**, *8*, 34-38. https://doi.org/10.1039/b512540e.

(44) Degheidy, A. R.; Elwakil, S. A. A.; Elkenany, E. B. Energy Band Structure Calculations of $Ga_xIn_{1-X}P$ Alloys under the Influence of Temperature and Pressure. *J. Alloys Compd.* **2013**, *574*, 580-590. https://doi.org/10.1016/j.jallcom.2013.05.084.

(45) Chen, P. W.; Huang, S. Y.; Wang, C. C.; Yuan, S. H.; Wuu, D. S. Influence of Oxygen on Sputtering of Aluminum-Gallium Oxide Films for Deep-Ultraviolet Detector Applications. *J. Alloys Compd.* **2019**, *791*, 1213–1219. https://doi.org/10.1016/j.jallcom.2019.03.339.

(46) Harwig, T.; Kellendonk, F.; Slappendel, S. The Ultraviolet Luminescence of β-Galliumsesquioxide. *J. Phys. Chem. Solids.* **1978**, *6*, 675-680. https://doi.org/10.1016/0022-3697(78)90183-X.

(47) Ng, N.; Rogers, M. A. Surfactants. In Encyclopedia of Food Chemistry, 1st ed.; *Elsevier Science:* Amsterdam, NL, **2018,** *1*, 276-282. https://doi.org/10.1016/B978-0-08-100596-5.

(48) Mourdikoudis, S.; Liz-Marzán, L. M. Oleylamine in Nanoparticle Synthesis. *Chem. Mater*. **2013**, *9*, 1465-1476. https://doi.org/10.1021/cm4000476.

(49) Mehta, S. K.; Kumar, S.; Chaudhary, S.; Bhasin, K. K. Nucleation and Growth of Surfactant-Passivated CdS and HgS Nanoparticles: Time-Dependent Absorption and Luminescence Profiles. *Nanoscale.* **2010**, *2*, 145-152. https://doi.org/10.1039/b9nr00070d.

(50) Grigorieva, N. A.; Fleitlikh, I. Y. Redox Processes in the Organic Phase during Cobalt Extraction with the Bis(2,4,4-Trimethylpentyl)Dithiophosphinic Acid and Trioctyl Phosphine Oxide Mixtures. *Solvent Extr. Ion Exch.* **2015**, *33*, 278–294. https://doi.org/10.1080/07366299.2014.993232.

(51) Hao, J.; Li, Y.; Xu, X.; Zhao, F.; Pan, R.; Li, J.; Liu, H.; Wang, K.; Li, J.; Zhu, X.; Delville, M. H.; Zhang, M.; He, T.; Cheng, J. Metal-to-Ligand Charge Transfer Chirality Sensing of d-Glucose Assisted with GOX-Based Enzymatic Reaction. *Adv. Mater. Technol.* **2020**, *5*, 138-139. https://doi.org/10.1002/admt.202000138.

(52) Giri, A.; Goswami, N.; Pal, M.; Zar Myint, M. T.; Al-Harthi, S.; Singha, A.; Ghosh, B.; Dutta, J.; Pal, S. K. Rational Surface Modification of Mn_3O_4 Nanoparticles to Induce Multiple Photoluminescence and Room Temperature Ferromagnetism. *J. Mater. Chem. C.* **2013**, *1*, 1885–1895. https://doi.org/10.1039/c3tc00709j.

(53) Stouwdam, J. W.; Hebbink, G. A.; Huskens, J.; Van Veggel, F. C. J. M. Lanthanide-Doped Nanoparticles with Excellent Luminescent Properties in Organic Media. *Chem. Mater.* **2003**, *15*, 4604-4616. https://doi.org/10.1021/cm034495d.

(54) Bünzli, J. C. G. Lanthanide Photonics: Shaping the Nanoworld. *Trends in Chem*. **2019**, *1*, 751-762. https://doi.org/10.1016/j.trechm.2019.05.012.

(55) Li, Y.; Li, Y.; Wang, H.; Liu, R. Yb^{3+}, Er^{3+}Codoped Cerium Oxide Upconversion Nanoparticles Enhanced the Enzymelike Catalytic Activity and Antioxidative Activity for Parkinson's Disease Treatment. *ACS Appl. Mater. Interfaces* **2021**, *13*, 13968–13977.

https://doi.org/10.1021/acsami.1c00157.

(56) Hasegawa, Y.; Kitagawa, Y.; Nakanishi, T. Effective Photosensitized, Electrosensitized, and Mechanosensitized Luminescence of Lanthanide Complexes /639/638/439/943 /639/638/911 Review-Article. *NPG Asia Mater.*. **2018**, *10*, 52-70. https://doi.org/10.1038/s41427-018-0012-y.

(57) Liu, H.; Owen, J. S.; Alivisatos, A. P. Mechanistic Study of Precursor Evolution in Colloidal Group II-VI Semiconductor Nanocrystal Synthesis. *J. Am. Chem. Soc.* **2007**, *129*, 306-312. https://doi.org/10.1021/ja0656696.

(58) Abel, K. a; Shan, J.; Boyer, J.; Harris, F.; Van Veggel, F. C. J. M. Beneficial Effect of Trioctylphosphine. *Comm.* **2008**, *20*, 3794–3796.

(59) Meng, F.; Fan, Z.; Chen, G.; Yang, X. Excellent Near-UV Emission and Room-Temperature Ferromagnetism of Square-like Nano-CeO_2 Mingled with $Ce(OH)_3$ Synthesised by a Hydrothermal Method. *Micro Nano Lett.* **2016**, *11*, 284–286. https://doi.org/10.1049/mnl.2015.0591.

(60) Aslam, M.; Qamar, M. T.; Soomro, M. T.; Ismail, I. M. I.; Salah, N.; Almeelbi, T.; Gondal, M. A.; Hameed, A. The Effect of Sunlight Induced Surface Defects on the Photocatalytic Activity of Nanosized CeO_2 for the Degradation of Phenol and Its Derivatives. *Appl. Catal. B. Environ.* **2016**, *180*, 391–402. https://doi.org/10.1016/j.apcatb.2015.06.050.

(61) Wang, S.; Tang, S.; Gao, H.; Fang, L.; Hu, Q.; Sun, G.; Chen, X.; Yu, C.; Liu, H.; Pan, X. Modified Polyacrylamide Gel Synthesis of CeO_2 Nanoparticles by Using Cerium Sulfate as Metal Source and Its Optical and Photoluminescence Properties. *J. Mater. Sci. Mater. Electron.* **2021**, *32*, 10820–10834. https://doi.org/10.1007/s10854-021-05740-w.

(62) Lazić, V.; Živković, L. S.; Sredojević, D.; Fernandes, M. M.; Lanceros-Mendez, S.; Ahrenkiel, S. P.; Nedeljković, J. M. Tuning Properties of Cerium Dioxide Nanoparticles by Surface Modification with Catecholate-Type of Ligands. *Langmuir.* **2020**, *36*, 9738–9746. https://doi.org/10.1021/acs.langmuir.0c01163.

(63) Farvid, S. S.; Dave, N.; Radovanovic, P. V. Phase-Controlled Synthesis of Colloidal In_2O_3 Nanocrystals via Size-Structure Correlation. *Chem. Mater.* **2010**, *22*, 9-11. https://doi.org/10.1021/cm9014783.

(64) Cook, D. S.; Kashtiban, R. J.; Krambrock, K.; de Lima, G. M.; Stumpf, H. O.; Lara, L. R. S.; Ardisson, J. D.; Walton, R. I. Nanocrystalline Transition-Metal Gallium Oxide Spinels from Acetylacetonate Precursors via Solvothermal Synthesis. *Mater. (Basel).* **2019**, *12*, 838. https://doi.org/10.3390/MA12050838.

(65) He, L.; Su, Y.; Lanhong, J.; Shi, S. Recent Advances of Cerium Oxide Nanoparticles in Synthesis, Luminescence and Biomedical Studies: A Review. *J.Rare Earths*. **2015**, *33*, 791-799. https://doi.org/10.1016/S1002-0721(14)60486-5.

(66) Borra, C. R.; Vlugt, T. J. H.; Yang, Y.; Offerman, S. E. Recovery of Cerium from Glass Polishing Waste: A Critical Review. *Metals (Basel).* **2018**, *8*, 801. https://doi.org/10.3390/met8100801.

(67) Saikumar, A. K.; Nehate, S. D.; Sundaram, K. B. A Review of Recent Developments in Aluminum Gallium Oxide Thin Films and Devices. *Crit. Rev. Solid State Mater. Sci.*

2021, *16*, 801-817. https://doi.org/10.1080/10408436.2021.1922357.

(68) Layek, A.; Stanish, P. C.; Chirmanov, V.; Radovanovic, P. V. Hybrid ZnO-Based Nanoconjugate for Efficient and Sustainable White Light Generation. *Chem. Mater.* **2015**, *27*, 1021-1030. https://doi.org/10.1021/cm504330k.

(69) Sabari Arul, N.; Mangalaraj, D.; Chen, P. C.; Ponpandian, N.; Viswanathan, C. Strong Quantum Confinement Effect in Nanocrystalline Cerium Oxide. *Mater. Lett.* **2011**, *65*, 2635–2638. https://doi.org/10.1016/j.matlet.2011.05.022.

(70) Dale, J. G.; Cox, S. S.; Vance, M. E.; Marr, L. C.; Hochella, M. F. Transformation of Cerium Oxide Nanoparticles from a Diesel Fuel Additive during Combustion in a Diesel Engine. *Environ. Sci. Technol.* **2017**, *51*, 1973-1980. https://doi.org/10.1021/acs.est.6b03173.

(71) Ozaki, Y. Infrared Spectroscopy—Mid-Infrared, Near-Infrared, and Far-Infrared/Terahertz Spectroscopy. *Anal. Sci.* **2021**, *37*, 1193-1212. https://doi.org/10.2116/analsci.20R008.

(72) Nyoka, M.; Choonara, Y. E.; Kumar, P.; Kondiah, P. P. D.; Pillay, V. Synthesis of Cerium Oxide Nanoparticles Using Various Methods: Implications for Biomedical Applications. *Nanomater.* **2020**, *10*, 242. https://doi.org/10.3390/nano10020242.

(73) Sakthiraj, K.; Karthikeyan, B. Synthesis and Characterization of Cerium Oxide Nanoparticles Using Different Solvents for Electrochemical Applications. *Appl. Phys. A Mater. Sci. Process.* **2020**, *126*, 1–10. https://doi.org/10.1007/s00339-019-3227-z.

(74) Shi, Z.; Gong, J.; Zhang, J.; Xu, P.; Yao, N.; Fang, W.; Wang, P.; Guo, X.; Tong, L. Single-Nanowire Thermo-Optic Modulator Based on a Varshni Shift. *ACS Photonics.* **2020**, *9*, 2571-2577. https://doi.org/10.1021/acsphotonics.0c00917.

(75) Deus, R. C.; Cortés, J. A.; Ramirez, M. A.; Ponce, M. A.; Andres, J.; Rocha, L. S. R.; Longo, E.; Simões, A. Z. Photoluminescence Properties of Cerium Oxide Nanoparticles as a Function of Lanthanum Content. *Mater. Res. Bull.* **2015**, *70*, 416–423. https://doi.org/10.1016/j.materresbull.2015.05.006.

(76) Grindlay, G.; Gras, L.; Mora, J.; De Loos-Vollebregt, M. T. C. Carbon-, Sulfur-, and Phosphorus-Based Charge Transfer Reactions in Inductively Coupled Plasma-Atomic Emission Spectrometry. *Spectrochim. Acta - Part B At. Spectrosc.* **2016**, *115*, 8–15. https://doi.org/10.1016/j.sab.2015.10.010.

(77) Ćirić, A.; Stojadinović, S. Photoluminescence of Gd_2O_3 and Gd_2O_3:Ln^{3+} (Ln = Eu, Er, Ho) Formed by Plasma Electrolytic Oxidation of Pure Gadolinium Substrate. *Opt. Mater. (Amst).* **2020**, *99*, 546-551. https://doi.org/10.1016/j.optmat.2019.109546.

(78) Yin, H.; Li, Y.; Bai, J.; Ma, M.; Liu, J. Effect of Calcinations Temperature on the Luminescence Intensity and Fluorescent Lifetime of Tb^{3+}-Doped Hydroxyapatite (Tb-HA) Nanocrystallines. *J. Mater.* **2017**, *3*, 144-149. https://doi.org/10.1016/j.jmat.2016.11.004.

Appendix

Safety Hazards

Safety is a priority in the Radovanovic lab. Gloves, goggles, and lab coats are always worn in the lab and all volatile chemicals are used in a fume hood. All synthesis was operated under a fume hood to contain any spills and volatile gases. Chemicals used during the project are hazardous and are handled with care. Material safety data sheets were reviewed for all chemicals used in this project. Acetylacetonate precursors are toxic through inhalation and ingestion and so masked were used when weighing and adding the precursors to reaction containers. Acetone, ethanol, and hexane are volatile solvents. They are flammable and may cause skin and eye irritation from direct contact. TOPO and OAM are corrosive and causes skin and eye irritation. Equipment was used only after completing safety training. Autoclaves were handled with care and proper standard operating procedures. They were cooled safely to room temperature in the oven after it was shut off to avoid handling at high temperatures.